UNIVERSITY OF OKLAHOMA

GRADUATE COLLEGE

THE STUDIES OF CONFINED FLUID PHASE BEHAVIOR IN SHALE RESOURCES

A DISSERTATION

SUBMITTED TO THE GRADUATE FACULTY

in partial fulfillment of the requirements for the

Degree of

DOCTOR OF PHILOSOPHY

By

YIXIN MA
Norman, Oklahoma
2018

THE STUDIES OF CONFINED FLUID PHASE BEHAVIOR IN SHALE RESOURCES

A DISSERTATION APPROVED FOR THE
MEWBOURNE SCHOOL OF PETROLEUM AND GEOLOGICAL ENGIEERING

BY

_____
Dr. Ahmad Jamili, Chair

_____
Dr. Jeffrey H. Harwell

_____
Dr. Xingru Wu

_____
Dr. Ramadan M. Ahmed

_____
Dr. Bor-Jier (Ben) Shiau

Dedicated to my family and my friends

Acknowledgements

First and the most, I would like to express my heartiest gratitude to my academic advisor, Dr. Ahmad Jamili, for his veritable academic Godfathers to me during my PhD studies at OU in these years. His guidance and supports are the most important driving force pushing me forward.

Thanks are extended to rest the committee members, Dr. Jeffrey Harwell, Dr. Xingru Wu, Dr. Ramadan Ahmed and Dr. Bor-Jier Shiau, for their excellent guidance and invaluable advice. I would like to especially thank Dr. Xingru Wu for his self-forgetful patience on guiding me and exposing me to new knowledge.

I would also like to thank Dr. Carl Sondergeld and Dr. Chandra Rai for allowing me to participate the activities for the Unconventional Shale Resource Consortium. Such precious experience is one of the most important elements that built up my academic success.

Finally, I would like to thank my parents for their endless support behind me, without which I can never step any further. Also, I would like to have special thanks to my friends at OU, especially Shuoshi, Qin, Li, Luchao, Jiman, Xiaochun, Alireza, Saied, Sumeer, Mounraj, Aman, Aditya, Victor, Chao, Changlong, Yuqing, Yinan and many others who helped me through the struggling time and colored my life here at OU.

Table of Contents

List of Tables

List of Figures

ABSTRACT

Fluid phase behavior in porous media is governed by not only fluid-fluid interactions but also fluid-wall interactions. In shale formations, a large amount of hydrocarbon fluid is stored within the organic matters where the pore sizes are in the order of nanometer scales. Inside these nanopores, the interactions between the fluid molecules and porous walls play such an important role that can change the fluid physical properties of the stored hydrocarbons.

The first part of this work is to focus on investigating the effects of pore proximity in shale formations on phase behavior of the reservoir fluids by modifying the cubic equations of state (EOS), e.g. van der Waals EOS and Peng-Robinson EOS. Effects of both fluid-fluid and fluid-wall interactions are included in the modified EOS. Such effects were averaged for any particular pore sizes. Correlations based upon the available molecular simulation results were developed to include the effects of fluid-wall interactions into the modified EOS. The relationships between the binary interaction coefficients and pore sizes of a C1/nC5 binary mixture were obtained based on experimental data using modified Peng-Robinson EOS. The vapor-liquid equilibrium (VLE) calculations were performed on a C1/nC4/C10 ternary mixture using the modified Peng-Robinson EOS. The results showed that smaller pores caused the fluid mixture to behave similar to dry gas, which results in reduction in condensate banking and delay in condensate dropout during production in comparison to conventional reservoirs.

Although the fluid phase behavior was calculated based on an average point of view for different pore sizes. It is believed that the fluids inside the nanoscale pores are not

uniformly distributed due to the fluid-wall interactions. The fluid density is higher near the wall than the center region of the pore. The second part of this work is concentrated on obtaining the fluid density profiles across the pore. The fluids in nanoscale pores were considered to form bulk phase, transition phase and adsorbed phase depended on the distances to the pore walls. Simplified Local Density (SLD) theory coupled with the modified Peng-Robinson EOS was used to calculate the density profiles for both single-component fluids and mixtures in different pore sizes. Both the fluid density profiles of single component fluids (e.g. methane, ether, propane and n-butane) and binary mixtures were investigated using the SLD-PR model. The results showed that the fluid density near the wall is much higher than that in the center of the pore. On the other hand, pressure, temperature, pore size, fluid type and fluid composition all have impacts on the fluid distributions. Higher pressure can shift the fluid density profile to a higher value while increase in temperature can shift down the density profile. For heavy components, such as n-butane, the adsorbed region is larger than that for light components, such as methane. For fluid mixtures, the composition of the fluid changes across the pore and the composition of the heavier component is much higher close to the pore compare to the bulk fluid.

The third part of this work is the application of the SLD theory to couple with a new Gas-In-Place (GIP) model on a case study of predicting the phase behavior of real reservoir fluids in condensate window of Eagle Ford shale and estimating the adsorbed gas content and the total GIP of the reservoir at high temperature and pressure. The preliminary computation results showed that the adsorbed gas could take more than 30% of gas in place in Eagle Ford shale. By using the introduced method, the adsorbed gas content and

the total GIP in unconventional reservoirs were calculated with good accuracy under short computational time. This makes the model useful when implemented into reservoir simulators.

The fourth part of this work investigates the occurrence of capillary condensation inside nanoporous shales and the way to quantify the condensed fluid contents and the behaviors using the SLD model combined with modified Young-Laplace equation. It is the first attempt to quantitatively consider both adsorption and capillary condensation for hydrocarbon mixtures in shale media. For a retrograde mixture, the effects of capillary condensation reduce the lower dew point pressure and increase the upper dew point pressure. The shift is larger for the lower dew point pressure. This finding is consistent with the results calculated using the modified EOS to consider the pore size effects in the first part of this dissertation, which gives a cross-validation to both models.

The last part of this dissertation work focuses on molecular dynamic (MD) simulations of hydrocarbons in nanopores. A universal molecular simulator called LAMMPS is used to perform MD simulations of hydrocarbon mixtures. From these MD simulations, we are able to investigate how hydrocarbon fluids are arranged under the effects of the pore wall. The results show that the pore wall attracts hydrocarbon molecules to form a high-density adsorbed region. This agrees with the findings from SLD model described in previous chapters.

Chapter 1: Introduction

1.1 Introduction to Shale Resources

The boom of oil and gas production from unconventional resources in the US has significantly shifted attentions in the oil industry from conventional type of reservoirs to these unconventional resources such as liquid-rich shale, gas shale, tight gas and coalbed methane. **Figure 1.1** shows the natural gas production by type in the US from 1995 to 2040. As the year of 2016, more than half of the natural gas production in the US is from unconventional resources. The most important contributor, shale gas and tight oil plays, takes up to 45% of the total natural gas production in 2016 and is expected to grow to over 60% in the year of 2040, according to US Energy Information Administration Annual Energy Outlook (EIA, 2017).

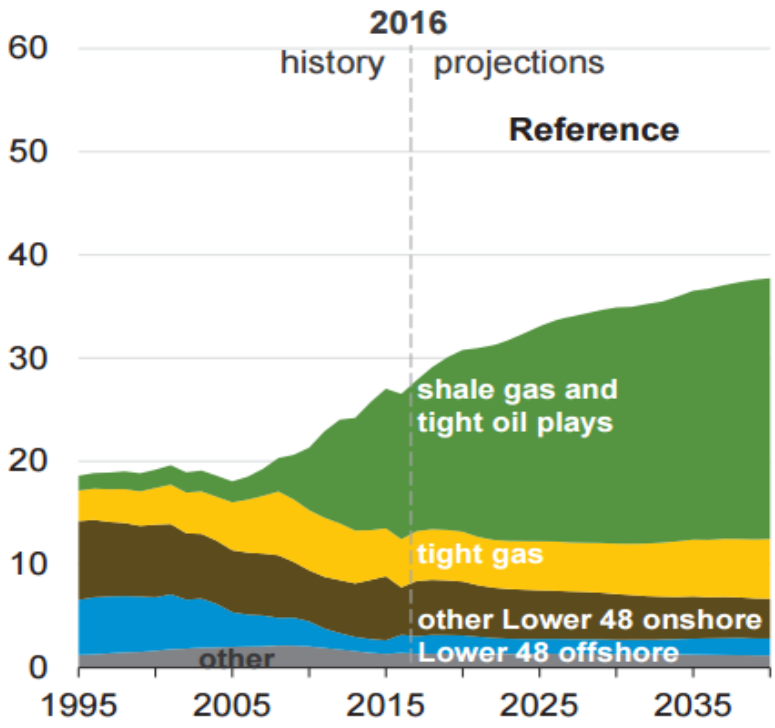

Figure 1.1—Natural gas production in the US by source from 1990 to 2040 (EIA, 2013)

Besides the natural gas production boom, the oil production from shale oil resources has also been growing rapidly recently and is expected to continuously increase in a tremendous speed. **Figure 1.2** shows the location of major shale gas and shale oil plays in the lower 48 states in the US as of June 2016, including current plays and prospective plays. Shale oil plays like Permian, Eagle Ford and Bakken are the major shale oil production contributors in the US as of now and in the future (shown in **Figure 1.3**). As we can see, the tight oil production takes roughly half of the total US oil production in 2016.

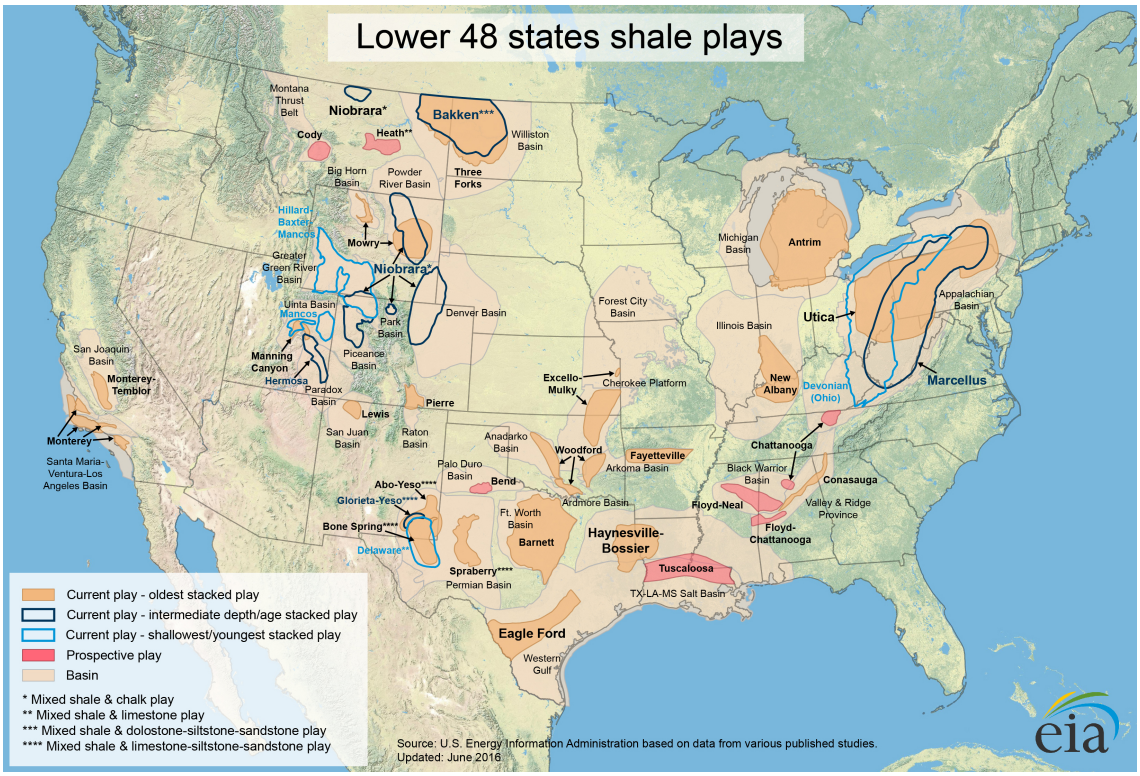

Figure 1.2— Location of major shale gas and oil plays in the lower 48 states in the US as of June 2016, including current plays and prospective plays (EIA, 2017)

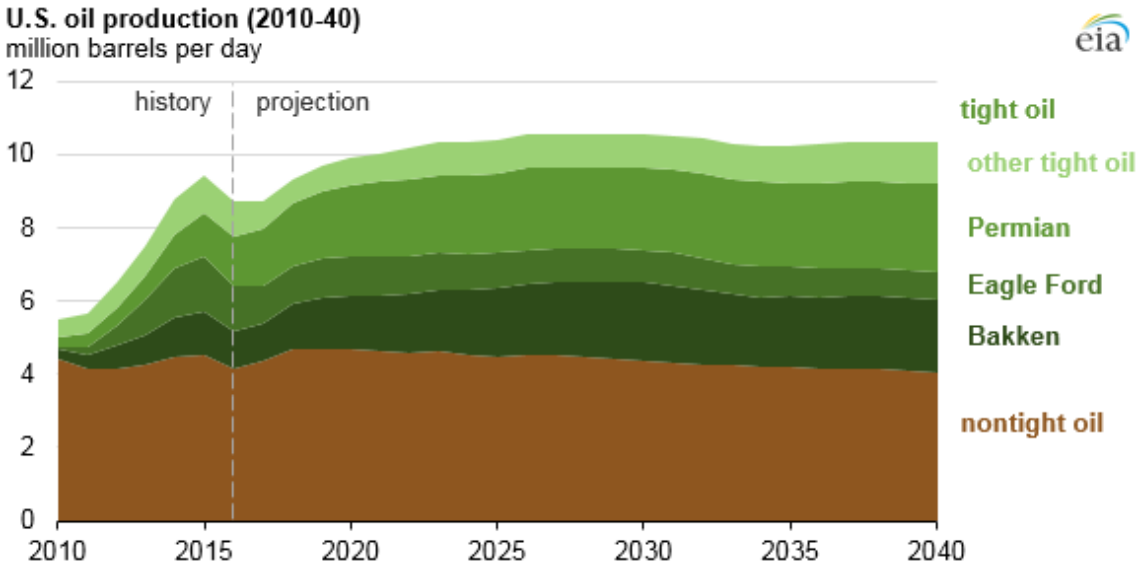

Figure 1.3—US oil production now and the future (EIA, 2017)

Shale formations are formed by fine-grained, clastic sedimentary rock composed of muds that consist of two different components, organic matters and inorganic matters. Organic matters are a mixture of organic materials that are composed of the remains of once-living organisms such as plants and animals and their wasted products while inorganic matters contain is a mix of flakes of clay minerals and small fragments of quartz, pyrite and other minerals (EIA, 2013). Many of the hydrocarbon fluids are stored inside organic matters, although some can be found in the natural fractures and inorganic porosities.

The investigation of microstructure of shale formations is achieved recently by using instruments that can create high-resolution images. For example, a combination of focused ion beam (FIB) and scanning electron microscopy (SEM) can show nanometer-scale resolution imaging of shale samples in both two and three dimensions (Curtis et al., 2011). **Figure 1.4** shows typical 2-D FIB-SEM images from different shale rocks (Curtis

et al., 2010). From the images, it is clear to distinguish organic matters (dark grey), clay (light grey), minerals like pyrite (white) and fractures and pores (black regions).

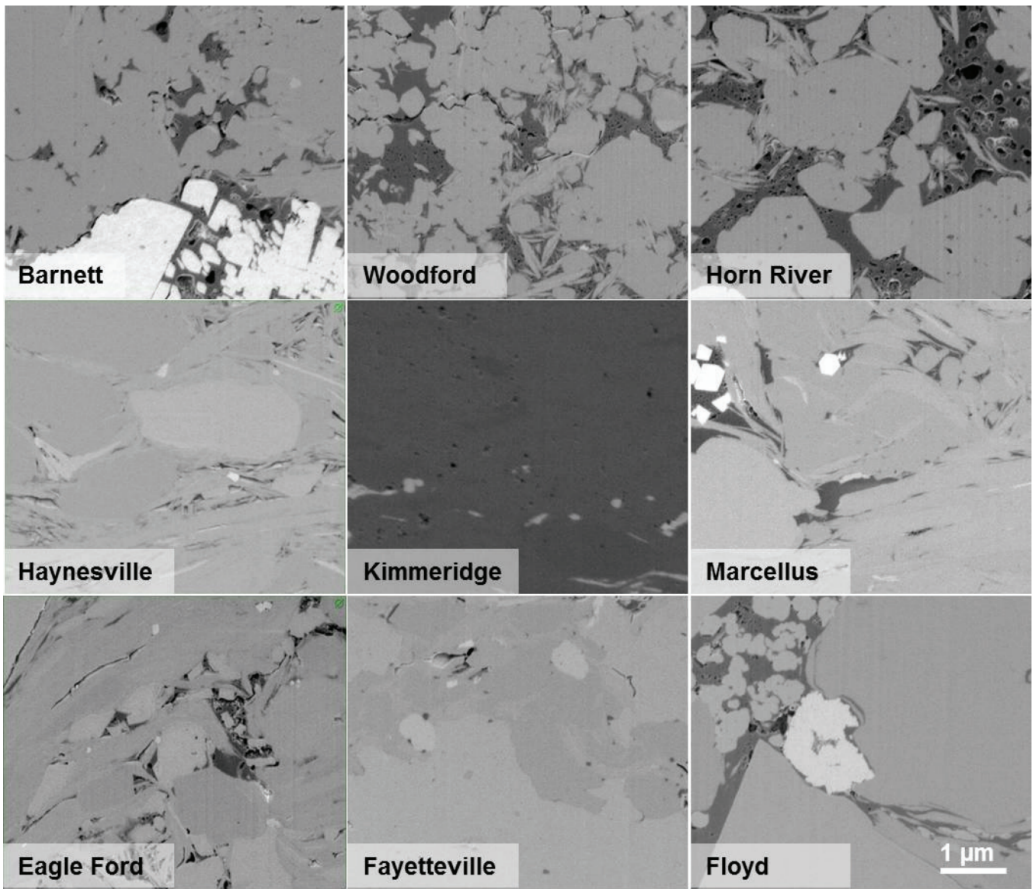

Figure 1.4—2-D FIB-SEM images from different shale reservoirs (Curtis et al., 2010)

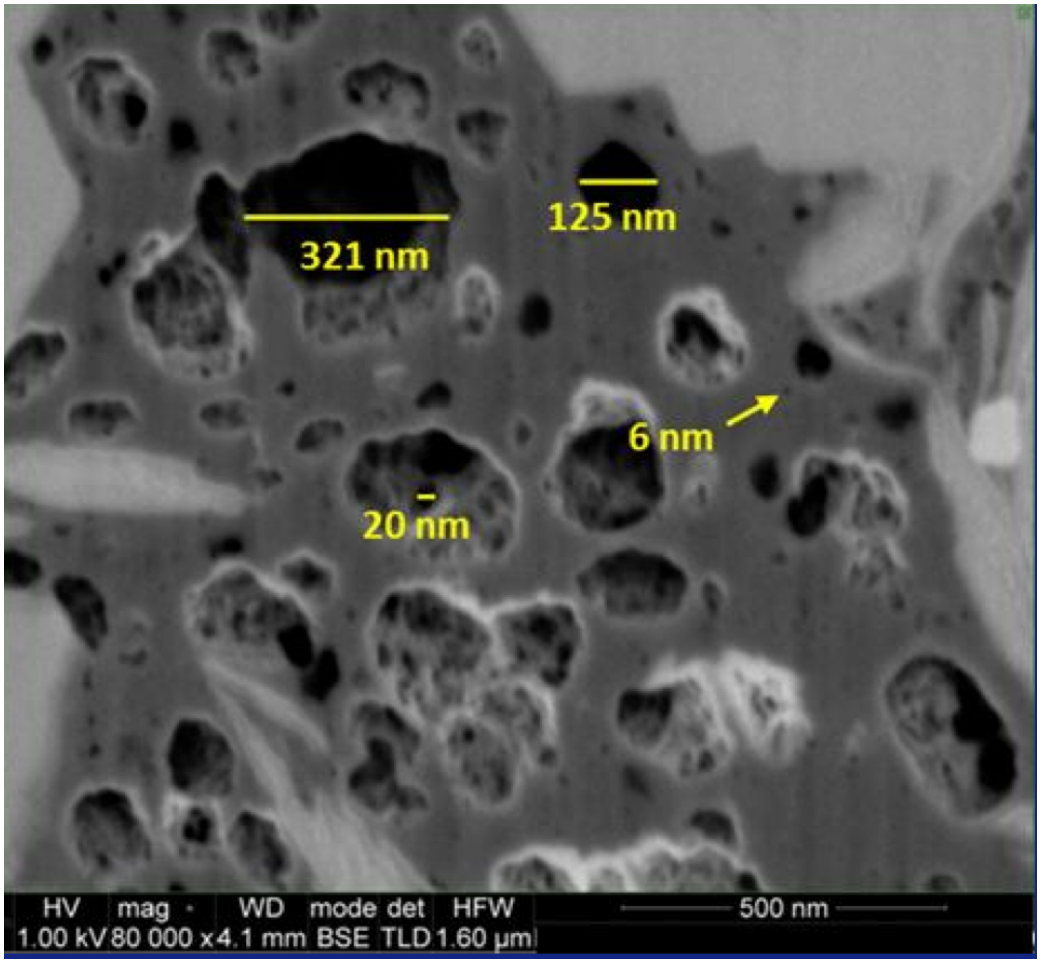

Figure 1.5—SEM image of organic contents from a shale sample (Curtis et al., 2010)

Figure 1.5 gives the image of organic contents, or kerogen contents from a shale sample using FIB-SEM technique. It shows that the size of pores inside kerogen contents is in the order of nanometers. In such small pores, the influence of the kerogen wall on the stored fluids becomes important due to the fluid-wall interactions. The fluids inside the kerogen pores are stored in two forms: adsorbed form near kerogen wall and bulk form in the center of the pore. The adsorbed fluids are under strong influence of the kerogen wall interactions and their properties become deviate from the bulk fluid properties. There

may have a transition zone between the adsorbed fluids and bulk fluids in relatively larger pores where exists weaker fluid-wall interactions compare to that in the adsorbed zone (Didar and Akkutlu, 2013). The properties of the fluids inside the transition zone may deviate from bulk values. In order to investigate the fluid properties and transport properties of the hydrocarbons stored inside the kerogen contents, one need to start from phase behaviors considering the effects of the interactions between the fluids and kerogen walls.

1.2 Phase Behavior in Shale Resources

Although the production in shale plays is growing vigorously, the phase behavior in shale resources has not been fully understood. In general, fluids under confinement within pores of nanometer-scale size exhibit significant deviation from their bulk values due to the molecular interactions between the fluid and the pore wall. The changes include fluid properties, such as critical properties, fluid densities, viscosities, compressibility factor, vapor/liquid interfacial tension as well as other fluid properties. In shale formations, molecular sizes approach typical values for the pore sizes. Therefore, the influence of both fluid-wall interactions and fluid-fluid interactions on phase behavior and fluid properties among others becomes important.

It has long been known that the pore size can have effects on fluid properties. Physical experiments have been conducted to investigate the effects of pore size on fluid phase behavior in porous media back in 1960s. Tindy and Raynal (1966) documented the bubble point pressure variations of two crude oils measured in both PVT cells and porous media. Grain sizes in the porous media were in the range of 160 to 200 microns. Bubble point

pressure was reported higher in the porous medium than PVT cell by 7 and 4 kg/cm^2. The bubble point pressures of one of the crude oils at 80 °C in the porous medium and PVT cell were 128 and 121 kg/cm^2 respectively. However, there was no difference in the measured bubble point pressures between porous medium and PVT cell for a mixture of methane and n-heptane. Trebin and Zadora (1968) investigated effect of pore size on phase behavior of gas condensate systems. They used a silica sand mixture (0.3 to 0.215 mm in diameter) as a porous medium. Table 1.1 shows permeability, porosity, and calculated surface area of three different packings used as porous medium. pore size was reported to have a strong influence on the vapor-liquid equilibrium and dew point pressure. They found that dew point pressure increases by increasing the surface area resulting in less liquid production. The dew point pressure was reported to increase 10% to 15%. Increasing the temperature decreased the effect of porous media on vapor-liquid equilibria.

Table 1.1: Properties of different packings (Trebin and Zadora, 1968)

Packing No.	Permeability (Darcy)	Porosity (%)	Surface area (cm^2/cm^3)
1	5.6	34	563
2	0.612	31.4	1,307
3	0.111	29.8	3,415

Sigmund et al. (1973) studied the effect of pore size on phase behavior by conducting experiments and calculations. They used C1-nC4 and C1-nC5 with different compositions as fluid mixtures at 100 °F and different pressure conditions. Capillary pressure was used to represent the effect of porous medium. It was reported that porous media with smallest packings of 30-40 U.S. meshes showed no effect on phase behavior

except at very high surface curvatures, where the bubble point pressures decrease under higher surface curvatures (mean curvature value less than -2.0×10^5 cm^{-1}). Thommes and Findenegg (1994) observed critical-point shift for pure SF_6 in controlled-pore glass (CPG) with mean pore diameters of 24 and 31 nm. They found in the experiments and lab measurements that the critical temperature shift was 0.92 K ± 0.24 K for CPG with 24-nm mean pore size and 0.48 K ± 0.23 K for CPG with 31-nm mean pore size. They also performed theoretical predictions of the confined geometry effects and found that the critical temperature shift ΔT_c is related to the pore size D as a power law $\Delta T_c \propto D^{-y}$, where the parameter y is about 1.6 for slit pores and has a value that is greater than 2 for CPG materials. Similar measurements were performed by Findenegg et al. (1994) using different fluids in CPG with mean pore sizes of 7.7 and 24 nm. The fluids were extended to cycolpentane, iso-pentane and perfluoropentane and the decreases in critical temperatures of these fluids were observed. Danesh (1998) claimed that the effect of pore size is significant when the pore size is less than 10 nm. Voronov et al. (2003) investigated the effects of pore size on phase behavior of C1/nC5 mixtures with different compositions of n-pentane near critical regions. The porous material used in this study was quartz powder with the characteristic pore size of 2.3 μm. The results showed that the dew point and bubble point pressures in porous media are more than that in bulk near the critical point. They believed that the dew-bubble curve shift was caused by the formation of wetting film on the surface of the porous media. Zeigermann et al. (2009) used NMR technique to measure diffusivity of n-pentane in both Vycor porous glass (pore size of 6 nm) and ERM glass (pore size of 15 nm) and found that the self-diffusivity jumped when the temperature was increased to 438 K and 458 K, respectively (shown in **Figure 1.6**).

This jump in diffusivity indicated the fluid changed from liquid to supercritical phase. While the critical temperature for bulk n-pentane was measured to be 470 K. Therefore, the results showed that the critical temperature of n-pentane decreased by 32 K and 12 K when confined in Vycor porous glass and ERM glass, respectively. As we can see, all these experimental evidences suggesting the existence of the changes in fluid phase behavior when confined in small pores. However, no clear conclusions can be drawn from these studies, due to the disagreement among the results and lack of data.

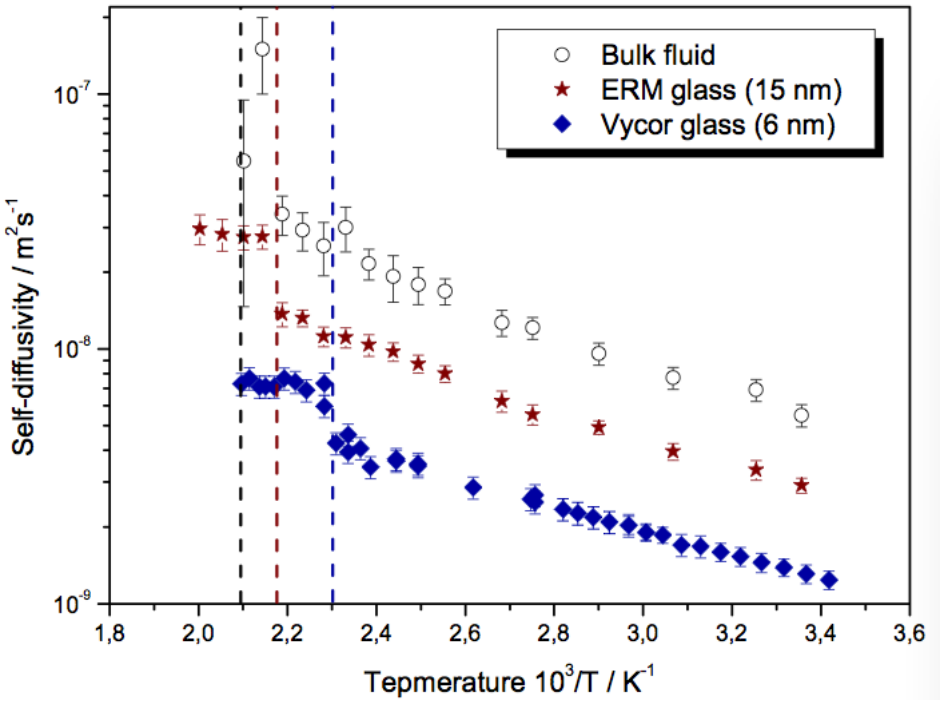

Figure 1.6— Self-diffusivity of n-pentane again temperature for bulk fluid and fluid confined in ERM glass and Vycor glass (Zeigermann et al., 2009)

On the other hand, simulations are taken place from different point of views to study the effects of pore size. Some of the better-known modeling approaches are molecular dynamics, equation of state modification and density functional theory. For example,

Ambrose et al. (2012) performed a molecular simulation study to investigate the adsorption of methane in a graphite slit. Density profiles of methane across the pore were obtained from molecular dynamic studies. From the methane density profiles, they found that the density values of the adsorbed layers were usually 2 to 2.5 times higher than the methane bulk density. Derouane (2007) proposed a simple modification of the van der Waals equation of state by introducing a new term that takes into account the attractions between the fluid molecules and the pore wall. The model quantitatively predicts the critical temperature decreases and critical pressure increases by decreasing the pore size. More details of the models on confined fluid phase behavior will be discussed in the later chapters.

In conclusion, due to the nature of the nanopores, it is difficult to perform persuasive conventional fluid phase behavior study experiments inside these small pores. Results from laboratory measurements may not be consistent and can sometimes have the opposite trends from one to another. On the other hand, simulations are powerful tools for investigating the fluid behaviors inside nanopores. Many of the recent simulation approaches, such as molecular simulations and density functional theory, are able to show more detailed adsorption phenomena of the confined fluids than some of the traditional models such as the Langmuir single-layer adsorption model (Ambrose et al., 2012).

1.3 Research Goal

The research goal is to investigate and better understand the fluid phase behavior under nanoscale confinement in shale formations by considering both molecule-molecule and molecule-pore wall interactions. We modified the equations of state to study the effects of pore size on critical properties, as well as the vapor-liquid equilibriums of the hydrocarbon mixture. Furthermore, we used the Simplified Local Density (SLD) model that combines fluid-wall potentials with Peng-Robinson equation of state to predict the fluid density at different locations inside the pore. The SLD model was extended to help build a new Gas-In-Place (GIP) model for unconventional condensate reservoir as well as investigate capillary condensation in shale nanoporous media.

1.4 Scope of Dissertation

This dissertation contains eight chapters. Chapter 1 gives the background of the study, literature review and research goal and motivation. Chapter 2 discusses the methodology of how to modify the equations of state to capture the phase behavior change of hydrocarbon fluids inside nanopores in shale formations. Chapter 3 describes the mathematical model developed upon Simplified Local Density theory and Modified Peng-Robinson equation of state. The model is able to predict the density profiles and pure fluids and fluid mixture under certain pore size, temperature and pressure. Chapter 4 shows the results of the study including model validations, case studies and sensitivity analysis. Chapter 5 gives the development of a new gas-in-place model typically for shale gas condensate plays. The model is applied to a real-world case in Eagle Ford shale play. Chapter 6 investigates the hydrocarbon mixture fluid behaviors with the presents of both

adsorption and capillary condensation. It helps determine the adsorption thickness as well as the adsorption isotherms in the two-phase region. Chapter 7 talks about molecular dynamics (MD) simulation and its application to study the fluid behaviors in nanoscale organic pores. Chapter 8 gives the conclusions of the dissertation as well as the future work recommendations.

Chapter 2: Modifying Equations of State to Consider Confinement Effects

2.1 Background and Previous Work

In thermodynamic, an equation of state (EOS) is an equation that provides the relations between different state variables, such as temperature, pressure and volume. EOS is most commonly used to describe the state of matter and the properties of any fluids, e.g., liquids, gases and solids. There are many different forms of cubic EOS in the literature. The van der Waals back in 1873 introduced the first cubic EOS that was derived by the assumption of a finite volume occupied by the constituent molecules (JD van der Waals, 1873). After his invention of this revolutionized formula, many cubic EOS were derived based on the van der Waals EOS (Redlich and Kwong, 1949; Zudkevitch and Joffe, 1970; Soave, 1972; Peng and Robinson, 1976; Schmidt and Wenzel, 1980), among which, the Peng-Robinsion (PR) EOS and the Soave-Redlich-Kwong (SRK) EOS are the most two widely used forms of EOS in the petroleum industry. Although these EOS, especially the PR-EOS and the SRK-EOS are believed to have accurate predictions on hydrocarbon phase behavior, all of the EOS assume the fluids are in a bulk system, i.e., a system without boundary effects and is allowed to expand or shrink without restrictions. However, this may not be the case for the fluids inside porous media. When the fluids are confined within narrow pores, the existence of the wall forces, as well as the competition between the fluid-fluid and fluid-wall interactions can lead to phase behavior changes of the confined fluids (Gelb et al., 1999; Trens et al., 2005; Hamada et al., 2007, Sapmanee 2011). Evidences showing critical property shift (de Keizer et al., 1991; Findenegg et al., 1994, Thommes and Findenegg, 1994; Groß and Findenegg, 1997) and saturation

pressure shift (Tindy and Raynal, 1966; Trebin and Zadora, 1968; Sigmund et al. 1973; Voronov et al., 2003) suggest that the conventional EOS are no longer valid to accurately predict the confined fluid phase behavior due to the ignorance of the confinement effects.

Studies implementing confinement effects into EOS are available in the literature. Schoen and Diestler (1998) modified the van der Waals equation of state by using perturbation theory to study confined fluids in slit-pores. The developed equation of state can predict capillary condensation and depression of critical temperature of a fluid in mesopore qualitatively. The predictions of the equation of state were however found to be unsatisfactory in the vicinity of critical region. Zhu et al. (1999) studied confined fluids in cylindrical mesopores and developed an EOS by using the theory of thermodynamical interfaces to describe N_2 adsorption in different pore sizes. The EOS took into account the facts of the attractive interactions between the adsorbed molecules and the wall, the curvature of the gas/adsorbed phase interface and surface tension. Zarragoicoechea and Kuz (2002 and 2004) studied confined fluids in square cross section pores by extending van der Waals EOS to a microscopic van der Waals mean field model to describe the Lennard-Jones fluids confined in nanopores. They assumed a tensorial character for the pressure of confined fluid and neglected the interaction between the fluid molecules and the wall. However, they did not find good agreement between the predicted capillary condensation and critical temperature and experimental data. Derouane (2007) proposed a simple modification of van der Waals EOS by introducing a new term that takes into account the attractions between the fluid molecules and the pore wall. The short-range repulsion effects are ignored as the first approximation. The model quantitatively predicts the critical temperature decreases and critical pressure increases by decreasing the pore

size. These results are in general agreement with the findings from molecular simulation studies of Singh et al. (2009) for pore sizes bigger than 2 nm. Travalloni et al. (2010a) developed a new version of the van der Waals EOS to study phase behavior of confined pure fluids and mixtures in porous media. A continuous and homogenous cylinder was assumed to be the representative of each pore while fluid molecules were assumed spherical. Fluid molecule-fluid molecule and fluid molecule-solid wall interactions were included in the EOS through square-well potential. The developed EOS has two fitting parameters. It was claimed that the model could be used for estimation of confined and bulk fluid properties because the effect of pore size was included in the EOS. Adsorption experimental data of pure fluids (C_1, C_2, N_2, H_2, toluene, and 1-propanol) at low pressures (close to atmosphere pressure) were used to find the fitting parameters of the model. Using the fitted parameters of pure fluids, the validity of the model was tested by satisfactorily predicting the adsorption of binary (C_1-C_2 and toluene-1-propoanol) and ternary mixtures (C_1-N_2-H_2). Travalloni et al. (2010b) studied critical behavior of confined pure fluids in porous media using the novel version of van der Waals EOS developed by Travalloni et al. (2010a). They determined that confined pure fluids may exhibit one or two mechanically stable critical points, due to the presence of strong fluid molecule-solid wall interactions. They also indicated that the prediction of the distinct critical points for these confined fluids is likely to be useful in describing phase transitions in adsorption isotherms.

Most of these studies, although considered the confinement effects using different approaches, only apply to certain conditions and/or temperature and pressure ranges. For example, Travalloni et al. (2010a and 2010b) focused on the pressure range up to 6 MPa

(870 psi). Schoen and Diestler (1998) and Zhu et al. (1999) investigated pure inorganic component (SF_6 and N_2, respectively) and mainly within the temperature and pressure ranges where capillary condensation can occur. Zarragoicoechea and Kuz (2002 and 2004) predicted the critical temperature shift using the modified van der Waals EOS model and had good match against experimental data. However, it only covers the range of pore size up to only two times the fluid molecular diameter. Derouane (2007) modified the van der Waals EOS by adding a new term to consider the fluid-wall interactions but no additional information about how to solve for the parameters in the new term was documented. However, Derouane (2007) gives a direction of research of implementing the confinement effects into EOS in a simple way. In this work, we developed a new EOS that can predict the phase behavior of hydrocarbon fluids for all range of pore sizes from bulk to nanopore scale sizes (in shale formations) based on van der Waals EOS in a way similar to Derouane (2007) by adding a new term. The value of the parameter in this new term was derived based on the molecular simulation data from Singh et al. (2009). The proposed methodology was also extended to Peng-Robinson EOS for higher accuracy.

2.2 Equation of State Modification

2.2.1 Modification of van der Waals Equation of State

Derouane (2007) stated that the fluid-wall interactions are obviously strong and could reduce the 'internal pressure' correction term in the EOS. Thus, van der Waals EOS is modified to include fluid-wall interactions as follows:

$$P = \frac{RT}{v-b} - \frac{a}{v^2} + \frac{c}{v^2} \quad \text{.....(2.1)}$$

Where the term $\frac{c}{V^2}$ represents the interactions between the fluid molecule and the pore wall of the porous media. The short-range repulsion effects between the fluid molecule and the pore wall are neglected and only attraction forces are considered as the first approximation. The new parameter c is dependent on the pore size. When the pore size is infinity, the value of c will approach zero and Equation 2.1 will turn to the original van der Waals EOS.

For any cubic equations of state, the critical isotherm of the PV curve exhibits an inflection at the critical point. Mathematically speaking, the first and second derivatives of pressure with respect to volume at a constant temperature are equal to zero at critical point:

$$\left(\frac{\partial P}{\partial V}\right)_{T;cr} = 0 \quad \text{.....(2.2)}$$

$$\left(\frac{\partial^2 P}{\partial V^2}\right)_{T;cr} = 0 \quad \text{.....(2.3)}$$

Where the subscript "T" means constant temperature and "cr" means critical point. For both modified and original van der Waals EOS, the expressions of critical pressure and critical temperature can be derived from Equations 2.2 and 2.3:

$$P_c = \frac{a}{27b^2} \quad \text{.....(2.4)}$$

$$T_c = \frac{8a}{27bR} \quad \text{.....(2.5)}$$

$$P_{cz} = \frac{a}{27b^2} - \frac{c}{27b^2} \quad \text{.....(2.6)}$$

$$T_{cz} = \frac{8a}{27bR} - \frac{8c}{27bR} \quad \text{.....(2.7)}$$

Where P_c and T_c are the critical pressure and critical temperature of the original van der Waals EOS; while P_{cz} and T_{cz} are the critical pressure and critical temperature (under confinement) calculated from the modified van der Waals EOS. ΔP_C and ΔT_C can be defined as follows:

$$\Delta P_C = \frac{P_c - P_{cz}}{P_c} = \frac{c}{27b^2 P_c} \quad \text{.....(2.8)}$$

Same for ΔT_C:

$$\Delta T_C = \frac{T_c - T_{cz}}{T_c} = \frac{8c}{27bRT_c} \quad \text{.....(2.9)}$$

The parameters a and b are the constants of cubic equations of sate for bulk fluid and can be derived from Equations 2.2 and 2.3 at critical point:

$$a = \frac{27}{64}\frac{R^2 T_c^2}{P_c} \quad \text{.....(2.10)}$$

$$b = \frac{1}{8}\frac{RT_c}{P_c} \quad \text{.....(2.11)}$$

However, there is no analytical derivation for the new parameter c. The simulation data from Singh et al. (2009) were used to generate a correlation between pore size and critical temperature shift to solve for the parameter c. Details were discussed in the next section. Once the value of c has been determined for a specific pure component in a particular pore size, the modified van der Waals EOS (Equation 2.1) can be successfully solved to give fluid properties of that single component.

For a mixture, similar approach can be used if given a reasonable mixing rule. Although in the literature, some believed that the confinement effects would have impact on mixing rules (Travalloni et al., 2010), we keep it the same as what has been used in the original van der Waals EOS as the first approximation:

$$a = \sum_{i}^{n}\sum_{j}^{n} x_i x_j a_{ij} \quad \text{.....(2.12)}$$

$$b = \sum_{i}^{n} x_i b_i \quad \text{.....(2.13)}$$

Where x_i and x_j are mole fractions for species i and j, respectively. b_i represents the value of b for species i while a_{ij} has the following form:

$$a_{ij} = (1 - k_{ij})(a_i \times a_j)^{1/2} \quad \text{.....(2.14)}$$

In Equation 2.14, k_{ij} is the binary interaction coefficient. For the new parameter c can be treated in the same way as a, by applying the same mixing rule:

$$c = \sum_{i=1}^{n_c}\sum_{j=1}^{n_c} x_i x_j c_{ij} \quad \text{.....(2.15)}$$

Where c_{ij} can be expressed as:

$$c_{ij} = (1 - J_{ij})(c_i \times c_j)^{1/2} \quad \text{.....(2.16)}$$

Similar to k_{ij}, J_{ij} is another set of binary interaction coefficient that is used to describe the binary interactions between i and j in parameter c. More details of the values of J_{ij} will be investigated in Chapter 4.

Once the values of the EOS parameters are obtained, one can perform the phase equilibria calculations in confined pores using the modified van der Waals EOS by equating the fugacities of each component in each phase. The fugacity is the effective pressure that replaces the true mechanical pressure of a real fluid. In thermodynamics, fugacity provides the fundamental criterion for phase equilibria calculations. That is, the fugacity of each component must be equal in all existing phases at equilibrium. To make it dimensionless, the fugacity coefficient is introduced to be the ratio of the fugacity and the true mechanical pressure:

$$\phi = \frac{f}{P} \quad \text{.....(2.17)}$$

Note that in Equation 2.17, f is the fugacity, P is the true mechanical pressure and ϕ is the dimensionless fugacity coefficient. For a mixture, the fugacity coefficient for each component is also related to partial fugacity of that component and its composition:

$$\phi_i = \frac{f_i}{x_i P} \quad \text{.....(2.18)}$$

Where x_i is the composition of component i in a phase. If the mixture has more than one phase, then the fugacity coefficient for component i in phase m can be expressed as:

$$\phi_{i,m} = \frac{f_{i,m}}{x_i P} \quad \text{.....(2.19)}$$

The fugacity coefficient for species i in phase m solved from the original van der Waals EOS is given as:

$$\ln \phi_{i,m} = \frac{b_{i,m}}{v_{i,m} - b_{i,m}} - \ln\left(\frac{\left(v_{i,m} - b_{i,m}\right)P}{RT}\right) - \frac{2a_{i,m}}{RTv_{i,m}} \quad \text{.....(2.20)}$$

Where $\varphi_{i,m}$ and $v_{i,m}$ are fugacity coefficient and molar volume for species i in phase m, respectively. However, the fugacity expression obtained from the proposed EOS (Equation 2.1) will change due to the additional c term as:

$$\ln \phi_{i,m} = \frac{b_{i,m}}{v_{i,m} - b_{i,m}} - \ln\left(\frac{\left(v_{i,m} - b_{i,m}\right)P}{RT}\right) - \frac{2\left(a_{i,m} - c_{i,m}\right)}{RTv_{i,m}} \quad \text{.....(2.21)}$$

Equation 2.21 gives the fugacity coefficient expression for component i in phase m considering the confinement effects. When the system is at equilibrium and has more than one phase, the fugacity of each component will equate in each phase. As we can see, the pore size dependent parameter c will impact the fugacity coefficient and thus can change the conditions of the equilibrium.

2.2.2 Modification of Peng-Robinson Equation of State

Peng and Robinson (1976) developed a new two-constant EOS, known as Peng-Robinson EOS, to help better predict the phase behavior of complicated fluids such as petroleum fluids. The Peng-Robinson EOS has the following form:

$$P = \frac{RT}{v - b} - \frac{a}{v(v + b) + b(v - b)} \quad \text{.....(2.22)}$$

Peng-Robinson EOS has been so far widely used in the petroleum industry. Similar approach of modification can be applied to Peng-Robinson EOS by adding a new term to consider the fluid-wall interactions:

$$P = \frac{RT}{v - b} - \frac{a}{v(v + b) + b(v - b)} + \frac{c}{v(v + b) + b(v - b)} \quad \text{.....(2.23)}$$

Same as that in the previous section, the term $\frac{c}{v(v+b)+b(v-b)}$ represents the interactions between the fluid molecule and the pore wall of the porous media. However, the short-range repulsions are ignored as of now. The expressions of critical temperature and pressure for both original Peng-Robinson EOS and its modified form are given as:

$$P_c = 0.013234\frac{a}{b^2} \quad \text{.....(2.24)}$$

$$T_c = 0.17015\frac{a}{bR} \quad \text{.....(2.25)}$$

$$P_{cz} = 0.013234\frac{a-c}{b^2} \quad \text{.....(2.26)}$$

$$T_{cz} = 0.17015\frac{a-c}{bR} \quad \text{.....(2.27)}$$

Where P_c and T_c are the critical pressure and critical temperature of the original Peng-Robinson EOS; while P_{cz} and T_{cz} are the critical pressure and critical temperature calculated from the modified Peng-Robinson EOS. ΔP_C and ΔT_C can be defined as follows:

$$\Delta P_C = \frac{P_c - P_{cz}}{P_c} = 0.013234\frac{c}{b^2 P_c} \quad \text{.....(2.28)}$$

Same for ΔT_C:

$$\Delta T_C = \frac{T_c - T_{cz}}{T_c} = 0.17015\frac{c}{bRT_c} \quad \text{.....(2.29)}$$

The same mixing rules that used in the van der Waals EOS in the previous section are applied here for Peng-Robinson EOS. For any mixtures, the expressions of fugacity coefficient for species i for both original and modified Peng-Robinson EOS are shown below:

$$\ln\phi_i = \frac{b_i}{b}(Z-1) - \ln\left(Z - \frac{bP}{RT}\right) - \frac{a}{2\sqrt{2}bRT}\left(\frac{2\sum_j y_j a_{ij}}{a} - \frac{b_i}{b}\right)\ln\left(\frac{Z+\left(1+\sqrt{2}\right)bP/RT}{Z+\left(1-\sqrt{2}\right)bP/RT}\right) \quad (2.30)$$

$$\ln\phi_i = \frac{b_i}{b}(Z-1) - \ln\left(Z - \frac{bP}{RT}\right) - \frac{(a-c)}{2\sqrt{2}bRT}\left(\frac{2\sum_j y_j (a_{ij}-c_{ij})}{(a-c)} - \frac{b_i}{b}\right)\ln\left(\frac{Z+\left(1+\sqrt{2}\right)bP/RT}{Z+\left(1-\sqrt{2}\right)bP/RT}\right)$$

.....(2.31)

In Equation 2.31, the term c and c_{ij} can be treated in the same way as a and a_{ij}, by applying similar mixing rule.

2.3 Correlations to Determine the Pore Size Dependent EOS Parameter c

Singh et al. (2009) studies the shift in the critical temperature as a function of slit pore width from 0.5 nm to 5 nm with configurational-bias grand-canonical transition-matrix Monte Carlo simulation method. **Figure 2.1** shows the relationship between ΔT_C and pore size for methane, n-butane and n-octane in graphite and mica porous media on a log-log scale plot. From the plot, we can see that the change in ΔT_C follows the similar trend for all the cases. That is, the value of ΔT_C tends to stabilize around 0.6 when the pore size is extremely small (<0.7 nm) and begins to decrease with increasing pore size. However, the rate of change in ΔT_C starts to differentiate for different fluids when the pore sizes greater than 1.5 nm. This is due to the effects of the molecular orientation in small pores resulted from the fluid molecule-pore wall interactions. Methane has a spherical molecular configuration and the smallest molecular size. ΔT_C for methane declines very fast at bigger pore sizes compare to n-butane and n-octane that have larger molecular

sizes. To eliminate the effects of molecular size, the ratio of pore size to effective molecular diameter is used in **Figure 2.2**. The effective molecular diameter is neither the width nor the length of a molecule, but it is the diameter of the smallest cross-section of a molecule. Mao and Sinnott (2001) proposed the effective size and length of methane, ethane and butane. From their studies, the effective diameter of methane (0.399 nm) is only a little smaller than n-butane (0.415 nm) since the cross section of n-butane along the carbon chain is close to that of methane. However, when the carbon chain of a hydrocarbon molecule gets longer, the molecular configuration will change as indicated by Lucia and Bonk (2011). In their studies, they mention that long molecules such as n-octane can exhibit to the structure that is partially extended and wrapped at the ends in the liquid state rather than zigzag planar configuration. This finding will change the shape and area of the cross section of the long n-alkanes and should take into account when obtaining the effective molecular diameter. Deourane (2007) discussed the same findings. Basically, what is reported as the diameter of a molecule is actually the van der Waals diameter when there is no effect of confinement. However, the effective molecule diameter under confinement will be different due to molecule configuration along the pore wall resulted from fluid molecule-pore wall interactions.

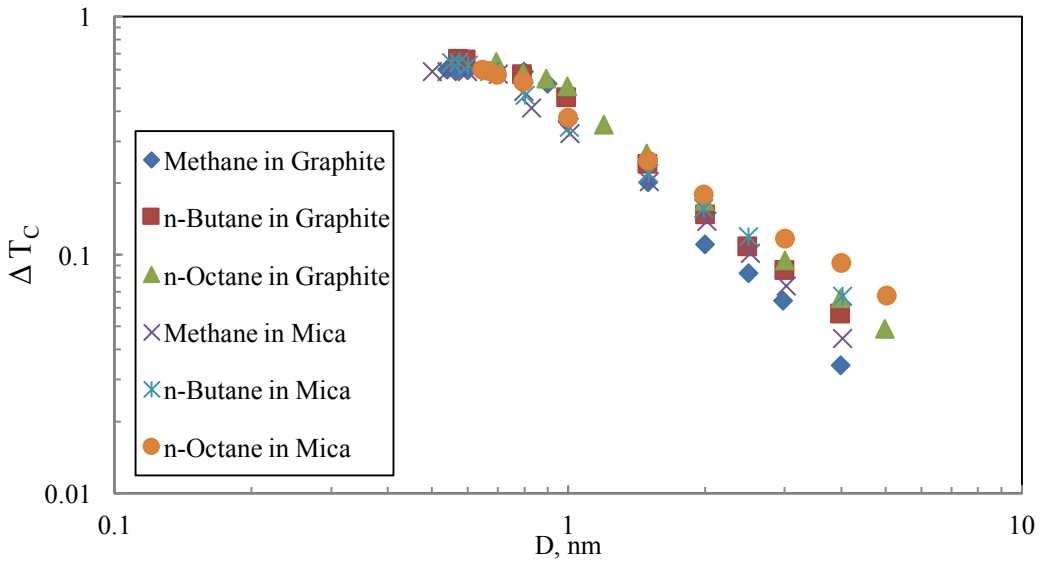

Figure 2.1—Correlation of critical temperature shift versus pore diameter

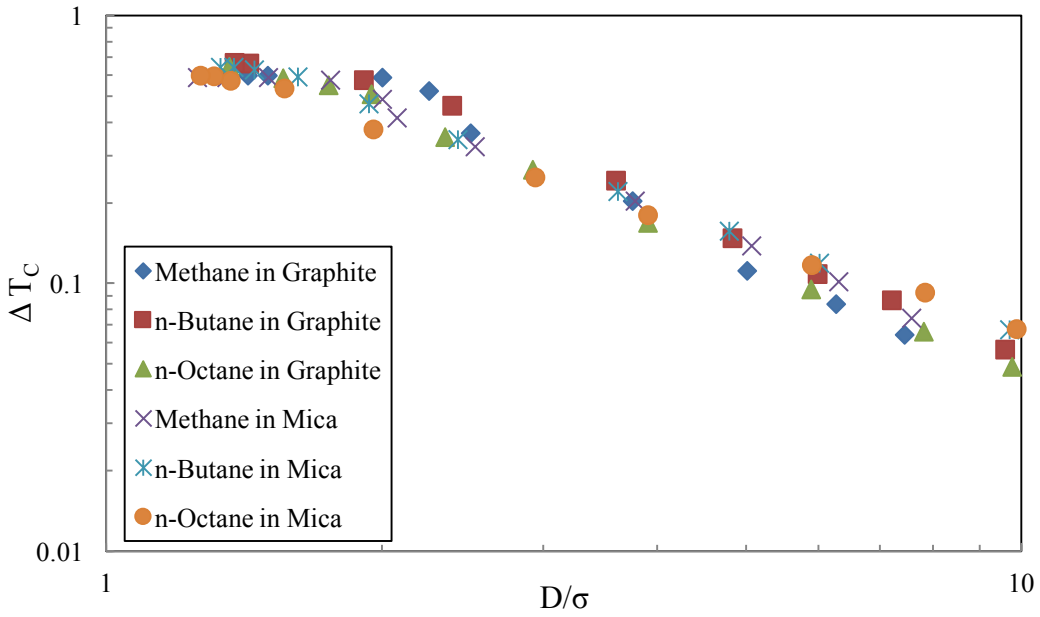

Figure 2.2—Correlation of critical temperature shift versus the ratio of pore diameter and effective molecular diameter

In **Figure 2.2** the decline rate of ΔT_C becomes much closer for all the three different fluids. A universal correlation can then be applied to present the relationships between ΔT_C vs. the ratio of pore size to effective molecular diameter as:

$$\Delta T_C = 0.6 \quad \text{when} \quad \left(\frac{D}{\sigma_{eff}}\right) < 1.5 \quad \text{.....(2.32)}$$

$$\Delta T_C = 1.1775\left(\frac{D}{\sigma_{eff}}\right)^{-1.338} \quad \text{when} \quad \left(\frac{D}{\sigma_{eff}}\right) \geq 1.5 \quad \text{.....(2.33)}$$

If substitute Equations 2.32 and 2.33 into Equation 2.9, the parameter c in the modified van der Waals EOS can be calculated for any fluids under specific pore size as:

$$c = \frac{27bRT_c}{8} \times 0.6 \quad \text{when} \quad \left(\frac{D}{\sigma_{eff}}\right) < 1.5 \quad \text{.....(2.34)}$$

$$c = \frac{27bRT_c}{8} \times 1.1775\left(\frac{D}{\sigma_{eff}}\right)^{-1.338} \quad \text{when} \quad \left(\frac{D}{\sigma_{eff}}\right) \geq 1.5 \quad \text{.....(2.35)}$$

Similarly, the parameter c in the modified Peng-Robinson EOS can be obtained by substituting Equations 2.32 and 2.33 into Equation 2.28:

$$c = 5.8772bRT_c \times 0.6 \quad \text{when} \quad \left(\frac{D}{\sigma_{eff}}\right) < 1.5 \quad \text{.....(2.36)}$$

$$c = 5.8772bRT_c \times 1.1775\left(\frac{D}{\sigma_{eff}}\right)^{-1.338} \quad \text{when} \quad \left(\frac{D}{\sigma_{eff}}\right) \geq 1.5 \quad \text{.....(2.37)}$$

Chapter 3: Predicting Fluid Density in Nanopores Using Simplified Local Density/ Peng-Robinson Equation of State Model

3.1 Background and Previous Work

The fluid density is one of the most important parameters in phase behavior. Many of the correlations of the fluid properties, such as viscosity, diffusivity, compressibility factor, interfacial tension and others are developed based on fluid densities (McCain et al., 2011). The prediction of fluid density is also important in hydrocarbon-in-place calculations in shale formations due to adsorption phenomena in nanopores (Ambrose et al., 2012). In conventional formations, where pore sizes are large, fluids are stored in bulk state inside these pores. The fluid is uniformly distributed and the fluid density remains constant across the pore width under certain temperature and pressure. However, in shale formations, the fluid density is not uniformly distributed across the pore due to the confinement effects. The fluid-wall interactions between the solid porous wall and the confined hydrocarbon fluids can cause the fluid densities to deviate from the bulk values (Rangarajan et al., 1995; Mohammad et al., 2009 and Ambrose et al., 2012). The fluids can get adsorbed near the surface of the pore (mostly organic pores), forming an adsorbed phase. The fluids of the adsorbed phase can have much higher density compare to that of bulk phase under the same reservoir condition. These adsorbed fluids are an important component of hydrocarbon storage in shales. The fluid properties of the adsorbed fluids are expected to be different from the bulk fluids. Therefore, it is important to predict the density of the adsorbed fluids in shale formations and should be solved as a prior.

There are several suggestions in the literature regarding adsorbed phase density calculations. Dubinin (1960) found that the adsorbed phase density is related to the van der Waals co-volume constant "b". Menon (1968) found that the adsorbed phase density is equivalent to the liquid density that is under the same temperature and pressure conditions. Li et al. (2003) used a Langmuir-Freundlich adsorption model and found that the adsorbed phase density is temperature dependent. These references although helpful in understand the mechanisms of adsorbed, but did not give a clear way to accurately predict the adsorbed phase density and the temperature and pressure conditions considered in these references are far below shale reservoir condition. Recently, Ambrose (2011) performed a molecular simulation study to predict the density of methane in nanometer slit graphite pores under high temperature high pressure. Results from Ambrose (2011) using molecular simulation technique showed more detailed adsorption phenomena than some of the simplified models such as the Langmuir single-layer adsorption model. **Figure 3.1** shows the density profile from molecular simulation results and the results from Langmuir adsorption model. The pore is in slit shape with width equal to 2.31 nm. The temperature and pressure are 176 °F and 3043 psi. It is clear to see that multi-layer adsorption is presented according to the results from molecular simulation. While Langmuir model only assumes monolayer adsorption. It indicates that the adsorption in shale formations is somehow complicated and Langmuir model cannot show all the details.

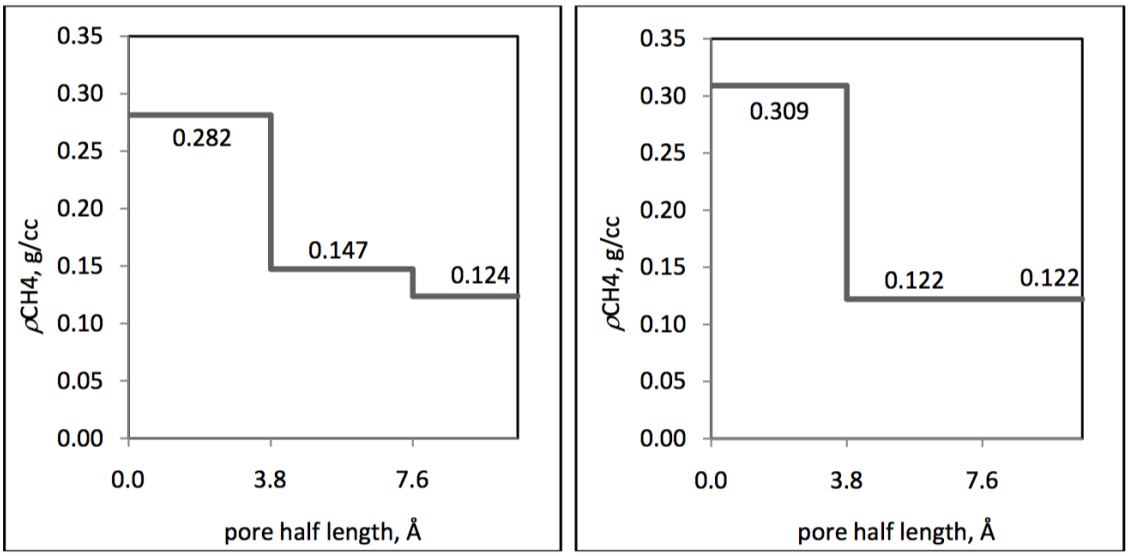

Figure 3.1 — Density profile from molecular simulation results and the results from Langmuir adsorption model (Ambrose, 2011)

Although molecular simulation provides detailed information about fluid distributions across the nanopores, the high computational cost makes it hard to deal with complicated field cases but a theoretical study. Moreover, molecular simulations cannot replace any of the analytical methods since the interpretation of the molecular simulation data, which is similar to experimental results, always requires analytical tools to achieve a good understanding of the underlying physics. On the other hand, Density Functional Theory (DFT) provides both microscopic structure and macroscopic properties of fluid from a molecular perspective, which bridges the gap between the molecular simulations and classical thermodynamics (Neimark et al., 2003; Wu, 2005). DFT is considered to be a statistical thermodynamic method and is widely used in chemical engineering, especially in the area of fluid storage in capillary systems, such as coals, catalysts and other nanoporous materials. These media have very similar characteristics compare to the shale

formations. However, few publications of unconventional shale resource studies using DFT are available in the oil and gas literature.

In this chapter, we introduce a model built upon thermodynamic equilibrium relations, named Simplified Local Density (SLD) model. The SLD model is a branch of DFT, which is first developed by Rangarajan et al. (1995) to study the physical adsorption of the different over large pressure area including the supercritical ranges. In their studies, Van der Waals EOS was used to couple with the SLD model to predict the fugacities and densities of the fluids. Mohammad et al. (2009) extended the model to a generalized Peng-Robinson EOS and predicted CO2 adsorption on coals. The two EOS parameters "a" and "b" were modified in the generalized Peng-Robinson EOS. The EOS parameter "a" was modified based on Chen et al. (1997) to consider the effects of interactions between fluid and wall on the internal pressure corrections. The other parameter "b" from Peng-Robinson EOS was generalized based on pure component adsorption data of different fluids on coals. The simulation results of their SLD model were in good match with the adsorption isotherm experimental measurements. In their more recent publication, Chareonsuppanimit et al. (2012), they tried both measurements and modeling on new Albany shale samples with N2, CH4 and CO2. They found that the SLD model was able to predict the laboratory measurements, with average absolute percentage deviations of 4% and 9% for CH4 and CO2 adsorption isotherms, respectively.

In this dissertation work, we focused on the predictions of the density distributions in slit-shaped graphite pores that represented the nanopores inside kerogen in shale formations. For simplicity and accuracy considerations, the SLD model developed by Rangarajan et

al. (1995) and the Peng-Robinson EOS with modification by Chen et al. (1997) was used. The model was extended to mixtures for the investigations of gas condensate systems.

3.2 Model Description

3.2.1 Single Component Model

The fluid density is at highest near the pores and lowest in the center portion of the pores due to the fluid-wall interactions exerted on the fluids inside the pores. This makes the fluid density a function of position with respect to the pore wall, $\rho(z)$, where z is the distance from the nearer solid wall of a slit shaped pore. The SLD-PR model was developed based on the chemical potential equality at any perpendicular position from the pore wall. The model has the following basic assumptions:

- At equilibrium, the chemical potentials at any point inside the pore are the same.
- At equilibrium, at any point where the fluid-wall interactions are not negligible, the chemical potential of that point is equal to the summation of chemical potentials resulting from fluid-fluid and fluid-wall interactions.
- The pore should have a perfect slit shape, which has uniform width.
- All the fluid molecules are considered to have a ball shape, which means that the configuration of these fluid molecules has been simplified to a sphere.
- The temperature and pressure are uniform inside the pores. The pressure of the bulk phase of the fluid (pore pressure) is adopted for calculations.

When the system is at equilibrium, the chemical potential of the adsorbed phase is equal to the chemical potential of the bulk phase. The chemical potential of the adsorbed phase

can further be expressed as the summation of the chemical potentials from the fluid-fluid interactions and fluid-solid interactions, as shown in Equation 3.1.

$$\mu_{bulk} = \mu_{ads} = \mu_{ff}(z) + \mu_{fs}(z) \quad \text{.....(3.1)}$$

In Equation 3.1, the subscripts "ads", "bulk", "ff" and "fs" refer to the adsorbed phase, the bulk phase, fluid-fluid interactions and fluid-solid interactions. For slit pores, z is the distance from point of interest to the nearer solid wall of the slit pore and L-z to be the distance to the further solid wall, where L is the width of the slit pore (see **Figure 3.2**). Then Equation 3.1 becomes:

$$\mu_{bulk} = \mu_{ads}(z) = \mu_{ff}(z) + \mu_{fs1}(z) + \mu_{fs2}(L-z) \quad \text{.....(3.2)}$$

The chemical potential of the bulk fluid can be written in terms of fugacity:

$$\mu_{bulk} = \mu_0(T) + RT\ln(\frac{f_{bulk}}{f_0}) \quad \text{.....(3.3)}$$

Where f_{bulk} is the bulk fugacity and f_0 is the fugacity at an arbitrary reference state. Similarly, the chemical potential of fluid-fluid interactions can be expressed:

$$\mu_{ff} = \mu_0(T) + RT\ln(\frac{f_{ff}(z)}{f_0}) \quad \text{.....(3.4)}$$

In Equation 3.4, $f_{ff}(z)$ is the fugacity that accounts for the fluid-fluid interactions at any position z. The fluid-solid chemical potential is, however, related to the fluid-solid pair potential:

$$\mu_{fs}(z) = N_A \Psi^{fs}(z) \quad \text{.....(3.5)}$$

Where $\Psi^{fs}(z)$ is the fluid-solid potential energy function. Lee's partially integrated 10-4 Lennard–Jones potential is used here to describe such interactions (Lee, 1988):

$$\Psi^{fs}(z) = 4\pi\rho_{atoms}\varepsilon_{fs}\sigma_{fs}^2\left(\frac{\sigma_{fs}^{10}}{5(z')^{10}} - \frac{1}{2}\sum_{i=1}^{4}\frac{\sigma_{fs}^4}{\left(z'+(i+1)\sigma_{ss}\right)^4}\right) \quad \text{.....(3.6)}$$

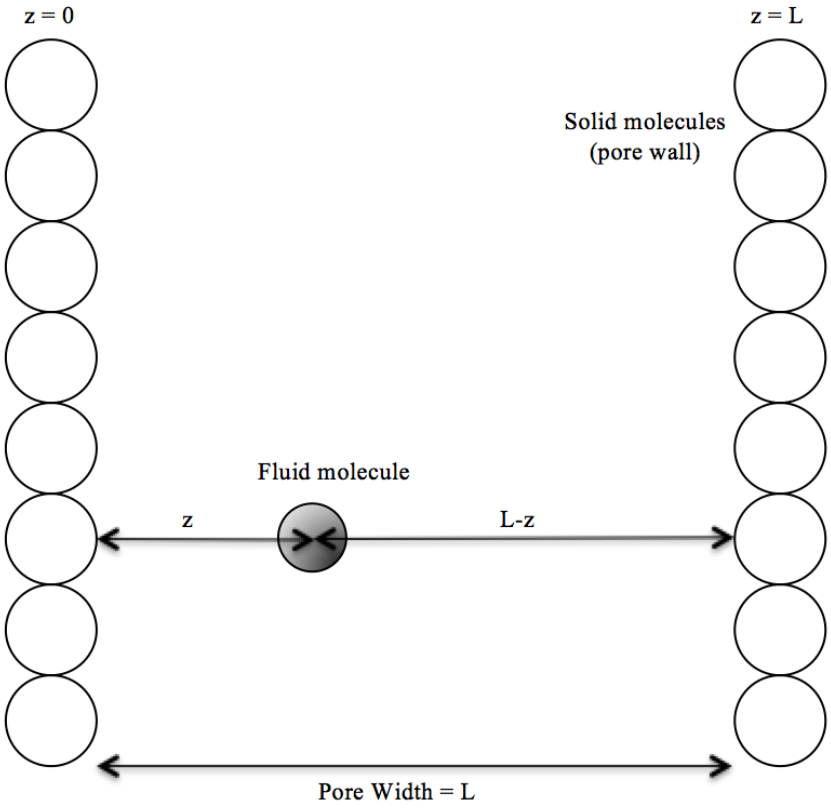

Figure 3.2 — Schematic of a slit-shaped pore model

In Equation 3.6, ρ_{atom} is the number of carbon plane atoms per unit area (38.2 atoms/nm^2), ε_{fs} is the fluid-solid interaction energy parameter and σ_{fs} is the average value of the fluid and solid molecular diameter: $\sigma_{fs} = (\sigma_{ff} + \sigma_{ss})/2$. σ_{ss} is the carbon interplanar distance which is commonly taken to be that of graphite (0.34 nm), and the virtual coordinate z' is defined by z'=z+$\sigma_{ff}/2$. The summation is over the number of solid layers from the surface to the bulk of the solid phase. It is assumed that the interaction between a fluid molecule and solid molecules after the fourth layer is very

weak, therefore, the counter i varies from 1 to 4. Now combine Equations 3.2-3.5, the relations of the bulk fugacity and fluid-fluid fugacity can be expressed as follows:

$$f_{ff}(z) = f_{bulk} \exp\left(-\frac{\mu_{fs1}(z) + \mu_{fs2}(L-z)}{RT}\right) \quad \text{.....(3.7)}$$

In this model, fugacities are calculated using PR-EOS:

$$\frac{P}{\rho RT} = \frac{1}{(1-\rho b)} - \frac{a\rho}{RT\left[1+\left(1-\sqrt{2}\right)\rho b\right]\left[1+\left(1+\sqrt{2}\right)\rho b\right]} \quad \text{.....(3.8)}$$

The bulk fugacity can be calculated using PR-EOS in terms of bulk fluid density:

$$\ln\frac{f_{bulk}}{P} = \frac{b\rho_{bulk}}{1-b\rho_{bulk}} - \frac{a\rho_{bulk}}{RT\left(1+2b\rho_{bulk}-b^2\rho_{bulk}^2\right)} - \ln\left[\frac{P}{RT\rho_{bulk}} - \frac{Pb}{RT}\right] - \frac{a}{2\sqrt{2}bRT}\ln\left[\frac{1+\left(1+\sqrt{2}\right)\rho_{bulk}b}{1+\left(1-\sqrt{2}\right)\rho_{bulk}b}\right] \text{.(3.9)}$$

The fugacity that accounts for the fluid-fluid interactions is expressed as in Equation 3.10.

$$\ln\frac{f_{ff}}{P} = \frac{b\rho_{local}(z)}{1-b\rho_{local}(z)} - \frac{a_{ff}(z)\rho_{local}(z)}{RT\left(1+2b\rho_{local}(z)-b^2\rho_{local}^2(z)\right)} - \ln\left[\frac{P}{RT\rho_{local}(z)} - \frac{Pb}{RT}\right] - \frac{a_{ff}(z)}{2\sqrt{2}bRT}\ln\left[\frac{1+\left(1+\sqrt{2}\right)\rho_{local}(z)b}{1+\left(1-\sqrt{2}\right)\rho_{local}(z)b}\right] \text{..(3.10)}$$

In Equation 3.10, the parameter "a" in PR-EOS has been modified as a function of position rather than constant to consider the confinement effects on the fluids. This modification is based on Chen et al. (1997). In their paper, they claimed that the parameter "a" in PR-EOS depends on the position of interest inside the pore, z, as well as the dimensionless pore width L/σ_{ff}, where L is pore width and σ_{ff} is the Van der Waals molecular diameter of the fluid. The purpose of this modification is to account for the variation of attraction potential with respect to position inside the pore for an inhomogeneous fluid. More details can be found in Rangarajan et al. (1995). The expressions of the correction on the parameter "a" are shown in **Appendix A**. From these expressions, it is clear to see that for a fixed pore size with a particular fluid, the parameter "a" only depends on position z.

Finally, the local density at any position z can be obtained from Equation 3.10. In Equation 3.10, the fluid-fluid fugacity can be calculated from Equations 3.6-3.8 and Equation 3.9. The local density profile across the pore can then be obtained by discretizing the pore into small segments and calculating an average $\rho_{local}(z)$ for each segment. An algorithm of local density profile calculations for pure component using SLD-PR model is shown in **Figure 3.3**.

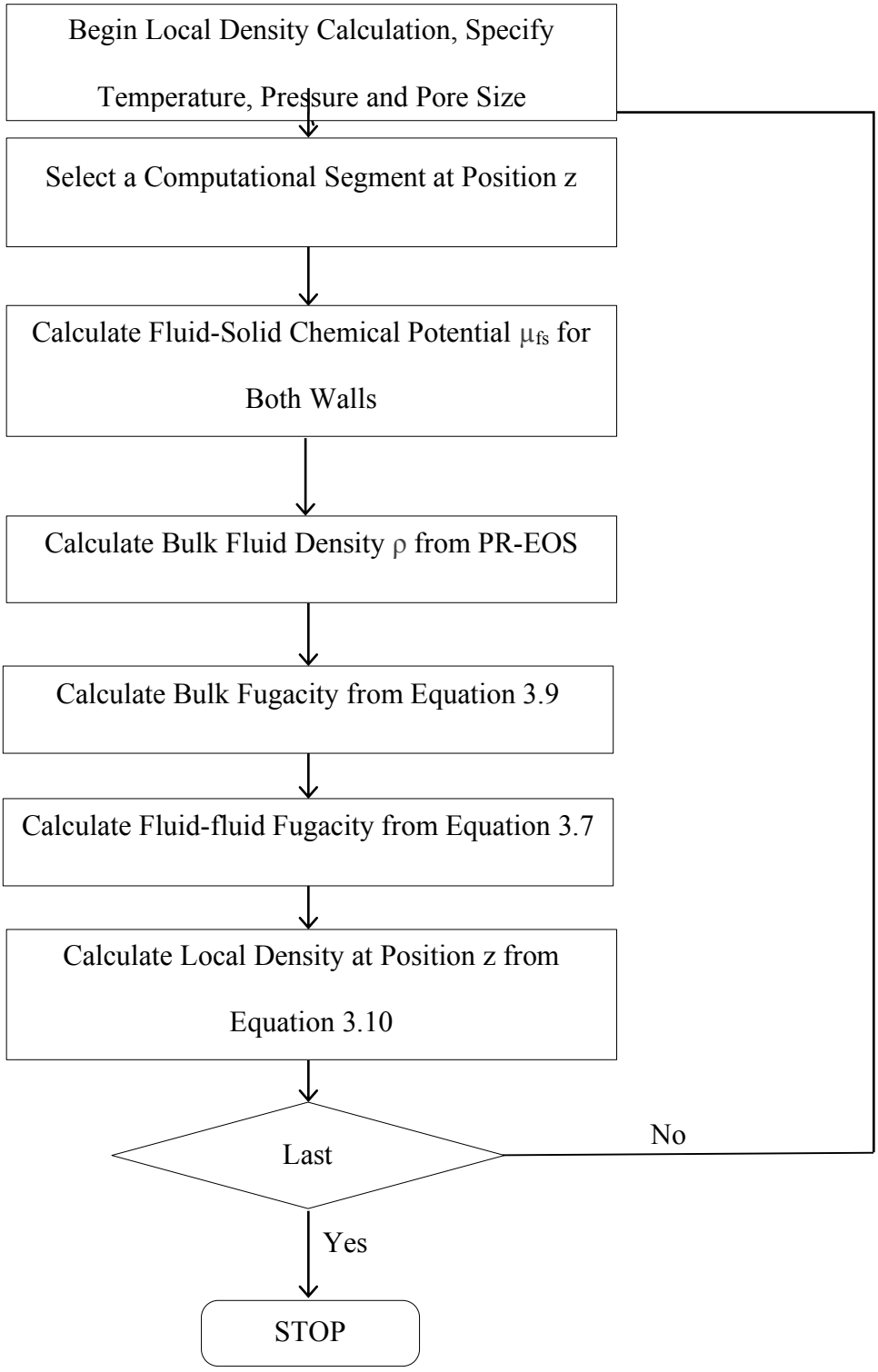

Figure 3.3 — Flow chart for SLD-PR single component model algorithm

3.2.2 Multi-Component Model

For fluid mixtures, the thermodynamic relations and equilibrium still apply for each component. That is, for component i, the partial bulk fugacity and partial fluid-fluid fugacity should still obey the relation expressed in Equation 3.7:

$$f_i^{ff}(z) = f_i^{bulk} \exp\left(-\frac{\mu_i^{fs1}(z) + \mu_i^{fs2}(L-z)}{RT}\right) \quad \text{.....(3.11)}$$

Where the partial bulk fugacity and partial fluid-fluid fugacity for component i can be obtained using PR-EOS similar to Equations 3.9 and 3.10:

$$\ln\frac{f_i^{bulk}}{x_i P} = \frac{b_i}{b}\left(\frac{P}{RT\rho_{bulk}} - 1\right) - \ln\left[\frac{P}{RT\rho_{bulk}} - \frac{Pb}{RT}\right] + \frac{a}{2\sqrt{2}bRT}\left(\frac{b_i}{b} - \frac{2\sum_j y_j a_{ij}}{a}\right)\ln\left[\frac{1+\left(1+\sqrt{2}\right)\rho_{bulk}b}{1+\left(1-\sqrt{2}\right)\rho_{bulk}b}\right] \quad \text{..(3.12)}$$

$$\ln\frac{f_i^{ff}}{y_i(z)P} = \frac{b_i}{b}\left(\frac{P}{RT\rho_{local}(z)} - 1\right) - \ln\left[\frac{P}{RT\rho_{local}(z)} - \frac{Pb}{RT}\right] + \frac{a_{ff}(z)}{2\sqrt{2}bRT}\left(\frac{b_i}{b} - \frac{2\sum_j y_j a_{ij}^{ff}(z)}{a_{ff}(z)}\right)\ln\left[\frac{1+\left(1+\sqrt{2}\right)\rho_{local}(z)b}{1+\left(1-\sqrt{2}\right)\rho_{local}(z)b}\right] \quad \text{(3.13)}$$

The parameter x_i represents the composition of component i in bulk phase. While the parameter $y_i(z)$ is the composition of component i at position z in adsorbed phase. The mixing rules for the EOS parameters a and b are given as:

$$a = \sum_{i=1}^{n_c}\sum_{j=1}^{n_c} x_i x_j a_{ij} \quad \text{.....(3.14)}$$

$$a_{ij} = \left(1-k_{ij}\right)\sqrt{a_i a_j} \quad \text{.....(3.15)}$$

$$b = \sum_{i=1}^{n_c} x_i b_i \quad \text{.....(3.16)}$$

Where k_{ij} is the binary interaction parameters (BIPs) between fluid-fluid molecules that is used to describe the interactions between asymmetric mixtures. The parameter a_{ff} describing the fluid-fluid interactions can have the similar form as parameter a:

$$a_{ff}(z) = \sum_{i=1}^{n_c}\sum_{j=1}^{n_c} y_i(z)y_j(z)a_{ij}^{ff}(z) \quad \text{.....(3.17)}$$

$$a_{ij}^{ff}(z) = \left(1-k_{ij}\right)\sqrt{a_i^{ff}(z)a_j^{ff}(z)} \quad \text{.....(3.18)}$$

For any fluid mixtures, in order to calculate the fluid composition and fluid local density at any position z, one needs to define the fluid composition of the bulk state. Once the fluid composition of the bulk state for each component, x_i (x=1,2,3….nc), is known, the partial fugacity f_i^{bulk} of each component can be calculated from Equation 3.12. The chemical potentials account for the fluid-wall interaction between component i and both pore walls can be calculated from Lee's potential using Equations 3.5 and 3.6. Then the partial fluid-fluid fugacity f_i^{ff} can be obtained from Equation 3.11. After f_i^{bulk} and f_i^{ff} are calculated, the fluid composition $y_i(z)$ and fluid local density $\rho_{local}(z)$ can be solved from Equation 3.13 plus the constraint on mole fractions, $\sum_i y_i(z) = 1$. For i components, there are i+1 unknowns: $y_i(z)$ for each component i and $\rho_{local}(z)$. And there should be i+1 equations: Equation 3.13 for each component i plus the mole fraction constraint. Repeat the above procedure for each position z from $\sigma_{ff}/2$ to $L - \sigma_{ff}/2$ with an increment of dz will give the density profile across the pore with a fixed width L. Note that the regions between 0 to $\sigma_{ff}/2$ and $L - \sigma_{ff}/2$ to L are inaccessible due to the size of the fluid molecules.

Chapter 4: Studying Confined Fluid Phase Behavior Using Proposed Models

The previous two chapters were focused on the development of the mathematical formulations that considered confinement effects on phase behavior calculations. In Chapter 2 we introduced the modification of EOS to include the fluid-wall interactions, while in Chapter 3 we discussed the SLD-PR model that can predict the fluid density at any position inside a confined pore space. In this chapter, we first compared the results of the models with literature data for validation purposes. Then we performed flash calculations using the modified Peng-Robinson EOS to show the confinement effects on phase equilibrium of a hydrocarbon mixture that contains C1, nC4 and C10. Last, we calculated fluid density profiles using the SLD-PR model in slit pores with fixed width for different fluids. Sensitivity analysis was performed to investigate the effects of temperature, pressure, fluid composition and pore size on the density profiles.

4.1 Model Validation

4.1.1 Validation of Modified EOS for Phase Behavior of Confined Fluid

In this section, the bubble point pressures of a C1/nC5 mixture in nanopores were calculated using Modified Peng-Robinson EOS and compared the results with experimental data. Sigmund et al. (1973) proposed bubble point pressures for a methane-n-pentane binary system under effects of curvature (confinement effect) for different methane compositions. The laboratory measurements of Sigmund et al. (1973) showed that bubble point pressures suppressed with confined pores. The smaller the pore size, the more the bubble point pressure suppression was observed. **Table 4.1** shows the bubble

point pressures of the C1/nC5 system with different C1 composition in different pore sizes calculated by Modified Peng-Robinson EOS as well as the measurements from Sigmund et al. (1973). The mixing rules used for the EOS parameters were listed in Chapter 2 as Equations 2.12, 2.13 and 2.15. The Binary Interaction Parameters (BIPs) K_{ij} and J_{ij} used in parameters a and c were obtained by using the least squares fitting to the experimental data. The values of K_{ij} and J_{ij} were found to be [0 0.021; 0.021 0] and [0 2.1; 2.1 0], respectively and the coefficients of determination, r^2, for bulk, 100 nm and 10 nm, were equal to 0.002589, 0.002183 and 0.001557, respectively.

It is clear to see from Table 4.1 that both the simulation results and the experimental measurements show the decrease in bubble point pressure with decreasing pore size, regardless of the C1 composition. However, it is also observed that at high bubble point pressure range, the difference between the simulation and experimental results becomes larger when the C1 composition in the mixture increases. And this has led us to have more investigations on the BIPs.

The BIPs are the empirical or semi-empirical parameters that are required in the use of any cubic EOS. The BIPs are used along with the mixing rules that are in conjunction with cubic EOS to represent fluid mixtures. The derivation of the BIPs has been studied in the past decades and many methods have been developed. Peng and Robinson (1976) obtained the values of the BIPs from vapor-liquid equilibrium experimental data. However, for many complex and nonideal systems, fixed BIPs may not do the job. It has been stated back from 1970s that the BIPs depend on physical parameters, such as temperature (Schulze 1993 and Estévez et al., 1988) and fluid composition

(Panagiotopoulos and Reid, 1986; Adachi and Sugie, 1986; Stryjek and Vera 1986; Łencka and Andrzej, 1991).

To have better performance of the simulation results, the BIPs were corrected and became composition dependent variables as follows:

$$k_{ij} = \begin{bmatrix} 0 & 0.029x_{C5} \\ 0.029x_{C5} & 0 \end{bmatrix} \quad \text{.....(4.1)}$$

$$J_{ij} = \begin{bmatrix} 0 & 2.9x_{C5} \\ 2.9x_{C5} & 0 \end{bmatrix} \quad \text{.....(4.2)}$$

Where x_{C5} represents the composition of n-pentane in the mixture. **Table 4.2** gives the simulation results using the new BIPs. We see better performance of predictions at high bubble point pressure range especially for bulk and 100 nm. The coefficients of determination, r^2, for bulk, 100 nm and 10 nm reduced to 2.3336e-4, 5.0953e-4 and 0.001465, respectively. Although it is not sufficient to draw conclusions on the generalizations of the composition dependent BIPs based on the limited data. Such corrections, however, gives the train of thought in the PVT calculations as an example. That is, in complex systems, the BIPs can be variable dependent parameters rather than fixed numbers to have better predictions in the phase behavior.

TABEL 4.1—Comparison of Simulation Results from Modified PR-EOS Model and Experimental Data from Sigmund et al. (1973) --- Fixed BIPs

	Bulk		100 nm		10 nm	
xCH4	Sigmund	mPR-EOS	Sigmund	mPR-EOS	Sigmund	mPR-EOS
0.0288	99.53	98.14	98.62	97.82	90.89	93.43
0.0628	200.75	198.34	199.09	197.71	184.83	186.73
0.0957	301.05	297.47	298.7	296.53	278.45	279.28
0.1282	402.4	398.02	399.41	396.77	373.66	372.93
0.1911	604.93	600.02	600.8	598.14	565.22	561.12
0.2508	804.65	800.64	799.62	798.14	756.35	748.26
0.3077	1001.14	999.7	995.45	996.57	946.49	934.78
0.3748	1238.58	1244.32	1232.26	1240.55	1178.04	1164.02
0.439	1468.08	1487.03	1461.97	1482.32	1409.52	1392.3
0.5041	1697.94	1738.41	1691.69	1733.08	1638.18	1629.89
0.5788	1960.32	2026.49	1955.06	2020.22	1913.11	1904.48

TABEL 4.2—Comparison of Simulation Results from Modified PR-EOS Model and Experimental Data from Sigmund et al. (1973) --- Corrected BIPs

	Bulk		100 nm		10 nm	
xCH4	Sigmund	mPR-EOS	Sigmund	mPR-EOS	Sigmund	mPR-EOS
0.0288	99.53	98.14	98.62	97.82	90.89	93.43
0.0628	200.75	198.34	199.09	197.71	184.83	186.73
0.0957	301.05	297.47	298.7	296.53	278.45	279.28
0.1282	402.4	398.02	399.41	396.77	373.66	372.93
0.1911	604.93	600.02	600.8	598.14	565.22	561.12
0.2508	804.65	800.64	799.62	798.14	756.35	748.26
0.3077	1001.14	999.7	995.45	996.57	946.49	934.78
0.3748	1238.58	1244.32	1232.26	1240.55	1178.04	1164.02
0.439	1468.08	1487.03	1461.97	1482.32	1409.52	1392.3
0.5041	1697.94	1738.41	1691.69	1733.08	1638.18	1629.89
0.5788	1960.32	2026.49	1955.06	2020.22	1913.11	1904.48

4.1.2 Validation of SLD-PR model for Density Profiles of Confined Fluid

The purpose of this section is to test the SLD-PR model against the results available from similar scenarios in the literature to check the accuracy of the model. Ambrose (2011) obtained pure methane density profiles for different pore widths under 176 °F and 3043 psi using molecular dynamic techniques. The density profiles obtained by Ambrose (2011) are presented in two ways: number-density profiles and discrete mass density profiles. The number-density profiles are obtained directly from molecular simulation by counting the number of methane molecules for every 0.38 nm wide integral across the pore. The number density was then converted to local mass density to obtain the discrete mass density profile. **Figure 4.1** gives the half methane density profiles in a 3.73 nm wide pore calculated from molecular dynamics performed by Ambrose (2011) as an example to show the shape of number-density profile (left) and discrete mass density profile (right). Here, the mass density profiles from molecular simulation to those obtained from SLD model since in SLD model the number of molecules is not defined. However, the density profiles calculated from SLD model are continuous profiles rather than discrete profiles. So the first thing to do is to average the density within each 0.38 nm wide integral across the pore. **Figure 4.2** shows the continuous methane mass density profile calculated from SLD model (left) and the equivalent discrete mass density profile (right) in a 2.31 nm pore under 176 °F and 3043 psi. Note that in SLD model, the regions between 0-0.19 nm and 2.12-2.31 nm are inaccessible due to the size of the methane molecules. Therefore, discrete density layers for the two 0.38-nm intervals close to either wall are averaged based on the densities within half interval length in the range between 0.19-0.38 nm and 1.93-2.12 nm, respectively, instead of the full interval length.

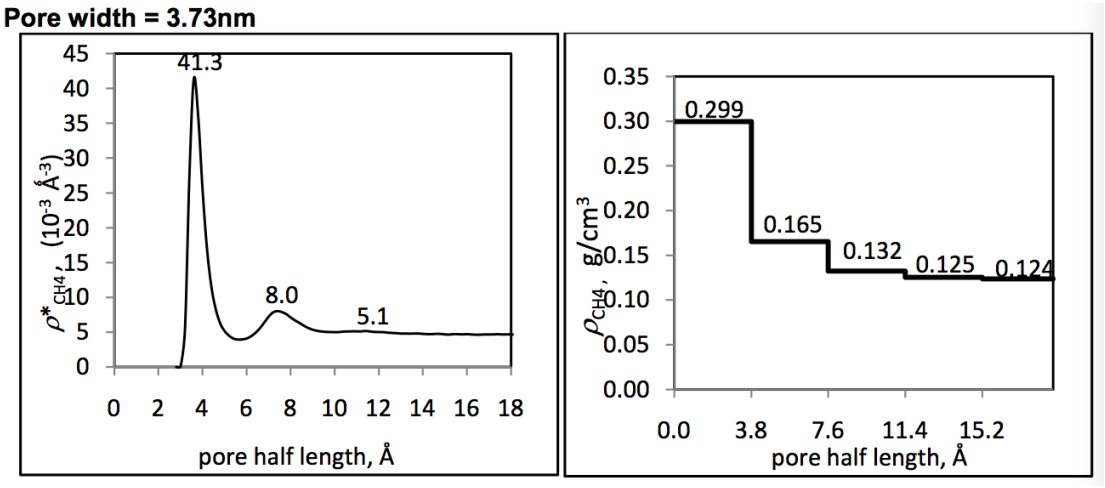

Figure 4.1—Number-density profile (left) and discrete mass density profile (right) of methane under 176 °F and 3043 psi obtained by Ambrose (2011)

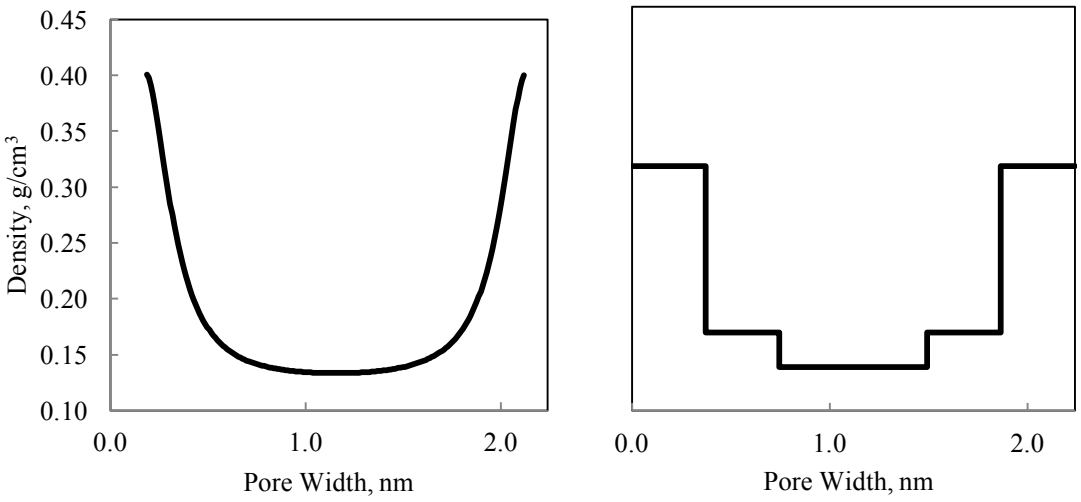

Figure 4.2—Continuous methane mass density profile calculated from SLD model (left) and the equivalent discrete mass density profile (right) in a 2.31 nm pore under 176 °F and 3043 psi

Figure 4.3 and **Figure 4.4** compare the discrete mass density profiles calculated from SLD model and Ambrose (2011) under 176 °F and 3043 psi in 3.73-nm pore and 2.31-

nm pore, respectively. Only half of the pore is shown because the density profiles are symmetric in a slit shaped pore. It is clear to see that the agreement is good between molecular simulation and SLD model values of methane densities in each layer in both 3.73-nm pore and 2.31-nm pore. **Table 4.3** shows the relative errors for each layer in both 3.73-nm pore and 2.31-nm pore. Note that layer 1 represents the interval that is closest to the wall on the left. It shows that the relative errors are within 5% for all the layers except layer 1 in 2.31-nm pore (6.85%). From the results, it may be concluded that the results calculated from SLD model are validated and in agreement with the results obtained from molecular dynamics performed by Ambrose (2011).

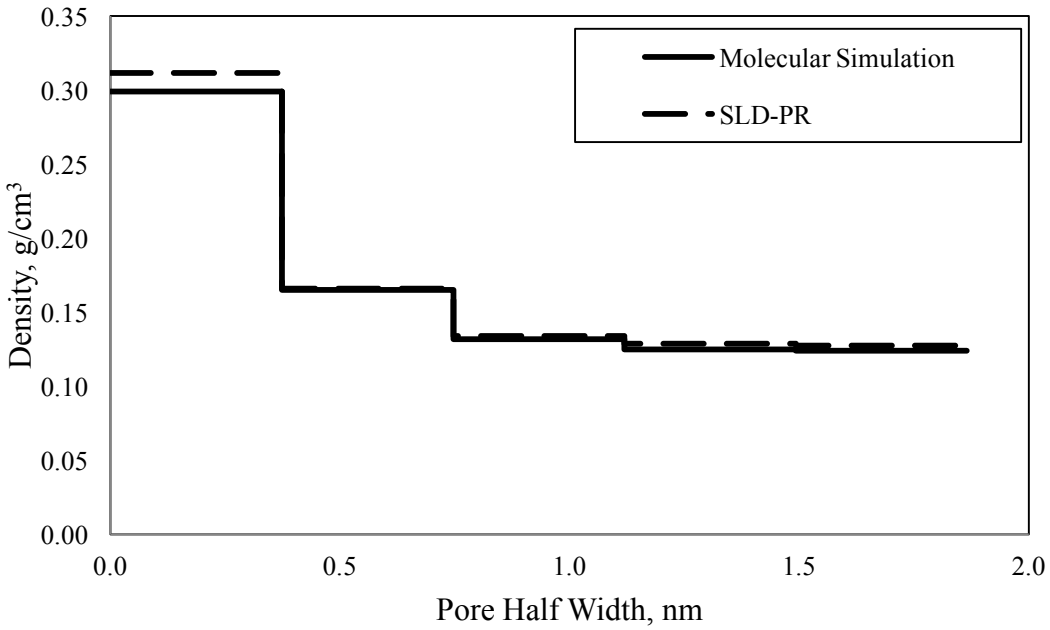

Figure 4.3—Comparison of density profiles of methane in a 3.73 nm-width slit pore at 176 °F and 3043 psi obtained from both SLD model and molecular dynamics performed by Ambrose (2011)

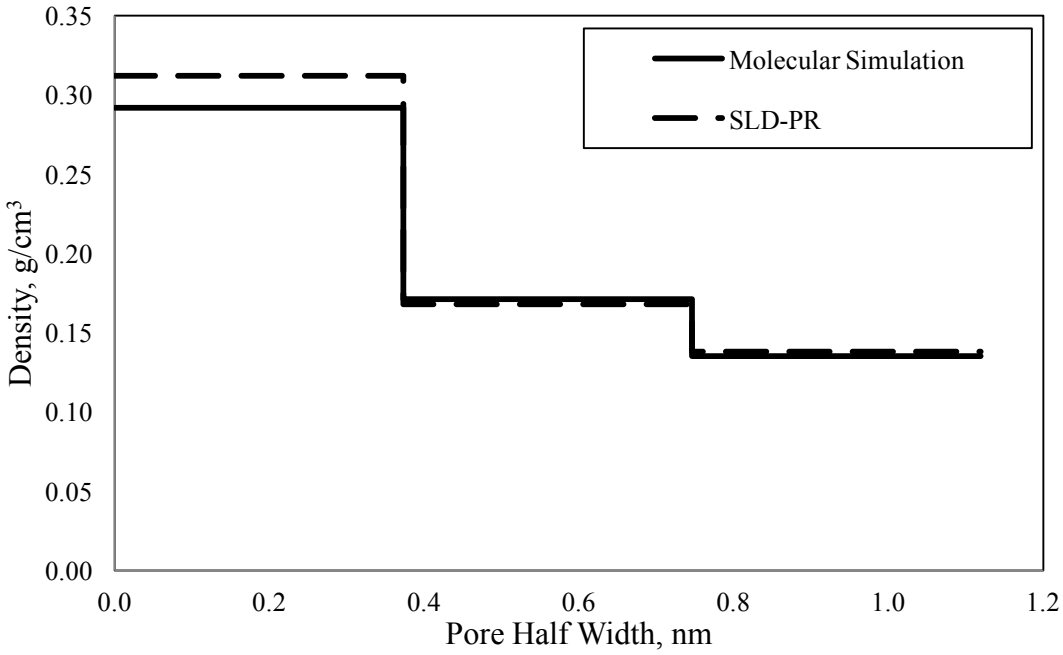

Figure 4.4—Comparison of density profiles of methane in a 2.31 nm-width slit pore at 176 °F and 3043 psi obtained from both SLD model and molecular dynamics performed by Ambrose (2011)

TABEL 4.3— Relative Errors of Methane Densities Calculated from SLD Model Compare to Ambrose (2011)

3.73-nm Pore	Relative Error	2.31-nm Pore	Relative Error
Layer 1	4.25 %	Layer 1	6.85 %
Layer 2	0.61 %	Layer 2	1.75 %
Layer 3	1.36 %	Layer 3	2.22 %
Layer 4	2.96 %		
Layer 5	2.82 %		

4.2 Vapor-Liquid Equilibrium Calculations for Confined Fluid

4.2.1 Flash Calculations

Flash calculations determine the number of equilibrium phases as well as the phase properties in a system with given temperature, pressure and overall composition. For a gas-condensate reservoir, where gas and oil are presented, flash calculations can be used to process with Vapor-Liquid Equilibrium (VLE) calculations. With known reservoir properties (temperature, pressure and overall composition), the composition of each component in both liquid phase and vapor phase and the mole fractions of liquid and vapor phases in the reservoir are calculated by performing flash calculations.

As mentioned previously, the fluid phase behavior will change when the fluids are confined inside nanopores in shale formations. This phase behavior change includes the shift in VLE. Thus, conventional flash calculation is no longer valid for confined fluids. In order to account for the confinement effects, the EOS used in conventional flash calculation is replaced by the modified PR EOS developed in Chapter 2.2.2. A flash calculation simulator using the modified PR EOS was developed and discussed.

Before the flash calculations, one needs to determine whether the fluid will actually split into multiple phases or remain as a single phase at specified composition, pressure and temperature. If the fluid is stable in single phase, there will be no meaning for the flash calculations. Li and Nghiem (1982) and Nghiem (1983) showed that the Gibbs tangent-plane criterion could be used to establish the thermodynamic stability of a given phase. Whitson and Brulé (2000) mentioned that for a fluid with a given composition, pressure and temperature, it favors the state that gives the minimum Gibbs energy. That is, the

fluid will either remain as a single phase or split to more than one phases, depending on the Gibbs energy of the system that gives a lower value. Therefore, it is necessary to check the stability of the fluid at given composition, temperature and pressure before performing the flash calculations.

The stability test that involved a successive-substitution algorithm was first developed by Michelsen (1982), known as Michelsen stability test. A step-by-step algorithm of the Michelsen stability test can be found in Whitson and Brulé (2000) and was adopted here. If the results show that the fluid has two phases under certain temperature and pressure, an initial guess of the K-values will be generated. Note that the K-value represents the ratio of composition of one component in the vapor phase to the composition of that component in the liquid phase at equilibrium. Once the initial guess of the K-values is obtained, one can perform the flash calculations by equating the fugacities of each component in the two phases. **Figure 4.5** shows the flow chart of the flash calculations using successive substitution algorithm (more details about the flash calculation algorithms can be found in Jamili, 2010). The modified PR EOS was used in the flash calculations. Such flash calculations will be sensitive to pore sizes and is able to capture the composition change under confinement. In this section, first the results of the new flash calculations simulator are compared to other calculations as well as experimental measurements at bulk conditions in the literature. Then the effects of pore size on the flash calculation results were investigated to show the VLE shift of the confined fluids.

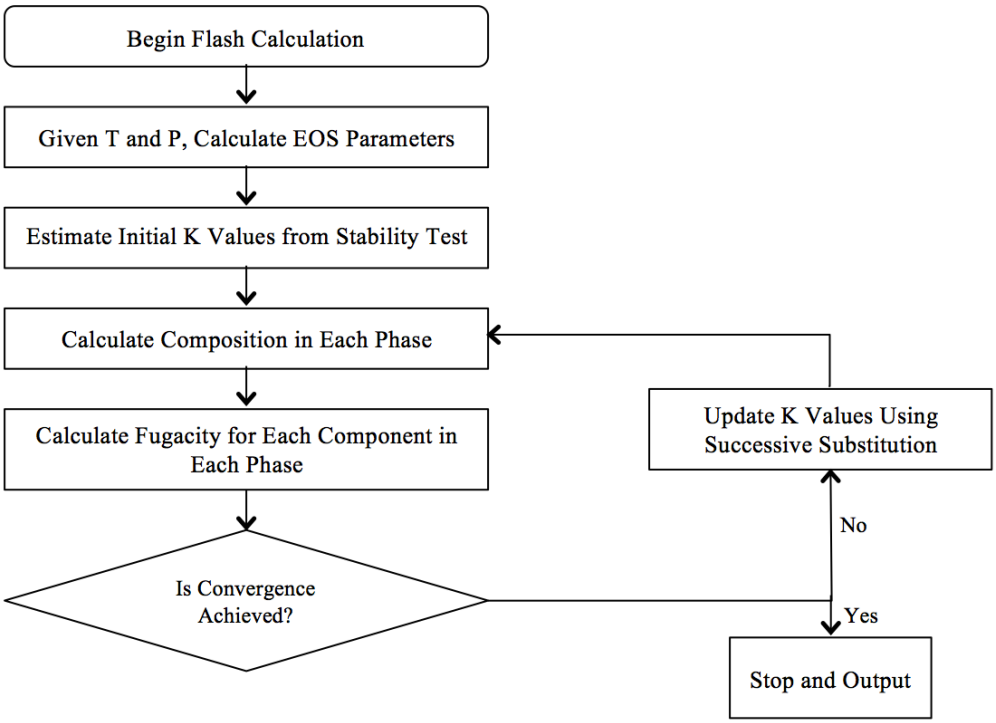

Figure 4.5—Flow chart of the flash calculation

The flash calculation simulator was validated against the flash calculation results from McCain (1990) and the experimental data from Sage et al. (1950). A ternary mixture contains methane, n-butane and decane was flashed under the pressure of 1000 psi and the temperature of 160 °F. **Table 4.4** shows the mixture composition and critical properties reported in McCain (1990). **Table 4.5** gives the BIPs of the mixture from McCain (1990). The BIPs are assumed to be independent of pressure, temperature and composition and are treated as fixed values for simplicity. **Table 4.6** shows the gas mole fraction, gas and oil compressibility factors calculated from this work and McCain (1990). **Table 4.7** shows the gas and oil compositions from this work and experimental data from Sage et al. (1950). Note that the pore size in the modified PR-EOS is set to be

infinity in the calculation so that the fluid-wall interactions are zero. From the comparison, it is clear to see that the results from this work are in good agreement with the flash calculation results from McCain (1990) and experimental data from Sage et al. (1950) in the bulk state.

Table 4.4—Compositions and Physical Properties of C1-nC4-C10 (McCain, 1990)

Component	Composition	Critical Temp. (°F)	Critical Pressure (psi)	Molecular Weight (lb_m/lb-mol)	Acentric Factor
CH_4	0.5301	-116.67	666.4	16.043	0.0104
n-C_4H_{10}	0.1055	305.63	550.6	58.12	0.1995
$C_{10}H_{22}$	0.3644	652.03	305.2	142.285	0.4898

Table 4.5—Binary Interaction Coefficients of C1-nC4-C10 (McCain, 1990)

	CH_4	n-C_4H_{10}	$C_{10}H_{22}$
CH_4	0	0.02	0.04
n-C_4H_{10}	0.02	0	0
$C_{10}H_{22}$	0.04	0	0

Table 4.6—Comparison of Fluid Properties from This Work and McCain (1990) Pressure=1000 psi, Temperature=160 °F		
Fluid Properties	McCain (1990)	This Work
Gas mole fraction	0.4015	0.4011
Gas compressibility factor	0.3922	0.3921
Oil compressibility factor	0.9051	0.9048

Table 4.7—Compositions of Oil and Gas from This Work and Sage et al. (1950) Pressure=1000 psi, Temperature=160 °F				
Component	Gas mole fraction (this work)	Gas mole fraction (Sage et al., 1950)	Oil mole fraction (this work)	Oil mole fraction (Sage et al., 1950)
CH_4	0.9613	0.963	0.2413	0.242
n-C_4H_{10}	0.0367	0.036	0.1516	0.152
$C_{10}H_{22}$	0.0021	0.0021	0.6071	0.606

Now we change the pore size to investigate the confinement effects on fluid phase behavior. For the same ternary mixture containing methane, n-butane and decane under the pressure of 1000 psi and the temperature of 160 °F, the pore size is decreased from 1000 nm (considered as bulk) to 2 nm. **Table 4.8** and **Table 4.9** show the gas and oil compositions in different pore sizes, respectively. **Table 4.10** gives gas mole fraction, gas

and oil compressibility factors in different pore sizes. If we plot gas mole fraction against pore size, as shown in **Figure 4.6**, we can see that the gas mole fraction increases with decreasing pore size. Such changes become much more rapid when the pore diameter is less than 10 nm. This shows that the confinement effects make this ternary mixture behaves more like a dry gas. **Figure 4.7** shows the K-values for each component in different pore sizes. From the figure, we can observe that the K-value of methane is almost constant at any pore sizes regardless of the pore size, while the K-values for n-butane and decane tend to increase in smaller pores, especially when the pore diameter is less than 10 nm. The K-value of n-butane increased from 0.24 at bulk to 0.38 when the pore size is decreased to 2 nm. While, the K-value of decane increased from 0.0035 at bulk to 0.014 when confined in 2 nm pores, with 4 times increase. These results show that heavier components, such as n-butane and decane have more tendencies to go to the vapor phase in smaller pores than lighter component, such as methane.

Based on the results of the flash calculations for the confined fluids, we can see that the confinement effects have strong impact on fluid phase behavior especially when the pore size is less than 10 nm. If the fluid has both vapor and liquid phase at equilibrium at given temperature and pressure, the confinement effects will shift the fluid more to the vapor phase. If the fluid has more than one component, the confinement effects have larger impact on heavier component, that is, the K-value of heavier components increase much more rapidly than the other components when the pore size decreases.

Table 4.8—Gas Composition of Each Component in the Mixture in Different Pore Sizes Pressure=1000 psi, Temperature=160 °F

Pore Diameter, nm	Gas Composition, fraction		
	Methane	n-Butane	Decane
1000	0.9612	0.0367	0.0021
100	0.9612	0.0367	0.0021
50	0.961	0.0369	0.0021
30	0.9608	0.0371	0.0022
15	0.96	0.0377	0.0023
10	0.9591	0.0384	0.0025
8	0.9583	0.0391	0.0026
6	0.9569	0.0402	0.0029
5	0.9556	0.0413	0.0031
4	0.9534	0.0429	0.0036
3	0.9492	0.0461	0.0047
2	0.9377	0.0537	0.0086

Table 4.9—Oil Composition of Each Component in the Mixture in Different Pore Sizes Pressure=1000 psi, Temperature=160 °F

Pore Diameter, nm	Oil Composition, fraction		
	Methane	n-Butane	Decane
1000	0.2413	0.1516	0.6071
100	0.2413	0.1516	0.6071
50	0.2413	0.1515	0.6072
30	0.2413	0.1514	0.6073
15	0.2414	0.151	0.6076
10	0.2414	0.1506	0.608
8	0.2415	0.1503	0.6083
6	0.2416	0.1496	0.6088
5	0.2418	0.149	0.6091
4	0.2423	0.148	0.6097
3	0.2434	0.1461	0.6104
2	0.2482	0.1413	0.6105

Table 4.10—Gas Mole Fraction, Gas and Oil Compressibility Factors Against Pore Sizes Pressure=1000 psi, Temperature=160 °F

Pore Diameter, nm	Gas Fraction	Gas Compressibility Factor	Oil Compressibility Factor
1000	0.4011	0.9048	0.3921
100	0.4012	0.9049	0.3922
50	0.4012	0.9051	0.3924
30	0.4014	0.9053	0.3926
15	0.4018	0.9062	0.3934
10	0.4022	0.9071	0.3944
8	0.4026	0.9079	0.3952
6	0.4033	0.9093	0.3967
5	0.4039	0.9105	0.3981
4	0.4047	0.9124	0.4003
3	0.4062	0.9157	0.4045
2	0.4088	0.9221	0.4151

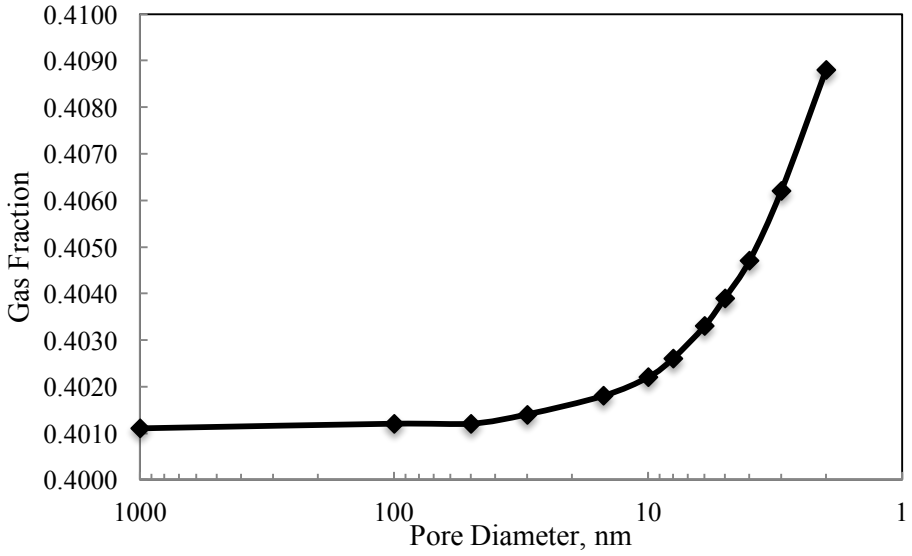

Figure 4.6—Gas fraction of the mixture (53.01% C1/ 10.55% nC4/ 36.44% C10) against pore sizes under 1000 psi and 160 °F

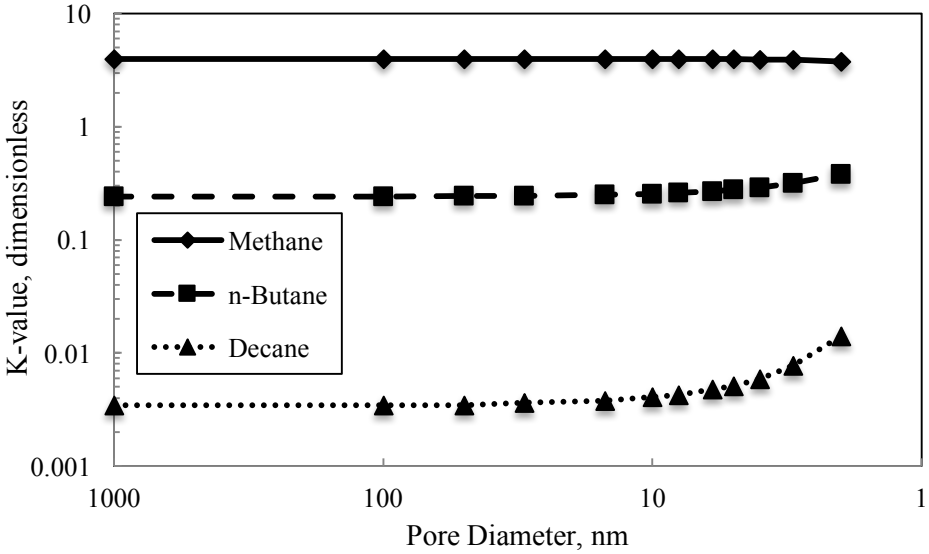

Figure 4.7—K-values of each component in the mixture (53.01% C1/ 10.55% nC4/ 36.44% C10) versus pore sizes under 1000 psi and 160 °F

4.2.2 Two-Phase Envelope Calculations

A two-phase envelope is a temperature-pressure phase diagram generated by a series of saturation pressures, including bubble point pressures and dew point pressures, for a multi-component mixture. For a given temperature, the bubble point pressure is the pressure where the first bubble of vapor is formed from the liquid. Similarly, the dew point pressure is the pressure where the first drop of liquid is formed from the vapor at certain temperature. Therefore, a two-phase envelope separates the fluid mixture into two regions: the region inside the envelope is the two-phase region, where the mixture is presented as a combination of liquid and vapor; the other region is the region outside the envelope, where only single phase (either pure liquid or pure vapor) exists. The phase envelope calculation is important in the petroleum industry, as it can predict at what conditions the condensation or evaporation can happen. The shape of the phase envelope can determine the type of the reservoirs, such as dry gas reservoirs, gas-condensate reservoirs, retrograde reservoirs, volatile reservoirs or black oil reservoirs, as shown in **Figure 4.8**. In this section, we focus on the gas-condensate system and investigate the effects of confinement on the gas-condensate system in shale resources.

For the same ternary mixture that contains methane, n-butane and decane, a two-phase envelope can be calculated based on Whitson and Brulé (2000). The original PR-EOS was replaced by the modified PR-EOS for pore size considerations. The average effects of pore size were included in the parameter c in the modified PR-EOS, shown in Equation 2.22. **Figure 4.9** shows the two-phase envelopes in different pore sizes. It is clear to see that the confinement effects can change the saturation pressures of the fluid mixtures in nanoscale pores. The two-phase region of the fluid mixture tends to shrink in smaller

pores when temperature is greater than 100 °F, resulting in behavior more like a dry gas. On the other hand, at temperature lower than around 100 °F, the saturation pressures tend to increase in smaller pores. In a two-phase envelope, the dew point line is separated into two parts by the cricondentherm point, one called upper dew point line where the pressure is higher than the cricondentherm point pressure. The other is the lower due point line, where the dew point pressures on the line are lower than the cricondentherm point pressure. Note that a cricondentherm point is the point with the maximum temperature at which condensation takes place.

For upper dew point line, the dew point pressures become lower in small pores where the pore size is reduced to 10 nm or even smaller. For example, the dew point pressure at 300 °F at bulk is 2780 psi, and is reduced to 2720 psi, 2610 psi and 2130 psi when the pore size is equal to 10, 5, 2 nm, respectively. There is a difference of 23% between the dew point pressures for bulk and in pores that have 2 nm in size. On the contrary, the dew point pressures are higher in smaller pores for lower dew point line. The dew point pressure at 400 °F changed from 80 psi at bulk to 400 psi for 2-nm pores, where we saw a dramatic increase. The change in dew point line can affect the prediction of condensate dropout. If we have a depleting path shown as the black line in **Figure 4.9** that goes through the phase envelopes, it is clear that the depleting path intersects with different phase envelopes at different pressures, which means different times. Since the phase envelope shrinks for smaller pores, one can expect the condensate dropout occurs at a later time when depleting a gas-condensate shale reservoir.

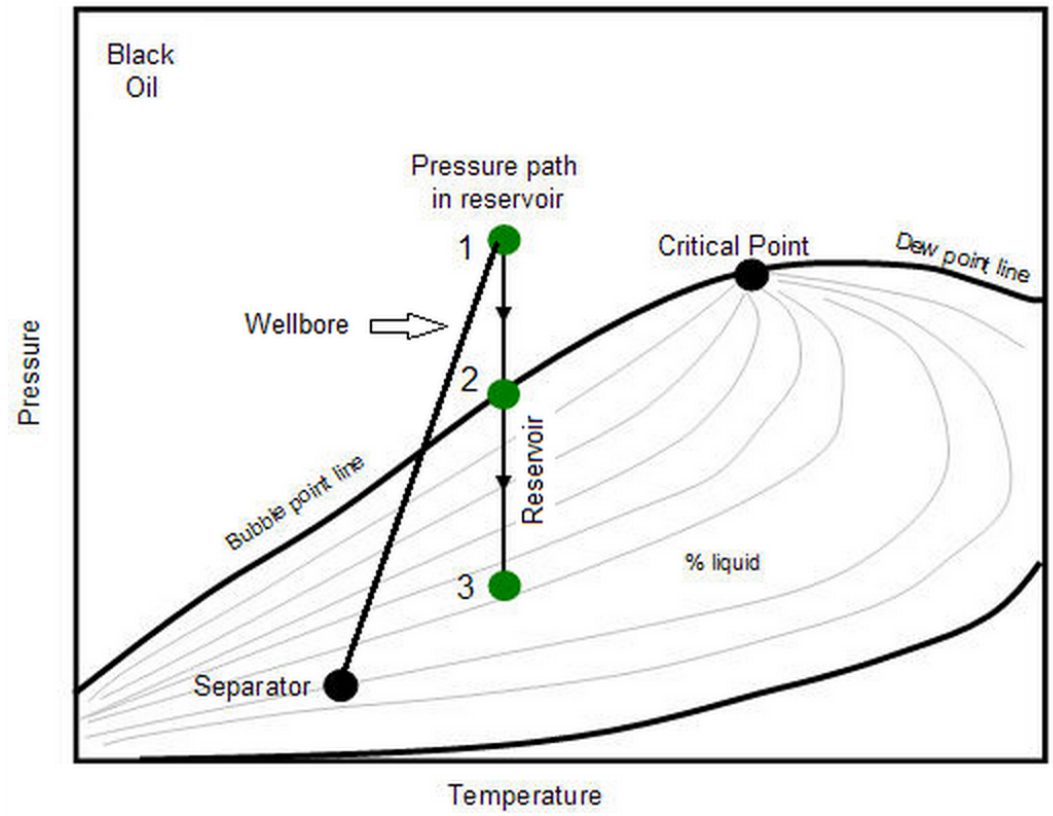
Black
Oil
Pressure path
in reservoir
1
Critical Point
Dew point line
Wellbore
2
Reservoir
Bubble point line
% liquid
3
Separator
Pressure
Temperature

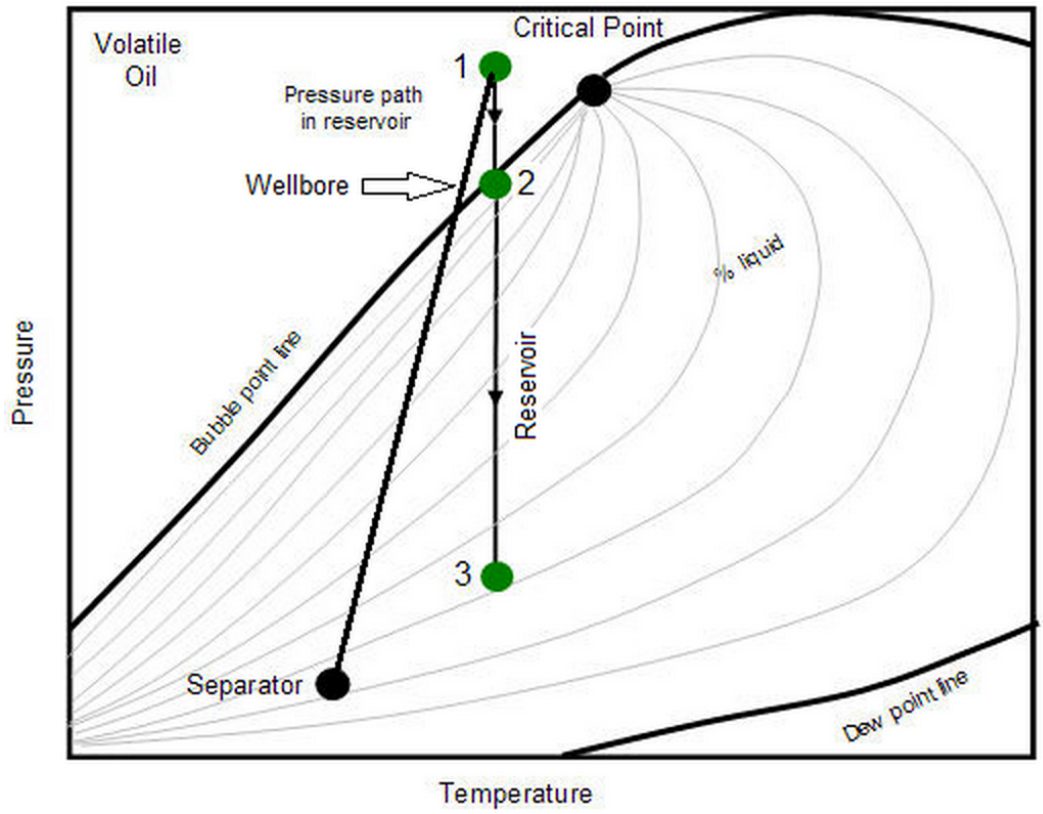
Volatile
Oil
Critical Point
1
Pressure path
in reservoir
Wellbore
2
% liquid
Bubble point line
Reservoir
3
Separator
Dew point line
Pressure
Temperature

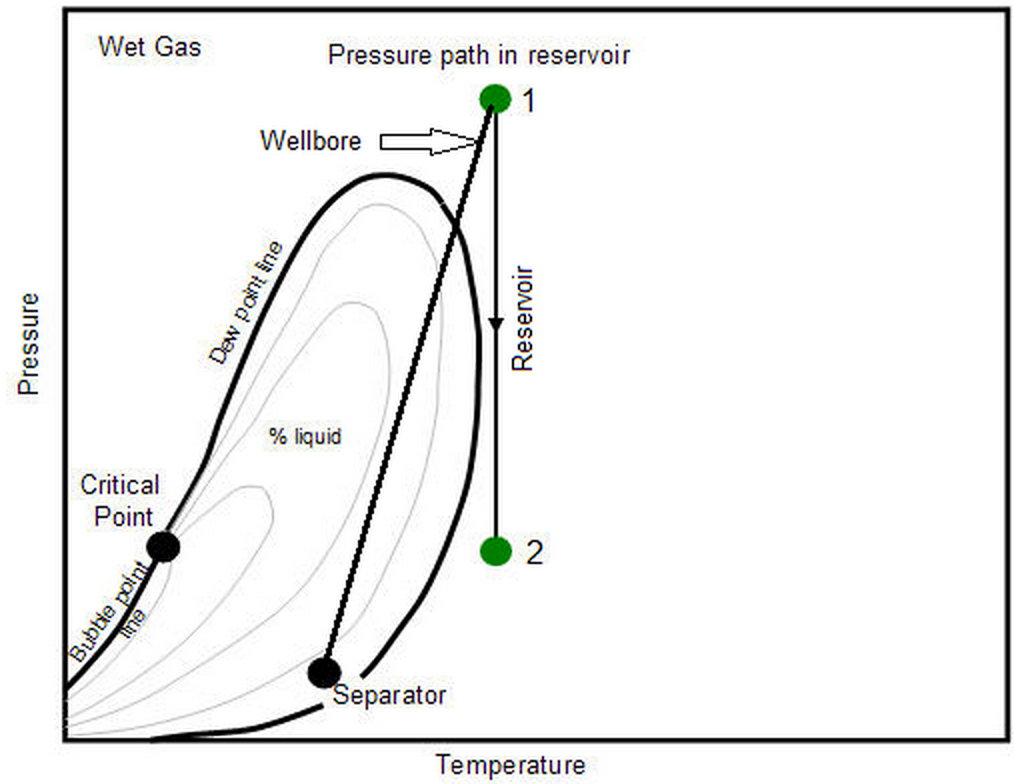
Wet Gas
Pressure path in reservoir
1
Wellbore
Dew point line
Reservoir
Pressure
% liquid
Critical Point
2
Bubble point line
Separator
Temperature

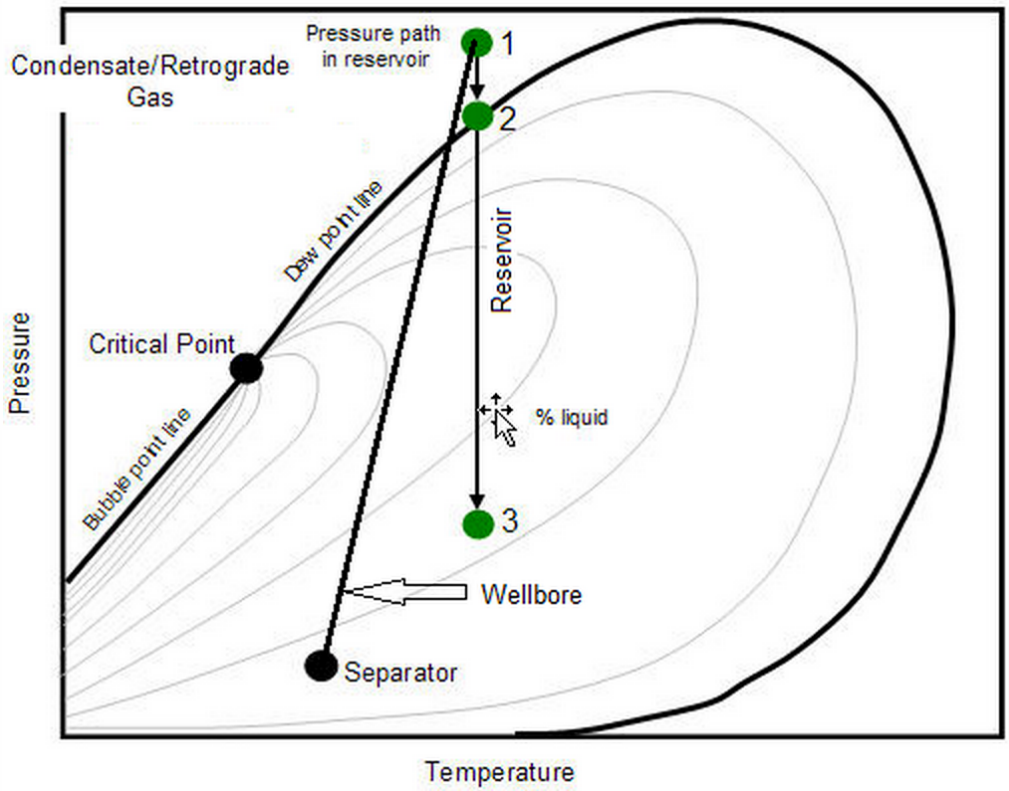
Pressure path in reservoir
1
Condensate/Retrograde Gas
2
Dew point line
Reservoir
Pressure
Critical Point
% liquid
Bubble point line
3
Wellbore
Separator
Temperature

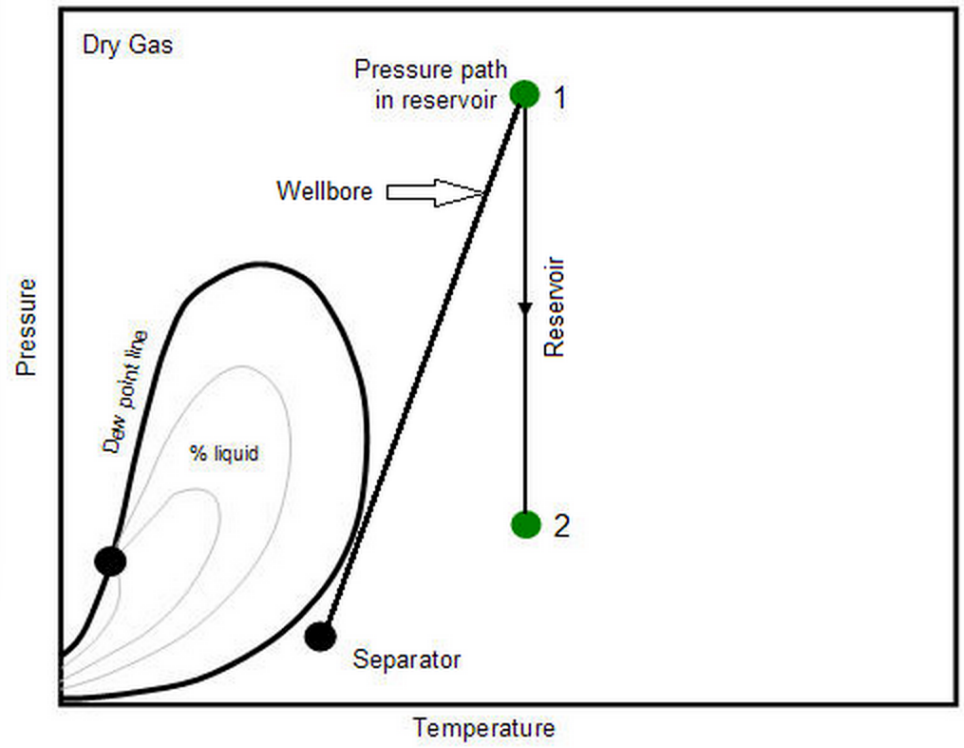

Figure 4.8— Illustrations of five main types of reservoir fluids (after IHS, 2014)

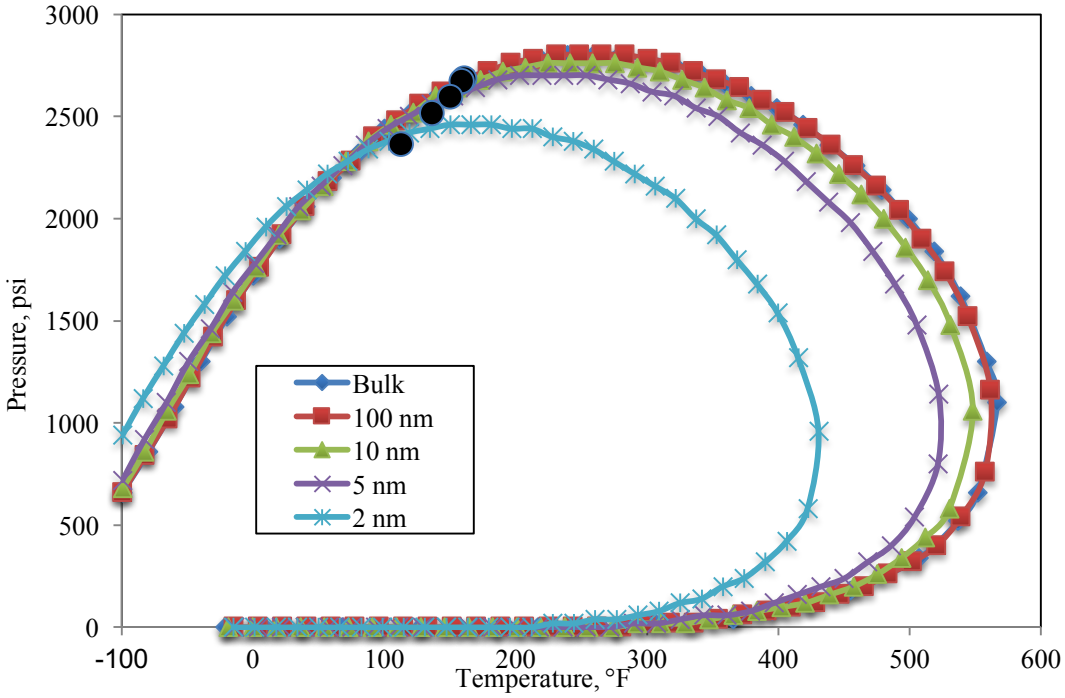

Figure 4.9— Two-phase envelopes of a C1/nC4/C10 mixture in different pore sizes

4.3 Fluid Distributions in Single Pore System

In Chapter 4.2 we discussed the confinement effect on fluid phase behavior. Such effect is considered to be an averaged effect for single pore system to reveal the overall fluid thermodynamic relations. However, the fluid-wall interactions are strongly dependent on the distance between the porous wall and fluid molecules, which makes the fluid nonuniformly distributed across the pore. Such nonuniformity is important to fluid storage mechanism as well as fluid transport modeling, and is not observed in the phase behavior studies in Chapter 4.2. In this section, we investigated the fluid distributions of a single pore system using the SLD-PR model. Both pure component fluid and mixture fluid were examined. Sensitivity analysis was performed to see the effects of pore size, temperature, pressure and fluid composition on fluid distributions.

4.3.1 Fluid Distributions of Single Component and Mixtures in Single Pore System

Consider pure methane in a slit-shaped pore with width of 2.4 nm under the condition of 185 °F and 2600 psi. **Figure 4.10** shows the methane local density profile along the pore as well as the bulk density calculated from the SLD-PR model. **Table 4.11** gives the molecular diameters, fluid-wall energy parameters, as well as fluid critical properties for methane, ethane, propane and n-butane that were adopted for the calculations. The Data was originally from Poling et al. (2001). Note that all the results in this chapter were calculated based on these data. From Figure 4.10 it is clear that the local density of methane is at its maximum near both walls with the value of 0.48 g/cm^3 and decreases as it goes further from the wall and reaches a minimum value of 0.12 g/cm^3 in the center portion of the pore. However, we can see that even the minimum value of the local density

is still higher than the bulk density of methane (0.10 g/cm^3), which does not take into account the fluid-wall interactions. This means in a pore with 2.4 nm widths filled with pure methane under 185 °F and 2600 psi, the whole pore is under the influence of the wall and there is no free gas presented inside the pore.

The fluid density distributions were extended from methane to heavier components. **Figure 4.11** shows the density profiles for methane, ethane, propane and n-butane under 176 °F and 3043 psi in a 5-nm wide slit pore. It is clear to see the density profiles for these four different fluids are distinct from each other. Heavier fluids have higher bulk densities and adsorbed layer densities than lighter fluids. On the other hand, the density difference for lighter fluids is greater than heavier fluids. Such density difference is the difference between the fluid densities at the position closest to the wall compare to the density in the center of the pore where it is at the lowest value. For example, for methane, such difference can be 0.27 g/cm^3, or over 200% in terms of percentage difference. Such difference is decreased to 0.26 g/cm^3 or 75% for ethane under the same conditions. And it is further decreased to 0.19 g/cm^3 or 38% for propane and 0.15 g/cm^3 or 25% for n-butane. This results shows that the effects of confinement are larger for lighter components, like methane, compare to heavier components such as n-butane.

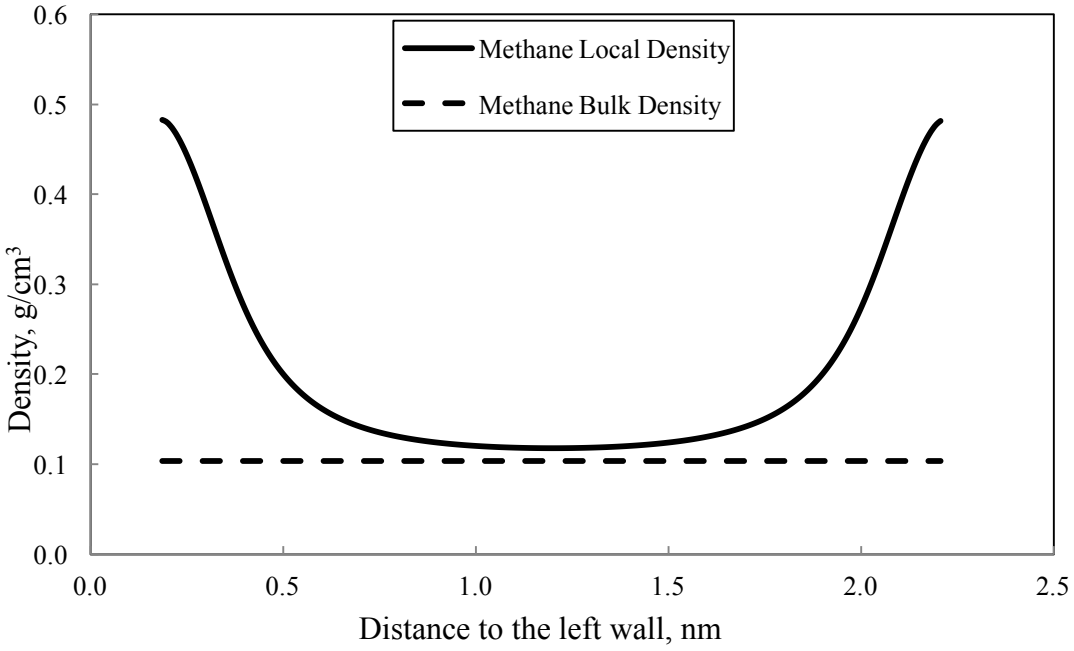

Figure 4.10— Methane local density profile along a 2.4-nm pore as well as the bulk density under 185 °F and 2600 psi calculated from the SLD-PR mode

Table 4.11—Physical Properties of Different Hydrocarbons

Component	Chemical Formula	Critical Temperature (°F)	Critical Pressure (psi)	Energy Parameter (°F)	Molecular Diameter (nm)	Acentric Factor
Methane	CH_4	-117.0	667.2	-192.2	0.3758	0.011
Ethane	C_2H_6	90.1	707.8	-71.4	0.4443	0.099
Propane	C_3H_8	206.0	616.4	-32.9	0.5118	0.153
n-Butane	n-C_4H_{10}	305.7	551.1	496.85	0.4687	0.199

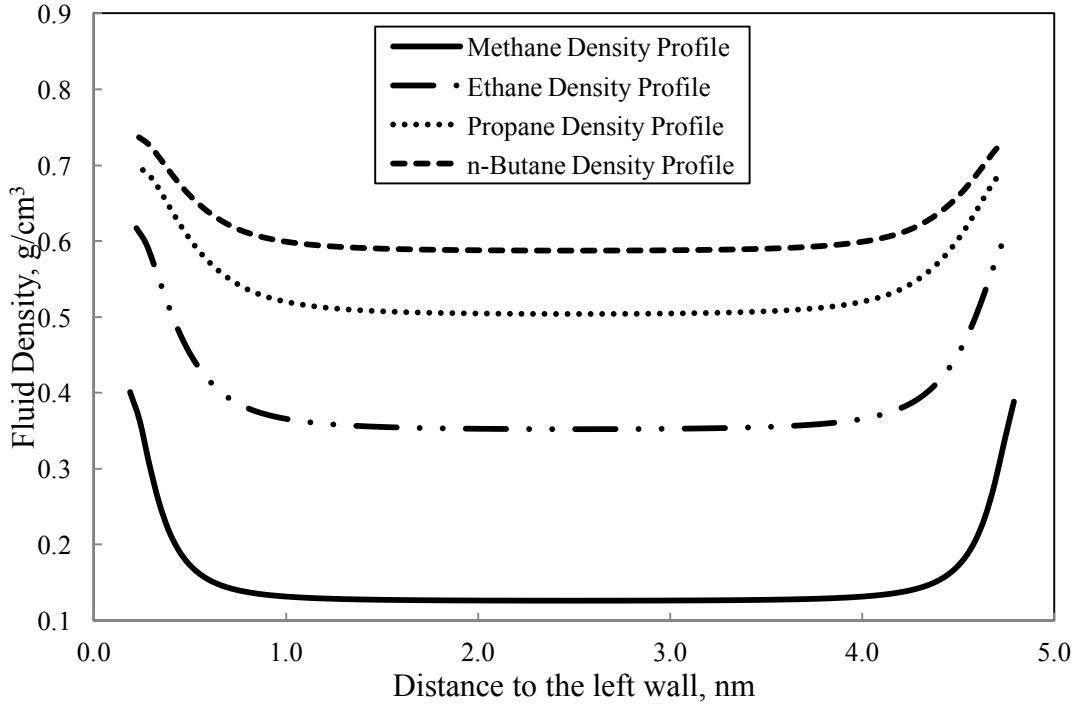

Figure 4.11— Density profiles for methane, ethane, propane and n-butane under 176 °F and 3043 psi in a 5-nm wide slit pore calculated from SLD-PR model

Multicomponent fluid mixtures can behave much different than single component fluids. As discussed previously, the fluid-wall interactions have different effects on different fluids. This can cause the fluid composition to vary with respect to the distance to the porous wall, which makes the scenario much more complicated. Consider a binary mixture that contains 80% methane and 20% n-butane in bulk at 170 °F and 3500 psi in a 20-nm wide pore, the mixture density profile is calculated using the SLD-PR model and is shown in **Figure 4.12**. Note that in Figure 4.13, the fluid density is shown in mol/cm^3. It is clear to see that unlike the single component density profiles, the mixture fluid density first increases when approaches to the wall and reaches to a maximum value before it hits the wall, then it starts to decrease when further closer to the wall. The two

humps of the mixture density profile are the results of fluid composition variance across the pore. **Figure 4.13** gives C1 and C4 composition distribution across the 20-nm pore. From the plot, it shows that the composition of C1 drops from 80% to almost 0% when it gets closer to the pore wall. On the other hand, the composition of C4 increases dramatically in the region near the pore wall. Thus, the mixture density is dominated by C4 when it is very close to the pore wall. The results show consistent conclusion that the pore wall favors heavier components much more than lighter components. In order to further investigate the relationships between the mixture and single component density distributions, we put the pure C1 and C4 density profiles along with the mixture density profile on the plot, as shown in **Figure 4.14**. It is clear to see that the mixture density profile tends to approach the pure C4 density profile when close to the wall. This demonstrates the reason why the mixture density profile will decline near the wall. We can also observe from Figure 4.15 that the adsorption of pure methane is significantly stronger compare to the mixture adsorption and pure C4 adsorption. This means that the adsorption ability of light component, such as C1, is stronger than heavier component, such as C4.

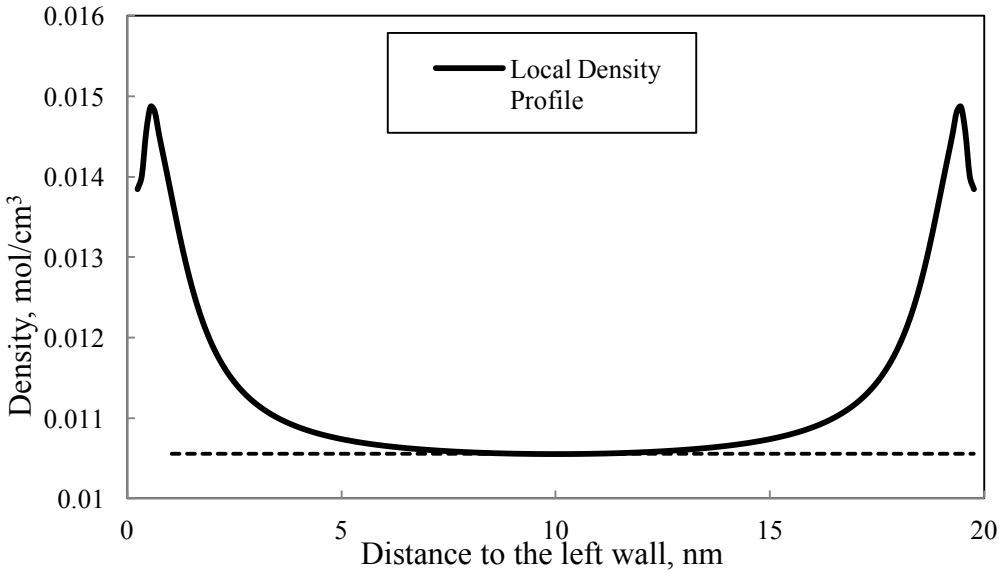

Figure 4.12— Density profile of an 80% C1/ 20% C4 mixture at 170 °F and 3500 psi in 20 nm pore calculated from SLD-PR model

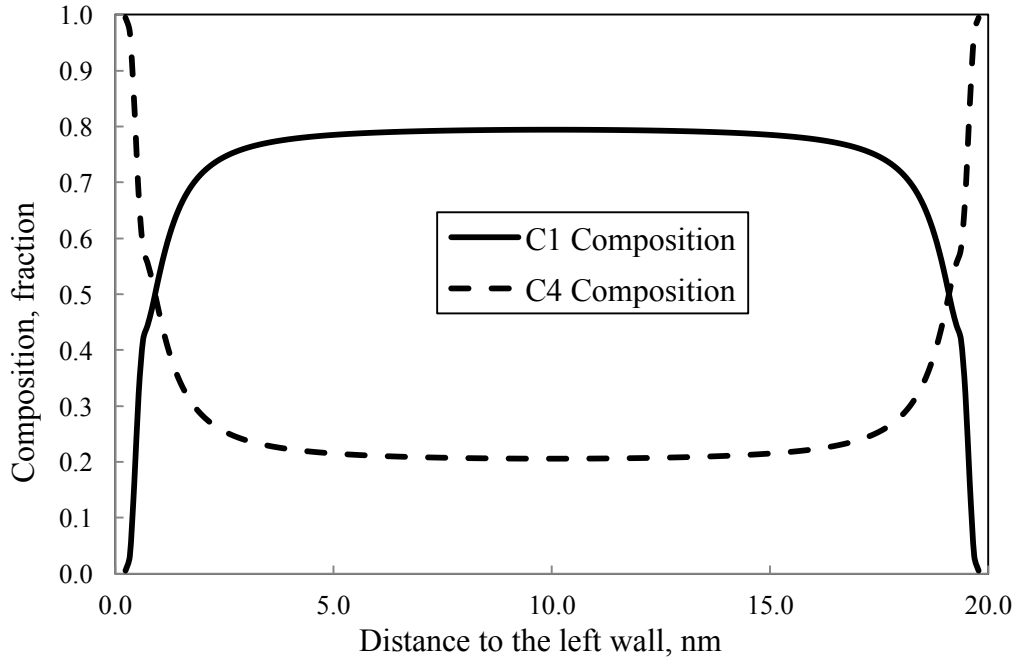

Figure 4.13—C1 and C4 composition distribution in the 20-nm pore at 170 °F and 3500 psi calculated from SLD-PR model

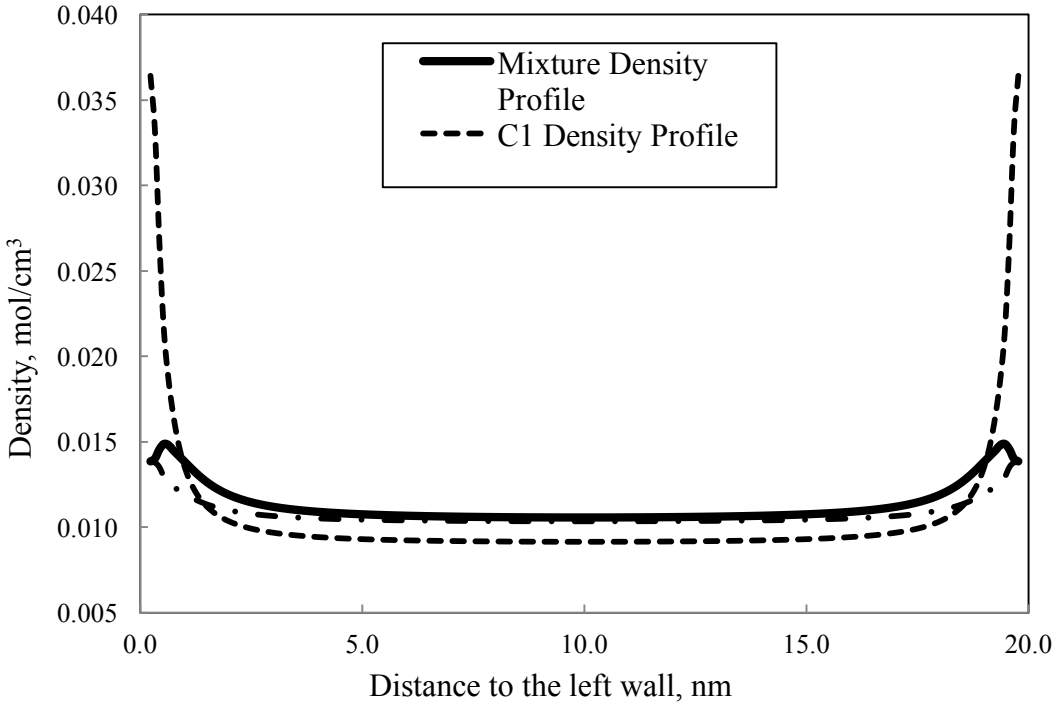

Figure 4.14— Density profiles of pure C1, pure C4 and 80% C1/ 20% C4 mixture in the 20-nm pore at 170 °F and 3500 psi calculated from SLD-PR model

4.3.2 Sensitivity Analysis

In the previous section, we discussed the density distributions of both single component and mixture fluids. The pore size, temperature, pressure and fluid composition were fixed during the study. In this section, we will investigate the influences of these parameters on the fluid density distributions.

Pore size is one of the most important factors that can influence fluid density distributions. Consider pure methane in a slit-shaped pore under the condition of 185 °F and 2600 psi. The pore size varies from 2 nm up to 10 nm. **Figure 4.15** shows methane density profiles in pores with width equal to 2, 4, 6, 8 and 10 nm. From the figure, it is clear that the local

density of methane is at its maximum near both walls with the value of around 0.38 g/cm^3 for all the pore sizes. The methane density decreases as it goes further from both walls and reaches a minimum value at the center of the pore. When the pore size is decreasing, the percentage of space where the methane is under strong wall influence is increasing based on the density profile shape. For pores with widths equal to 4, 6, 8 and 10 nm, the minimum methane densities at the center of the pores are equal to the methane bulk density, which is 0.11 g/cm^3. For the 2-nm pore, even the lowest methane density in the center is higher than the bulk density. This means in a pore with 2 nm in width, the whole pore is under the influence of the wall. As a result, the free gas not exist at any places within the 2-nm pore under the condition of 185 °F and 2600 psi.

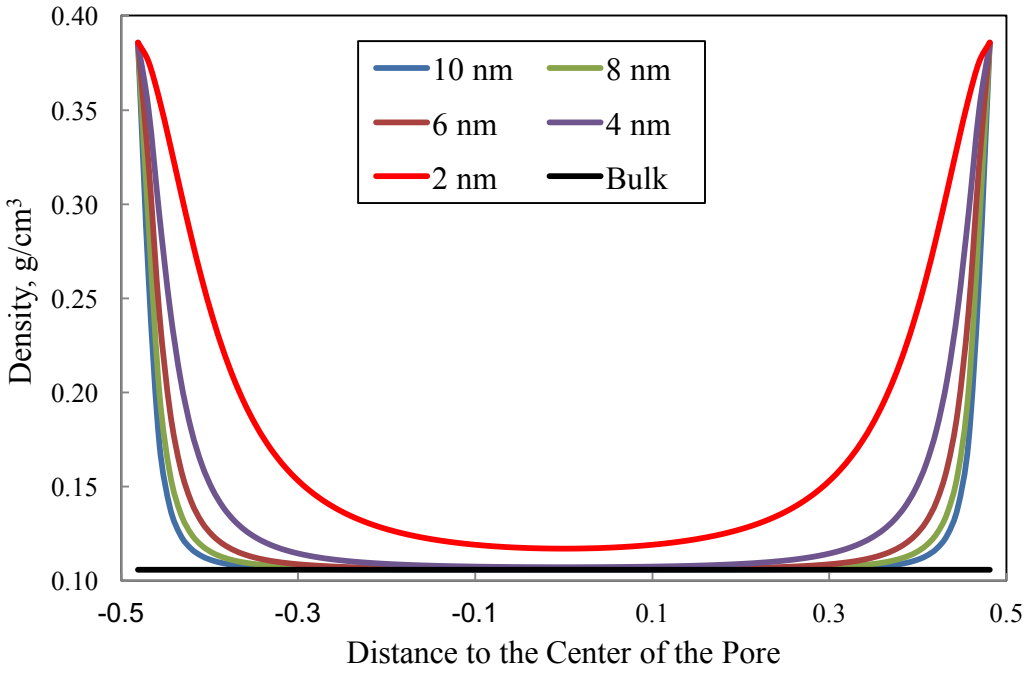

Figure 4.15— Density profiles of methane confined in pores with variety widths under 185 °F and 2600 psi. Pore sizes of 2, 4, 6, 8 and 10 nm were selected to show in the figure

Other than pore size, the pressure and temperature can also influence the fluid density distributions when confined in nanopores. **Figure 4.16** shows the density profiles of pure methane under variety of pressure conditions, ranging from 3000 to 7000 psi. The temperature and pore size are fixed to be 200 °F and 10 nm, respectively. From the figure, we can see that the density profiles are shifting up with increasing pressure. However, the rate of density increase in the center region is higher to the adsorbed region close to the walls. For example, when the pressure is changed from 3000 to 4000 psi, the methane density in the center region of the pore is increased by 0.035 g/cm^3. For the regions close to the wall, such change is 0.020 g/cm^3, which is much less than the density change in the bulk region. The results imply that the pressure has larger impact on the bulk methane density than the adsorbed methane density. This is because the adsorbed methane has already been much more compressed compare to the bulk methane due to the fluid-wall interactions and thus harder to be compressed. The increase in pressure, which is equivalent to further compressing the fluid, will have more impacts on less compressed fluids.

In order to investigate the effects of temperature on methane density distributions, four different temperatures are chosen at the constant pressure of 4000 psi in a 10-nm pore: 150, 200, 250 and 300 °F. Unlike the effects of pressure change on methane densities, as shown in **Figure 4.17**, we see that the methane density profile is shifting down at higher temperature, means that the increase in temperature can cause the decrease in methane density in both bulk region and adsorbed region inside the pore. The results are consistent with fluid PVT relations, where an increase in temperature will cause the decrease in fluid density. Furthermore, the effects of temperature change on methane density in bulk region

and adsorbed region are similar. For example, when the temperature changes from 150 to 200 °F, the density decrease in the bulk region is 0.018 g/cm^3, while the decrease in the adsorbed region is 0.020 g/cm^3. This is because the increase in temperature, which is equivalent to thermal expansion, is independent on fluid compressibility ability.

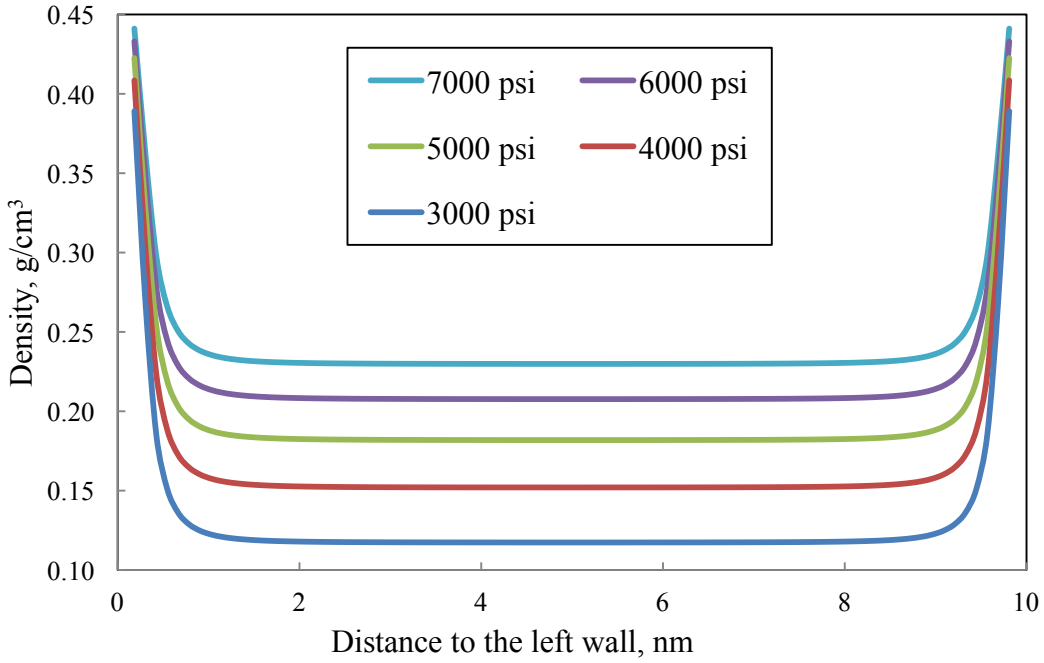

Figure 4.16— Methane density profiles confined in pores under variety pressures. The temperature and pore size are fixed to be 200 °F and 10 nm, respectively

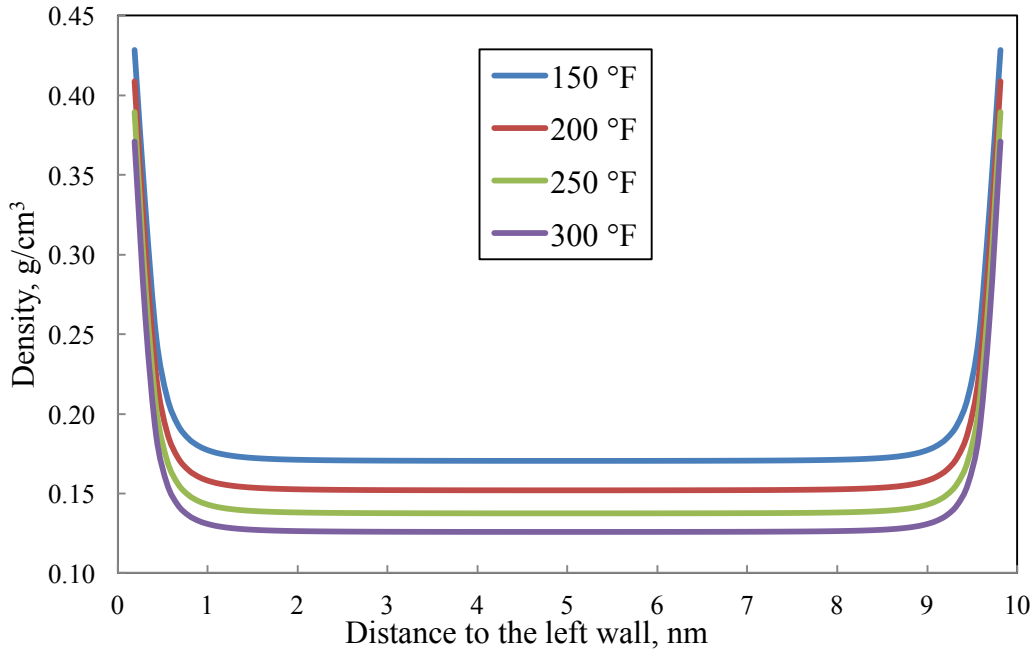

Figure 4.17— Methane density profiles confined in pores under variety temperatures. The pressure and pore size are fixed to be 4000 psi and 10 nm, respectively

Last, we evaluated the effects of changing composition on the mixture fluid density profiles. Consider a binary mixture contains methane and n-butane in a 20-nm wide pore at 3500 psi and 170 °F, the density profiles of the mixture fluid are shown in **Figure 4.18**. Note that the composition of methane in the mixture is varied from 50% to 80%. It is clear to see from **Figure 4.18** that the density profiles representing different methane compositions separate well in the center region of the pore, but become closer when approaching the wall and finally become identical when it reaches the closest position to the wall. This can be explained by the methane composition distributions, showing in **Figure 4.18**. In the center region of the pore, the methane compositions remain constant and equal to the original methane compositions in the mixtures; the fluid mixture densities

are also equal to the bulk densities. The mixture that contains heavier component, in this case n-butane, will have larger density. However, when the fluids become closer and closer to the wall, the methane compositions drop dramatically and eventually become almost zero for all the four cases, as shown in **Figure 4.19**. When the methane composition of the mixture becomes negligible, the fluid behavior is dominated by n-butane and therefore the four different mixtures become identical near the wall.

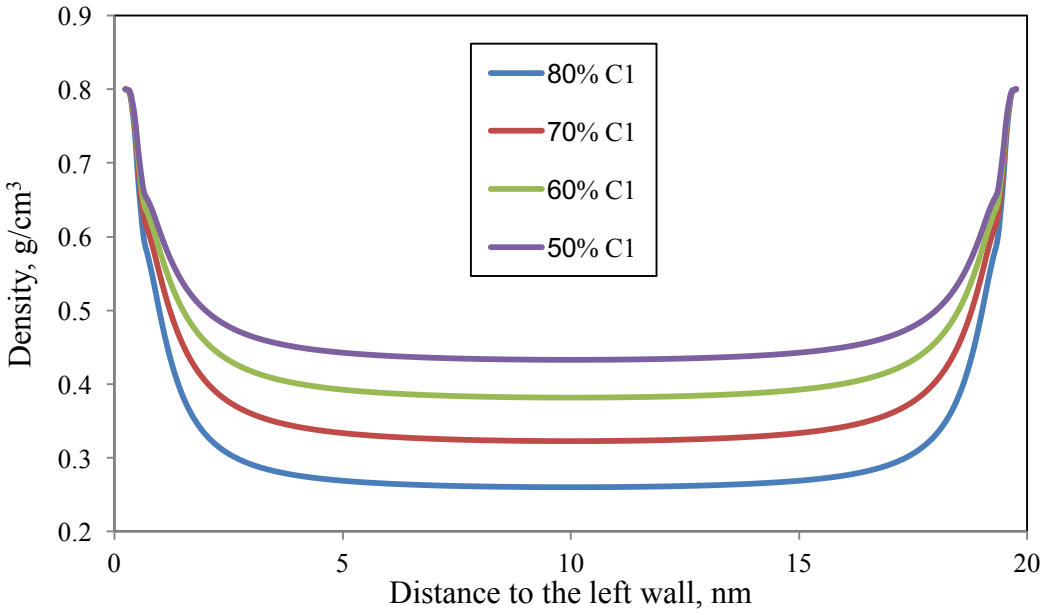

Figure 4.18— Density profiles of binary mixtures containing methane and n-butane with variety composition combinations in a 20-nm pore at 3500 psi and 170 °F

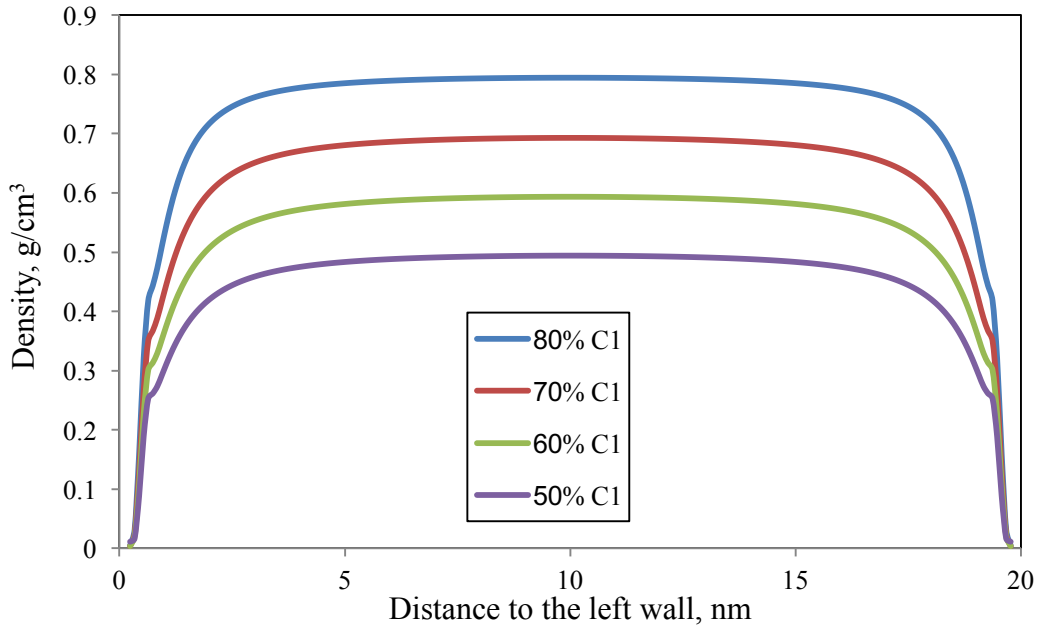

Figure 4.19— Methane composition distributions of four different fluid mixtures in a 20-nm pore at 3500 psi and 170 °F

4.4 Adsorption Isotherms of Pure and Mixture Hydrocarbons in Nanopores

The investigations of adsorption isotherms of pure and mixture gases in nanoporous materials have been carried out for many decades from both experimental studies (Dreibach et al., 1999; Heuchel et al., 1999; Yun et al., 2002; Gasem et al., 2003; Harlick and Tezel, 2003; Wu et al., 2005) and simulation methods (Maddox et al., 1996; Du et al., 1998; Heuchel et al., 1999; Yun et al., 2002; Gasem et al., 2003; Jiang and Sandler, 2004; Yang and Zhong, 2006; Bae et al., 2008). Until recently, the adsorption of pure methane in shale rocks has been studied (Nuttall et al., 2005; Beaton et al., 2010; Weniger et al., 2010; Zhang et al., 2012; Yuan et al., 2014). In this section, we chose some adsorption experimental data and molecular simulations data from the literature to compare with the results from the SLD-PR model. The adsorption isotherm at a specific temperature and pressure is calculated by subtracting the adsorbed density by bulk density. The adsorbed density is obtained by integrating the density profile calculated from the SLD-PR model at a specific pore size using the trapezoidal rule.

Yun et al. (2002) reported adsorption measurements of methane, ethane and their binary mixtures on MCM-41 materials with temperature from 263 to 374 K and pressure from 0.01 to 3.3 MPa. The MCM-41 materials are molecular sieves with cylindrical pore channels with diameters range from 1.5 to 10 nm and the mean pore size is 4.1 nm. **Figure 4.20** shows the adsorption isotherms of pure methane and ethane at 373.15 K. The energy parameters of methane and ethane used in the model were from Table 1. The wall energy parameter was adjusted to be 11 K to give the best fit. **Figure 4.21** gives the adsorption isotherms of each component in the binary mixture containing 28.7 mole% methane and

71.3 mole% ethane at 264.75 K. The results of the mixture adsorption isotherms showed that the adsorbed amount of methane could be almost negligible. This indicates that ethane is a stronger adsorbate, compare to methane.

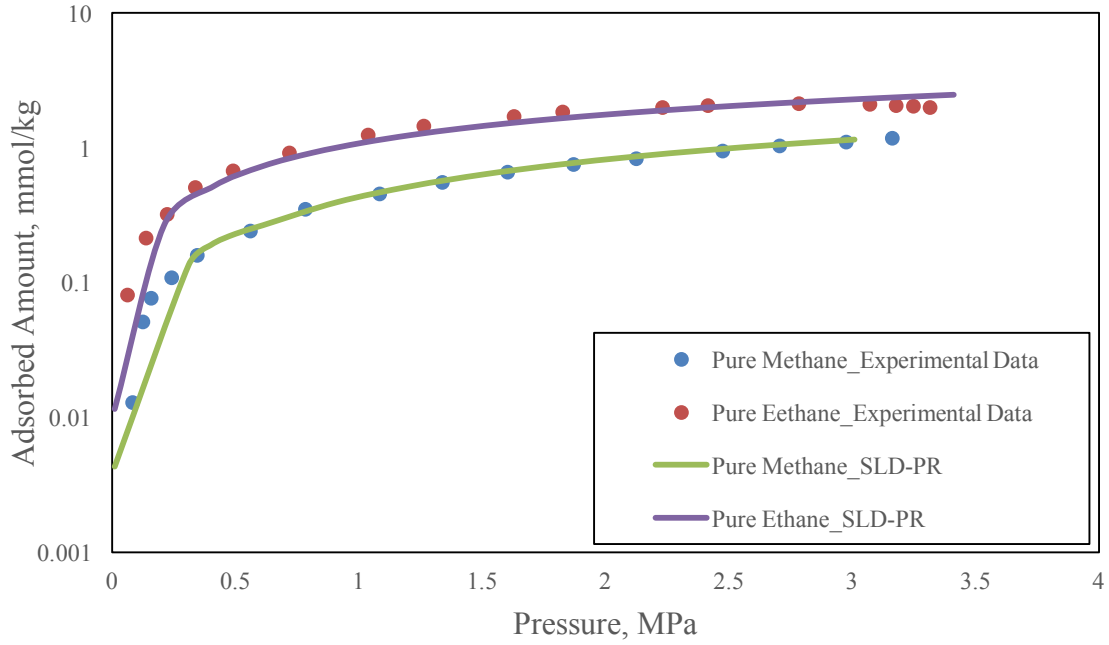

Figure 4.20— Adsorption isotherms of pure methane and ethane at 373.15 K on MCM-41 materials

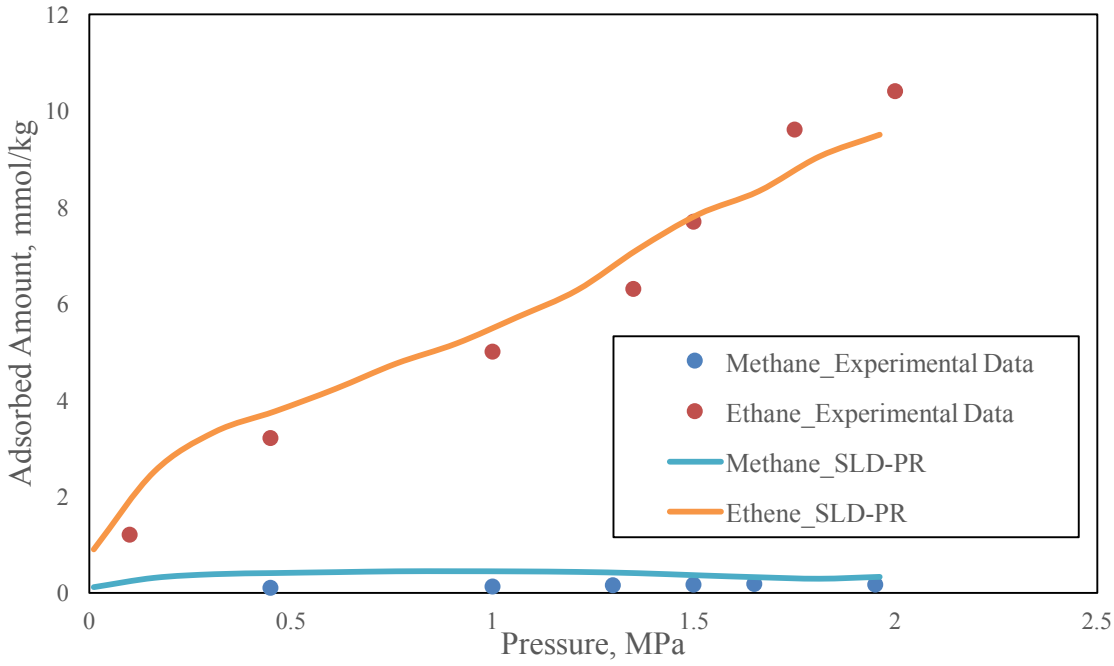

Figure 4.21— Adsorption isotherms of each component in the binary mixture containing 28.7% methane and 71.3% ethane at 264.75 K on MCM-41 materials

Du et al. (1998) performed molecular simulations to study the adsorption of pure short n-alkanes and the binary mixtures of methane/ethane in silicalite with mean pore size reported as 0.55 nm. The compositions of methane in the adsorbed phase of methane/ethane were simulated and plotted against bulk methane composition at two different pressures of 345 and 655 kPa. They compared the results with experimental data from Abdui-Rehman et al. (1990) and found good match. Here we used the SLD-PR model to generate the relationships between the methane composition in bulk and in adsorbed phase, as shown in **Figure 4.22**. The Lennar-Jones parameters of methane, ethane and the silicalite wall used in the SLD-PR model were directly adopted from Du et al. (1998). The mean pore size was adjusted to be 1.6 nm to give the best. From the figure, it is clearly to see that the SLD-PR model was able to predict the results well with

data from both molecular simulation data of Du et al. (1998) and experimental data of Abdui-Rehman et al. (1990). It was found that the methane composition diagram was not sensitive to pressures. More importantly, it is clear to see that the composition curve is concave-downward, which means the methane composition in confined space (x-axis) is smaller than the bulk methane composition (y-axis). For example, the methane composition in confined silicalite is 7% when the bulk methane composition is 50% at 345 kPa. As the methane bulk composition increases, the confined methane composition also increases, but the methane bulk composition is always greater than the confined methane composition. Another example from Figure (17) is that when the bulk methane composition is 89% and the confined methane composition is 33% at 345 kPa. This means that the other adsorbate, ethane, is preferentially adsorbed in silicalite compare to methane.

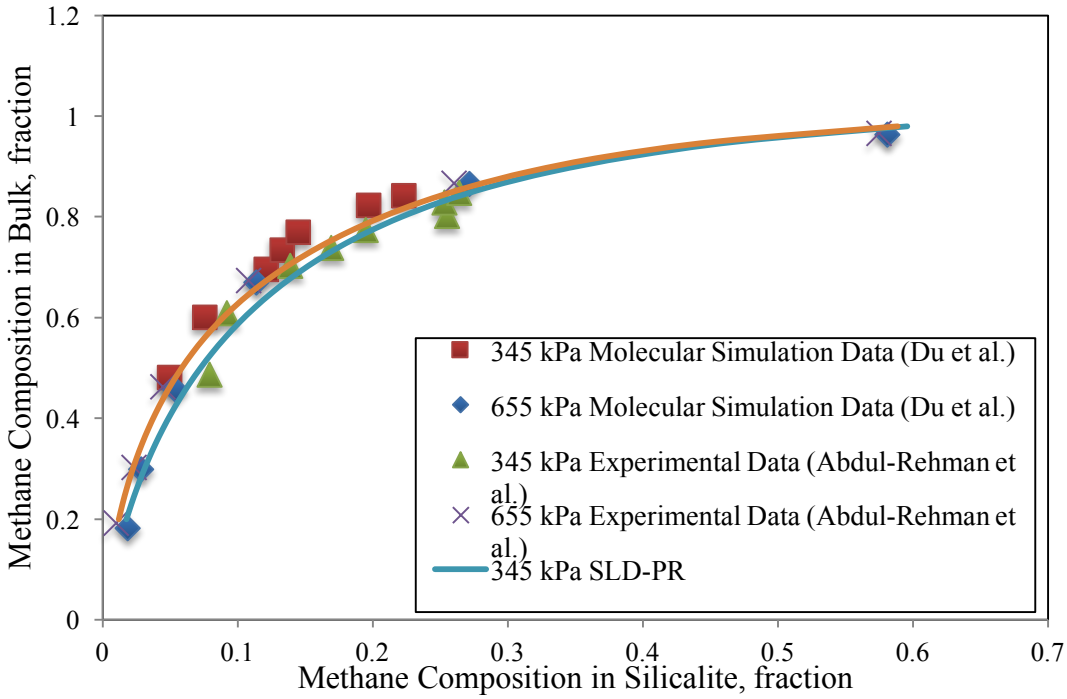

Figure 4.22— Methane composition diagram of a methane/ethane mixture at pressure of 345 and 655 kPa

Zhang et al. (2012) performed a series of methane adsorption experiments on organic rich shales and their isolated kerogens under different temperature conditions with pressure up to 15 MPa. Shale samples with different organic matter types and thermal maturities were used. Results showed that the maximum adsorption capacity of methane in type I kerogen is lower than types II and III. They also found that the methane adsorption capacity is higher in shale samples with higher thermal maturity. We used the SLD-PR model to simulate methane adsorption in kerogen concentrates of Green River shale (type I) and Woodford shale (type II) at 323.15 K, as shown in **Figure 4.23**. The mean pore size and pore volume were not given from Zhang et al. (2012). To fit the experimental data, the mean pore size of 15 nm for both shales and the pore volumes of

0.29 and 0.46 mL/g for Green River shale and Woodford shale, respectively were used in the SLD-PR model. There is an excellent agreement between the SLD-PR model and the reported experimental data.

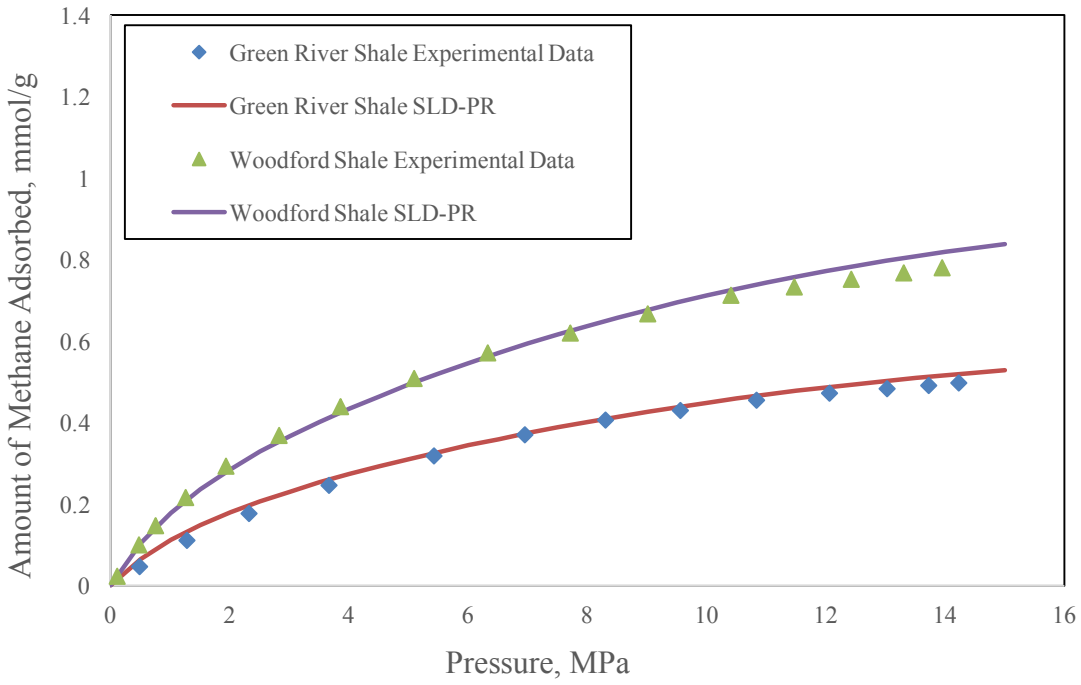

Figure 4.23— Methane adsorption in Green River shale and Woodford shale at 323.15 K

Chapter 5: New Gas-In-Place Model for Shale Gas Condensate plays

5.1 Background and Previous Work

Shale formations are formed by fine-grained, clastic sedimentary rock composed of muds that consist of two different components, organic matters and inorganic matters. The organic matters are mixtures of organic materials that are composed of the remains of once-living organisms such as plants and animals and their wasted products, while the inorganic matters contain a mix of flakes of clay minerals and small fragments of quartz, pyrite and other minerals (EIA, 2017). Hydrocarbons can be found in both organic content and inorganic matrix. The estimation of the total initial gas-in-place is extremely important not only to gas reserve disclosures, but also for production analysis and forecast. Volumetric method for gas-in-place estimations is quite often used for newly developed fields with key reservoir parameters obtained, such as total porosity (including clay-bound water), water saturation, bulk rock density, fluid composition and so on (Luffel and Guidry, 1992 and Mavor and Nelson, 1997). These parameters can be measured with well logs, fluid sample analysis and core sample analysis. Such parameters allow us to predict the total volume associated with hydrocarbons, which leads to the estimation of gas-in-place.

The petrophysical characterizations in shales have been well investigated recently. **Figure 5.1** provides a typical volumetric petrophysical model for shale formations. It is known that the gas is stored in two different forms in kerogen (organic content) in organic-rich shale formations, free gas and adsorbed gas. **Figure 5.2** illustrates the

distributions of fluids in the total pore volume. The total porosity is divided into two categories, with one associated with organic porosity, named kerogen porosity and the other one associated with the porosity within the inorganic matrix. The pore volume in the inorganic matrix is occupied by free gas and formation water, while the pore volume of the organic content is filled with adsorbed gas and free gas. In this storage model, the adsorbed gas in inorganic matrix and the water in organic materials are assumed to be negligible. The characteristics and properties of the adsorbed phase, such as thickness and density are extremely important for shale gas-in-place calculations. These parameters are direct inputs to the volumetric method. Inaccurate predictions of the adsorbed phase properties can result in either under- or over-estimation of the true total hydrocarbon capacity in the shale formations.

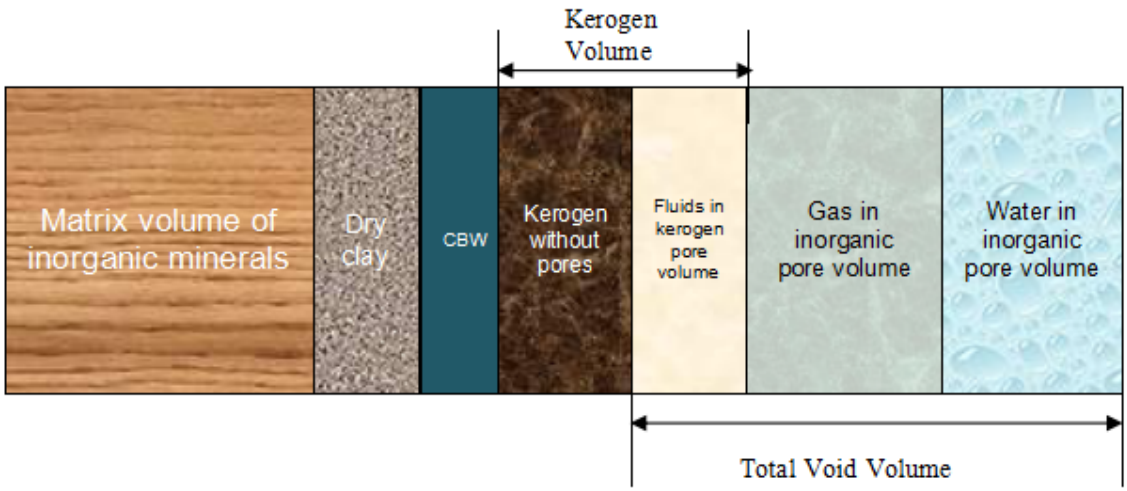

Figure 5.1— Volumetric petrophysical model

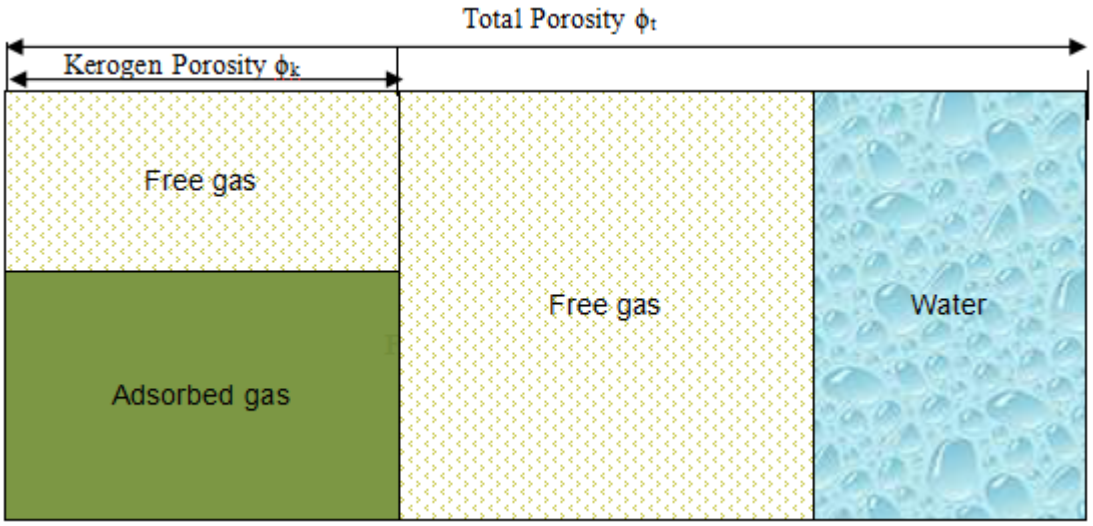

Figure 5.2— Fluid storage model

Several literatures regarding the methodologies of shale gas-in-place calculations considering the adsorbed phase are available. Ambrose et al. (2010) considered new pore scale into gas-in-place calculation for dry gas shale. They took into account the volume occupied by the adsorbed phase and computed the density of the adsorbed phase using molecular dynamic techniques. Their results showed that the results from molecular simulations on adsorbed phase density were similar compare to the predictions obtained from Langmuir single-layer adsorption model for pure methane at reservoir conditions. Then Langmuir adsorption model was then used to compute the amount of adsorbed gas. This method may be valid for dry gas shale (pure methane), however, for gas-condensate shale, where considerable amount of heavier components other than methane can exist, such method may no longer be valid due to multi-layer adsorption (Li et al., 2014; Ma and Jamili, 2014; Ma and Jamili, 2016) and heterogeneity in terms of fluid composition (Didar and Akkutlu 2013; Ma and Jamili, 2014). Their later publication (Hartman et al., 2011) considered the effects of multi-component on gas adsorption. Extended-Langmuir

(EL) model and Ideal Adsorbed Solution (IAS) theory were used to characterize the adsorbed phase. Although the results showed inhomogeneous of the fluid composition between free gas phase and adsorbed gas phase, they did not provide a clear way to compute adsorbed phase density and the effects of multi-layer adsorption was not considered. Li et al. (2014) focused on the gas-in-place calculations of gas condensate shale with the presence of capillary condensation. The adsorbed phase thickness was computed based on Shapiro's model (Shapiro and Stenby, 1996), but the adsorbed phase density was assumed to be twice as the free gas density. Moreover, Shapiro's model may not be valid at pressure above the dew point pressure where there is no capillary condensation.

The adsorbed phase density and thickness are the key parameters for shale gas-in-place calculation. As we can see so far, no literatures can provide clear and accurate predictions of both of the parameters. However, the Simplified Local Density (SLD) theory discussed in the previous chapters has the capability to calculate the density profiles of the fluids across the pore. From the density profile, one can easily define the adsorbed phase thickness and determine adsorbed density as well as fluid composition based on average values. Therefore, a new GIP volumetric method is developed based on the SLD theory. In this chapter, we will discuss the mathematical theory of the model and the applications to predict the total gas-in-place for a field example of Eagle Ford shale.

5.2 The New Volumetric Method for Shale Gas Content Calculations

A new volumetric method to calculate the gas-in-place was developed based on the volumetric petrophysical model and the fluid storage model shown in Figure 5.1 and Figure 5.2. The total gas storage, G_{st}, describing the amount gas in standard cubic feet at surface condition per ton rock is used as industrial standard. Based on our fluid storage model, the total gas storage G_{st} is considered to have the following components:

$$G_{st} = G_{ads} + G_{f,org} + G_{f,inorg} \quad \text{.....(5.1)}$$

Where G_{ads} represents the amount of adsorbed gas, $G_{f,org}$ and $G_{f,inorg}$ account for the free gas in organic pores and inorganic matrix, respectively. Here we assume that the gas dissolved in formation water is negligible and there is no hydrocarbon liquid at initial reservoir conditions (initial reservoir pressure far above the dew point pressure). Each of the three terms on the right side of Equation 5.1 can be further expressed in terms of volume occupied and the total bulk mass of rock:

$$G_{f,inorg} = \frac{V_{f,inorg,surf}}{M_b} \quad \text{.....(5.2)}$$

$$G_{f,org} = \frac{V_{f,org,surf}}{M_b} \quad \text{.....(5.3)}$$

$$G_{ads} = \frac{V_{ads,surf}}{M_b} \quad \text{.....(5.4)}$$

Where $V_{ads,surf}$, $V_{f,org,surf}$, $V_{f,inorg,surf}$ represent the volume occupied by adsorbed gas, free gas in kerogen, free gas in inorganic matrix at surface condition, respectively. M_b is the total bulk mass of rock in ton.

As we can see, in order to calculate the amount of adsorbed gas and free gas in both organic and inorganic materials, the volume occupied by each type of gas needs to be known a priori. By known the total porosity and kerogen porosity from petrophysical measurements, it is easy to separate the void volume into inorganic void volume and organic void volume. The volume occupied by free gas in inorganic matrix is associated with inorganic void volume. Equation 5.2 can be further expressed by known petrophysical parameters:

$$G_{f,inorg} = 8.7355 \times 10^5 \frac{[\phi_t(1-S_w)-\phi_k]\rho_{f,res} Z_f}{\overline{M}_f \rho_b} \quad \text{.....(5.5)}$$

Where ϕ_t and ϕ_k are the total porosity and kerogen porosity, respectively. S_w is water saturation, $\rho_{f,res}$ is the free gas density at reservoir condition, Z_f is the compressibility factor of free gas at surface condition, $\overline{M}_f$ is the apparent molar density of free gas and ρ_b is the bulk rock density. The compressibility factor Z_f and the fluid density $\rho_{f,res}$ can be calculated using an equation of state. Peng-Robinson equation of state developed by Peng and Robinson (1976) was used here. Similarly to $G_{f,inorg}$, the amount of gas in the organic content G_{ads} and $G_{f,org}$ can be computed as the following:

$$G_{f,org} = 8.7355 \times 10^5 \frac{[V_b\phi_k - V_{ads}]\rho_{f,res} Z_f}{\overline{M}_f \rho_b V_b} \quad \text{.....(5.6)}$$

$$G_{ads} = 8.7355 \times 10^5 \frac{V_{ads}\rho_{ads,res} Z_{ads}}{\sum_i^{n_c}(y_i MW_i)\rho_b V_b} \quad \text{.....(5.7)}$$

The derivations of Equations 5.5-5.7 from Equations 5.2-5.4 are illustrated in **Appendix B**. For the void volume in organic content, however, there is no direct petrophysical measurement that can distinguish the volume occupied by adsorbed gas and free gas. In

order to calculate the amount of gas G_{ads} and $G_{f,org}$, the characteristics of the adsorbed phase, such as adsorption film thickness, adsorbed phase density and fluid composition need to be computed first. These are calculated by using the SLD theory.

5.3 Adsorption Film Thickness, Adsorbed Density and Fluid Composition from SLD-PR Model

The density profile calculated from the SLD-PR model is a continuous profile. A density profile of 80% methane (C1) and 20% n-butane (C4) at 170 °F and 3500 psi in 20 nm pore is shown in **Figure 5.3** as an example of how the continuous density profile looks like. As we can see in Figure 5.3, there is no clear transition between the bulk phase and the adsorbed phase. In order to quantify the amounts of adsorbed gas and free gas, a cutoff point is used to separate the adsorbed phase and bulk phase. Here, the cutoff points, shown as the red dots in Figure 5.3, are defined as the positions where the local densities are just 1.15 times higher than the bulk density. Any position inside the pore that has a higher density than the cutoff density (>1.15*ρ) is classified as the adsorbed region. Another observation from Figure 5.3 is that the density first increases when approaches to the wall and reaches to a maximum value, after which the density starts to decrease when further closer to the wall. The result is different from what to be expected, which the fluid density should always increase when getting closer to the pore wall since the fluid-wall interactions becomes stronger for pure component. However, when the system has more than one component, the density profile can be very different because the fluid-wall interactions between the wall and different fluids are different. This can be further

explained by fluid composition distributions, as shown in **Figure 5.4**. Results show that the pore wall favors heavier components much more than lighter components. In Figure 5.4, the composition of C1 drops from 80% to almost 0% when it gets closer to the pore wall. On the other hand, the composition of C4 increases dramatically in the region near the pore wall. Therefore, the mixture density is dominated by C4, rather than the mixture itself within the region close to the pore wall. **Figure 5.5** shows the density profile of pure C1, pure C4 and the 80%/20% mixture in the same figure under the same temperature and pressure conditions. It is clear to see that the mixture density profile tends to approach the pure C4 density profile when close to the wall. This demonstrates the reason why the mixture density profile will decline near the wall. We can also observe from Figure 5.5 that the adsorption of pure methane is significantly stronger compare to the mixture adsorption and pure C4 adsorption. This means that the adsorption ability of light component, such as C1, is stronger than heavier component, such as C4. This is because methane molecules are much smaller than butane molecules, thus the pore wall is able to hold much more C1 than C4.

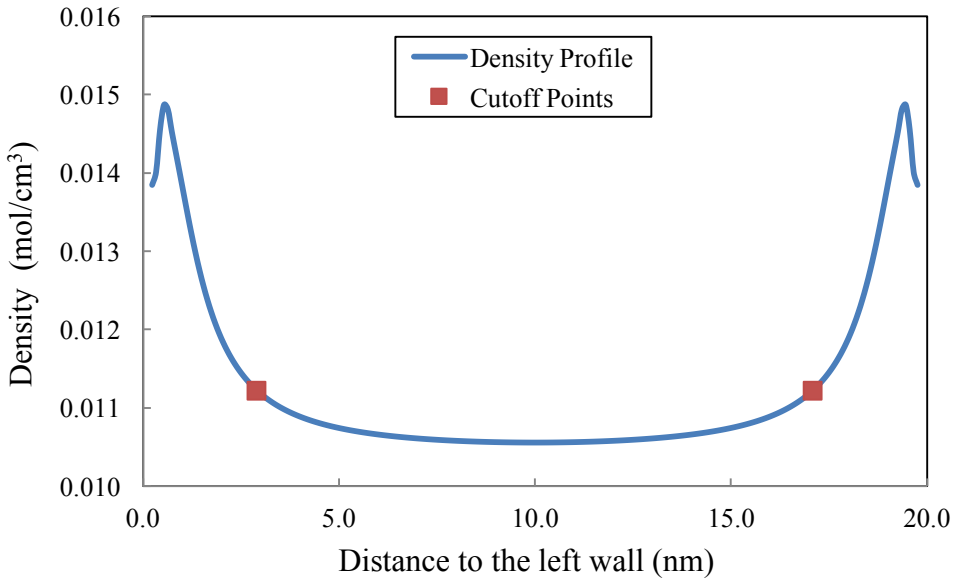

Figure 5.3—Density profile of a 80% C1/ 20% C4 mixture at 170 °F and 3500 psi in 20 nm pore calculated from multicomponent SLD-PR model. The red dots are the cutoff points which distinguish the free phase and the adsorbed phase.

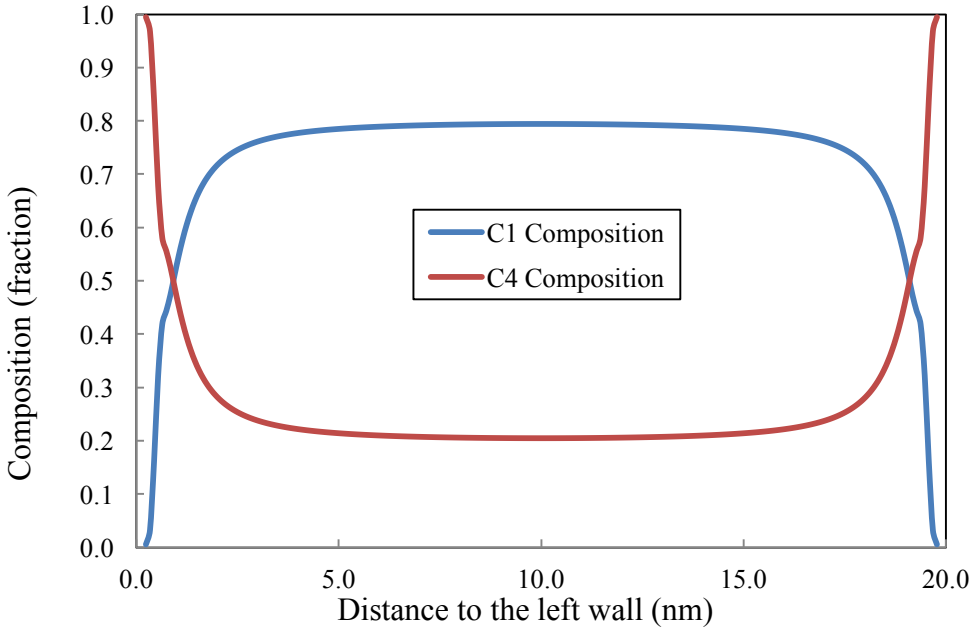

Figure 5.4—C1 and C4 composition distribution in the 20-nm pore at 170 °F and 3500 psi calculated from multicomponent SLD-PR model.

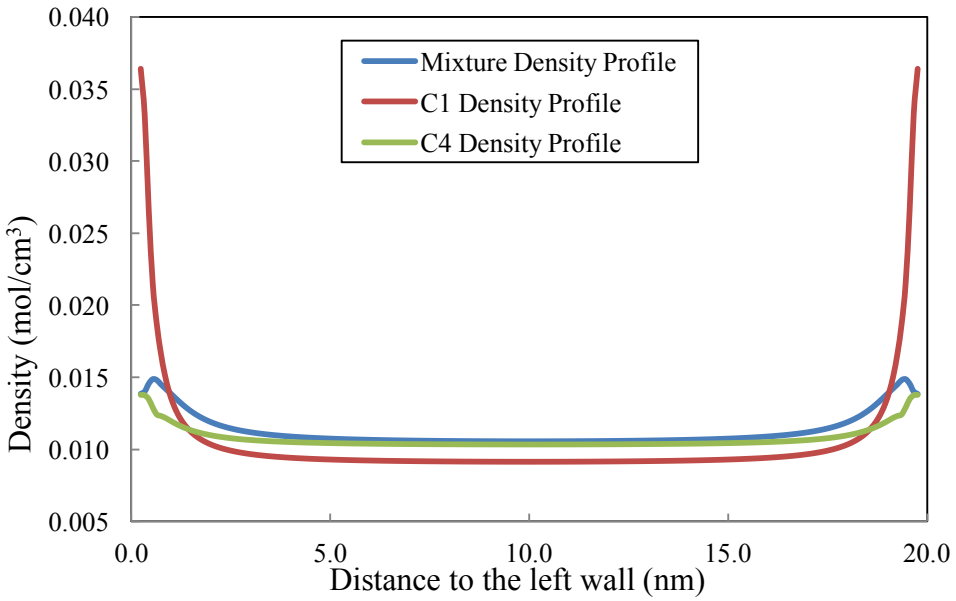

Figure 5.5— Density profiles for pure C1, pure C4 and 80% C1/ 20% C4 mixture in the 20-nm pore at 170 °F and 3500 psi calculated from multicomponent SLD-PR model.

Once the adsorbed region has been identified, the adsorption film thickness is equal to the distance from the pore wall to the cutoff point. Meanwhile, the continuous density can be converted to the equivalent averaged density profiles for both bulk phase and adsorbed phase, based on the cutoff points defined earlier. All the excess amount of gas with respect to the bulk state goes into the pre-defined adsorbed phase, leaving the bulk phase with the same and uniform density and fluid composition as the bulk state. The fluid density and composition of the adsorbed phase are averaged for convenience. So there will only have one set of values for the fluid density and fluid composition of the adsorbed phase in a single pore (see **Figure 5.6)**. **Figure 5.7** shows the averaged density profiles in different pore sizes for the same fluids at the same temperature and pressure conditions as that in Figure 5.3. As we can see, when the pore size gets smaller and

smaller, the region occupied by free gas phase is decreasing, but the adsorption thickness and adsorbed density remain the same. When the pore size is further decreased, the adsorption film on the opposite pore walls will merge, leaving no bulk phase in the center of the pore. Upon this point, the pore is all filled with adsorbed gas. We define the pore size at which the adsorption films from both sides just meet in the pore center is the cutoff size. Once the pore size is smaller than the cutoff size, the adsorption film no longer exists since all the pore volume is occupied by adsorbed gas. Meanwhile, the average adsorbed density starts to increase with further decreasing pore size below cutoff size. The fluid composition is also expected to change under the same condition.

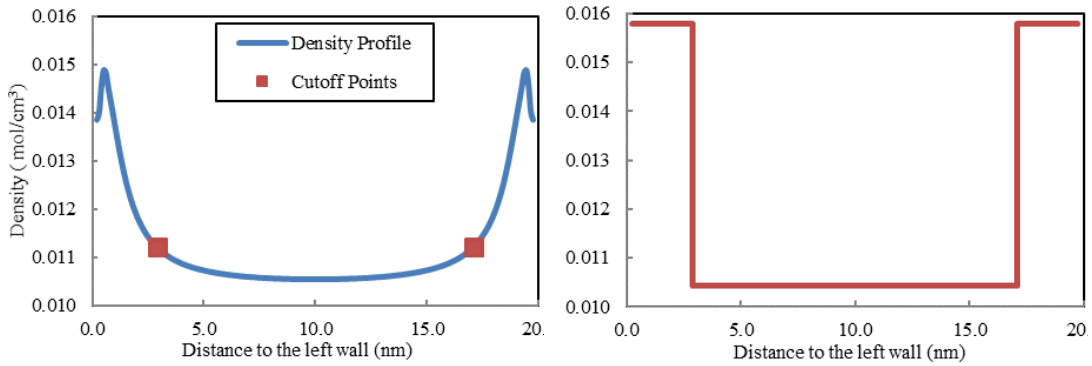

Figure 5.6— Continuous density profile (left) and averaged density profile (right) of the 80% C1/ 20% C4 mixture in the 20-nm pore at 170 °F and 3500 psi.

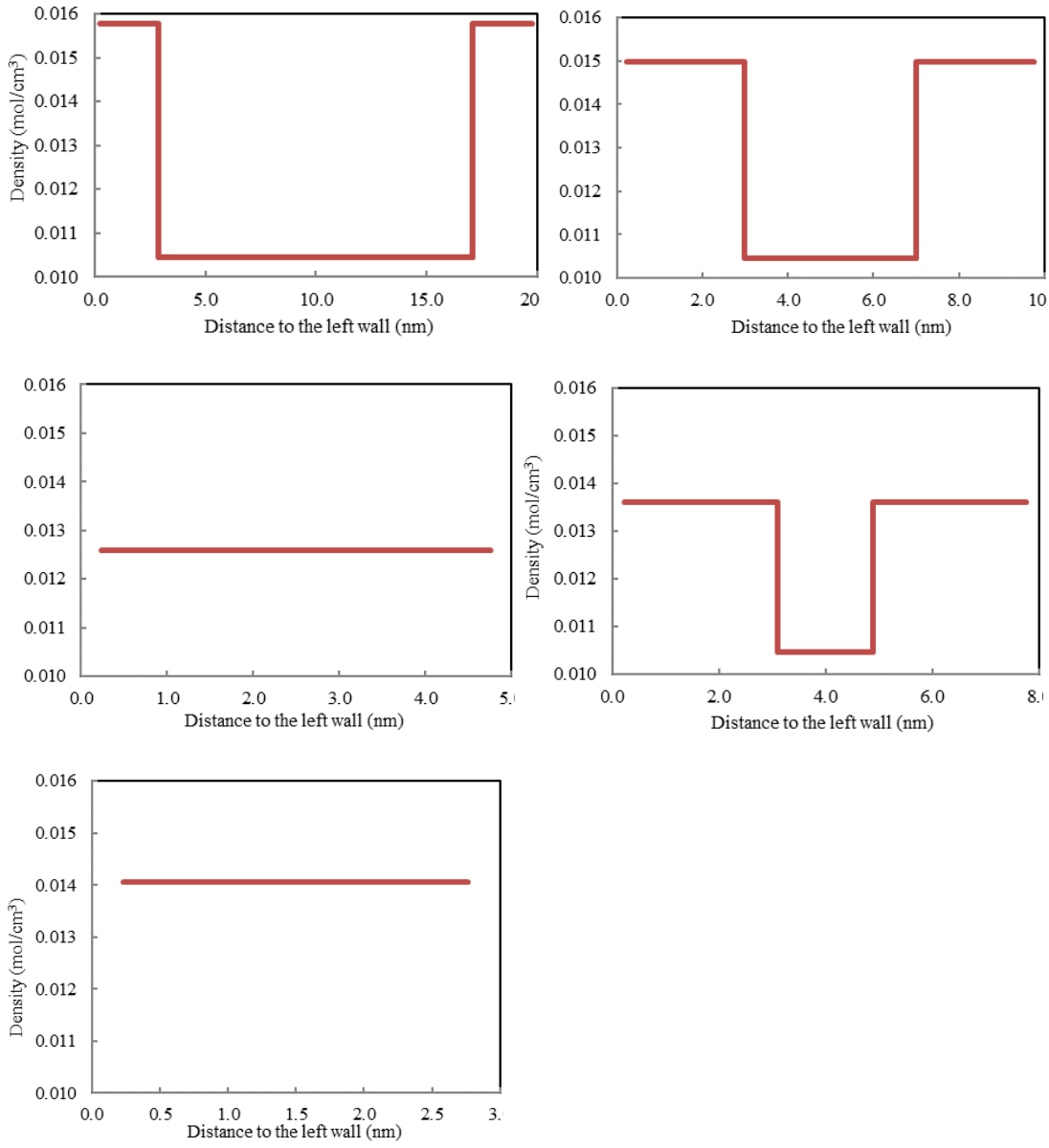

Figure 5.7— Averaged density profile of the 80% C1/ 20% C4 mixture at 170 °F and 3500 psi with different pore sizes (20 nm, 10 nm, 8 nm, 5 nm and 3 nm).

5.4 Pore Size Distribution and Pore Geometry Consideration in Kerogen

Kerogen is a porous material made by the organic matter that contains mixtures organic compounds in sedimentary rocks. The pore size in kerogen is typically within the range of 3-100 nm. It is well documented that the pore size has large impacts on gas adsorption (Mosher et al., 2013; Didar and Akkutlu 2013; Ma and Jamili, 2014). In order to consider such effects, pore size distribution is introduced in this GIP model. Here, we generate a series of pores with their pore sizes follow the normal distribution with specified mean pore size and standard deviation. In this model, the pores are all assumed to have cylindrical shapes with its diameter of the circular surface equal to half the height of the cylinder unless the specific pore geometry parameters are available. For simplicity, the curvature effects inside the pore have been neglected as of now. **Figure 5.8** shows a pore network established by cylindrical pores with different pore sizes to represent the pore network system in kerogen. It assumes that gas can only get adsorbed to the sidewall of the cylindrical pores. It is clear to see that when the pore size is small enough, there is only have adsorbed gas, but no free gas. With considerations of pore size distribution and pore geometry, it becomes possible to separately compute the volume occupied by free gas and adsorbed gas in kerogen based on statistical point of view. Note that the curvature effects of the cylindrical pores have been ignored as of now.

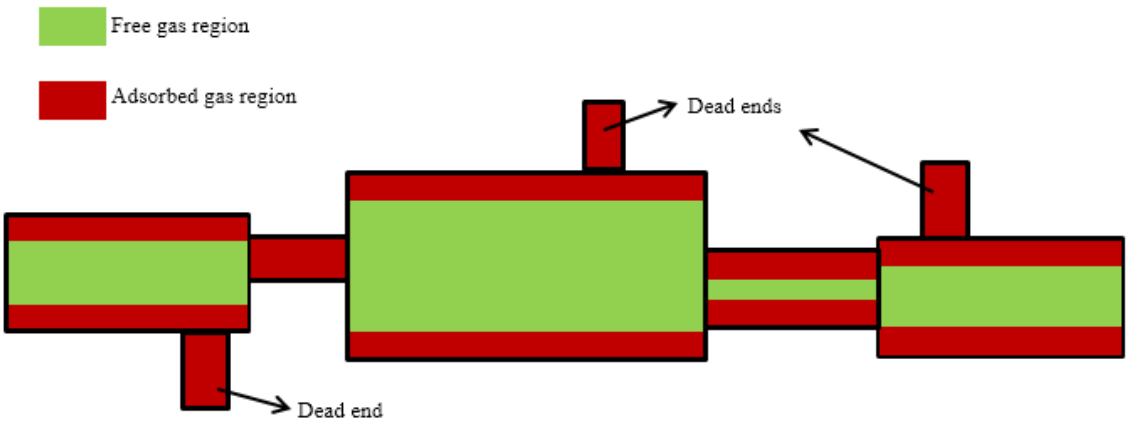

Figure 5.8— Pore network established by cylindrical pores with different pore sizes

Consider a series of pores. For those pores with their sizes less than the cutoff size, all the volume is taken by adsorbed gas. In this case, the total volume occupied by adsorbed gas is the same as the void volume created by these pores, $V_{ads,small}$, can be calculated as follows:

$$V_{ads,small} = \sum_{i=1}^{n} \frac{\pi D_i^{\,3}}{2} \quad \text{.....(5.8)}$$

Where n is the total number of pores with diameters less the cutoff size, D_i is the pore diameter for the *i*th pore. For the pores with their sizes larger than the cutoff size, the volume taken by the adsorbed gas, $V_{ads,large}$, can be computed as:

$$V_{ads,large} = \sum_{j=1}^{m} \left[\frac{\pi D_j^{\,3}}{2} - \frac{\pi (D_j - 2t)^3}{2} \right] \quad \text{.....(5.9)}$$

Where m is the total number of pores with diameters greater the cutoff size, D_j is the pore diameter for the *j*th pore and *t* represents the adsorption film thickness obtained

from SLD-PR model. Thus the total volume occupied by adsorbed gas is the summation of $V_{\text{ads,small}}$ and $V_{\text{ads,large}}$.

$$V_{ads} = V_{ads,small} + V_{ads,large} \quad \text{.....(5.10)}$$

Once the adsorbed gas volume has been obtained, the amount of free gas in kerogen, $G_{\text{f,org}}$, can be solved from Equation 5.6. In order to calculate the amount of adsorbed gas, G_{ads}, the properties of the adsorbed gas, including density and fluid composition, needs to be solved from SLD-PR model first. However, as discussed previously, these properties may vary from pores to pores with different sizes. To accurately compute G_{ads}, the amount of adsorbed gas in each single pore is accumulated:

$$G_{ads} = \sum_{k=1}^{n+m} \left[8.7355 \times 10^{5} \frac{V_{ads,k} \rho_{ads,res,k} Z_{ads,k}}{\overline{M}_{ads,k} \rho_b V_b} \right] \quad \text{.....(5.11)}$$

Note that when the total number of pores, $n+m$, is larger. Equations 5.9 and 5.11 can become time consuming. In such case, one can set up a few reference values of the each of the parameters (pore volume, adsorbed gas density and composition, etc.) calculated from chosen pore sizes, so these values from the rest of the pore sizes can be interpolated. Once G_{ads}, $G_{\text{f,org}}$ and $G_{\text{f,inorg}}$ are calculated from Equations 5.5, 5.6 and 5.11, the total GIP is obtained from Equation 5.1.

5.5 Eagle Ford Shale Play

We select the Eagle Ford shale play to investigate the total gas capacity by using the proposed new method. The Eagle Ford shale play is located at the Western Gulf basin in south Texas. It lies between the deeper Buda limestone and the shallower Austin Chalk formation, with depth in the range of [4,000-to 13,000] ft. From northwest to southeast and from the shallow zone to the deep zone, it covers all hydrocarbon windows, i.e. oil window, condensate window, and gas window. The condensate window is located at the middle of the shale play, seen in **Figure 5.9**. The depth of the condensate window is in the range of [9,000-to 10,000] ft. The average pay zone thickness is approximately 250 ft. Its temperature is in the range of [263-to 280] °F. The total organic content (TOC) of the Eagle Ford shale play is of 1% to 7%, and the porosity is in the range of 2 – 11% (Walls et al., 2011). **Table 5.1** gives the petrophysical and reservoir properties adopted for calculations. The pore size distributions of core samples of the Eagle Ford shale play have been derived by the NMR logging method, the nitrogen adsorption/desorption isotherm method, and the scanning electron microscope (SEM) method. The SEM study showed the SEM images of both kerogen pores and non-organic pores. The analysis results show that the pore sizes of organic pores and non-organic pores are in range of a few nm to a few microns (Walls et al., 2011; Rine, 2011). The average pore size used in the study is 20 nm, with a standard deviation of 10 nm.

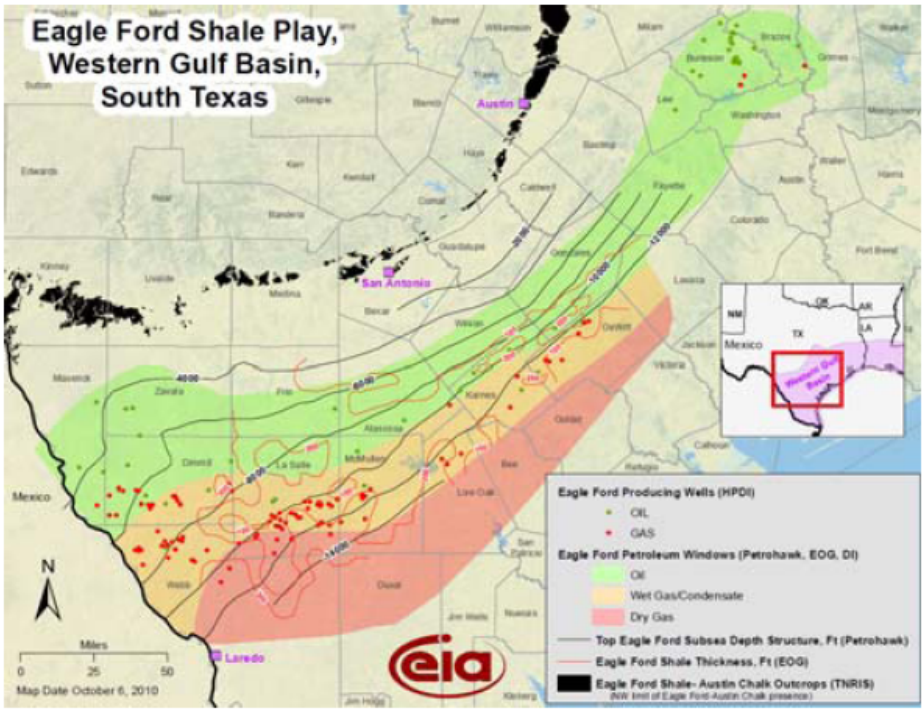

Figure 5.9— Eagle Ford hydrocarbon windows, source from EIA

TABLE 5.1—Effects of temperature on gas storage				
Temperature, °F	G_{st}, scf/ton	$G_{f,inorg}$, scf/ton	$G_{f,org}$, scf/ton	G_{ads}, scf/ton
270	128.4	37.2	50.0	41.2
280	126.7	36.6	47.9	42.2
290	125.1	36.0	47.3	41.9

Fluid samples from the Eagle Ford shale play were taken for PVT analysis. However, there exist only few published data for the fluid composition at the condensate window. Deo and Anderson (2012) used the fluid composition, listed in **Table 5.2**, or their reservoir description and fluid dynamic of the Eagle Ford shale (Deo and Anderson, 2012). In this study, we adopt their fluid composition and modified component $C6^+$ into C6, due to lack of fluid property data for $C6^+$. Also, i-C4 and i-C5 are treated n-C4 and n-C5, respectively for simplicity. The non-hydrocarbon gases CO_2 and N_2 are ignored in this study. **Table 5.3** gives the physical properties for fluids from C1 to C6. **Table 5.4** gives the binary interaction coefficients from Whitson and Brulé (2000). By using the new volumetric method, it shows that the total gas in place for the Eagle Ford condensate gas shale play is 132 scf/ton with the given parameters, from which 37 scf/ton is the free gas in inorganic matrix, 49 scf/ton is the amount of free gas in kerogen and 46 scf/ton is the total adsorbed gas amount. As we can see, the adsorbed gas amount is significant, which takes 35% of the total gas in place, although it only occupies relatively small portion of the total pore volume. **Figure 5.10** shows the total gas storage capacity, as well as the free gas in both kerogen and inorganic matrix and adsorbed gas storage capacity over the pressure range from 1 MPa to 50 MPa. It is clear to see that the adsorbed gas storage capacity is the highest among the three, but the differences with the other two are getting smaller as pressure increases. This is because the free gas is more sensitive to pressure, since it is much easier to compress, compare to the adsorbed gas, which is already very packed. As we can predict, when the pressure is high enough, the amount of free gas can exceed the adsorbed gas and becomes dominant.

TABLE 5.2—Effects mean pore size on gas storage				
Mean pore size, nm	G_{st}, scf/ton	$G_{f,inorg}$, scf/ton	$G_{f,org}$, scf/ton	G_{ads}, scf/ton
10	129.4	37.2	41.7	50.5
30	127.5	37.2	56.7	33.7
50	126.4	37.2	65.4	23.7

TABLE 5.3—Effects pore size standard deviation on gas storage				
Pore size standard deviation, nm	G_{st}, scf/ton	$G_{f,inorg}$, scf/ton	$G_{f,org}$, scf/ton	G_{ads}, scf/ton
5	129.3	37.2	42.4	49.7
10	128.3	37.2	50.0	41.2
15	127.6	37.2	56.2	34.2

TABLE 5.4— Effects of fluid composition on gas storage					
C1 Composition	G_{st}, scf/ton	$G_{f,inorg}$, scf/ton	$G_{f,org}$, scf/ton	G_{ads}, scf/ton	Ads film thickness, nm
80 %	140.5	36.7	51.1	52.8	2.25
60 %	139.0	37.4	53.2	48.5	2.15
40 %	136.1	36.6	57.4	42.2	1.74
20 %	132.4	34.8	58.5	39.1	1.44

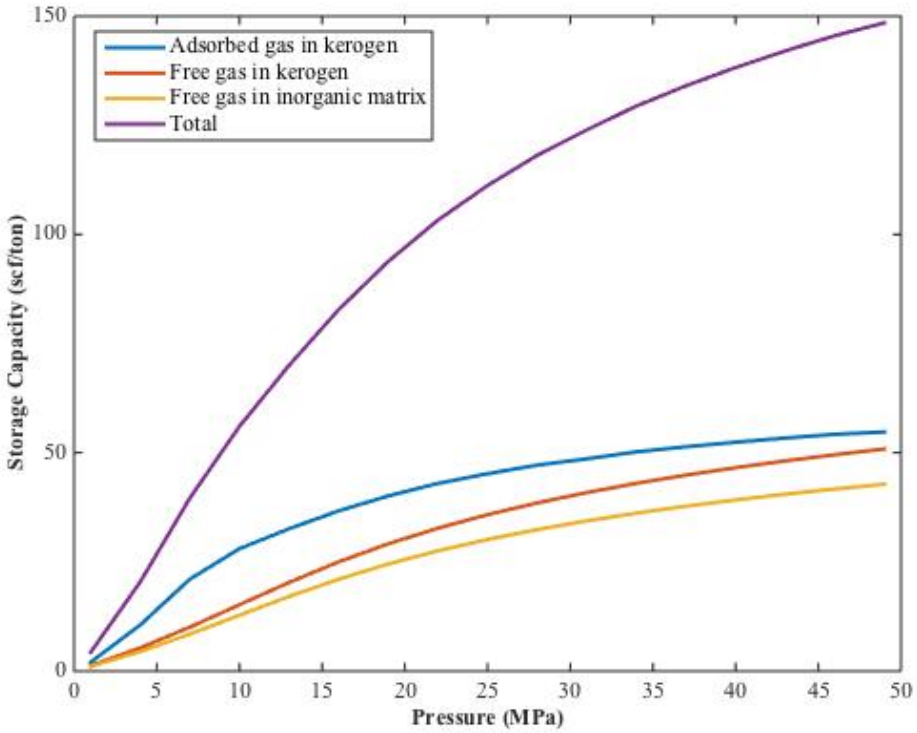

Figure 5.10— Total gas, free gas and adsorbed gas storage capacity over the pressure range from 1 MPa to 50 MPa

Chapter 6: Adsorption and Capillary Condensation of Hydrocarbon Mixtures in Heterogeneous Nanoporous Shales

6.1 Background and Previous Work

It is well known that fluid can be adsorbed on solid surfaces (Langmuir, 1918; Masel, 1996). In conventional rocks where the pore size is large (in the order of millimeters), the amount of fluid adsorbed is usually ignored compare to large portion of the bulk fluid. When the pore size becomes extremely small in shale rocks (order of 1-100 nm), the surface area to volume ratio of these pores becomes significant. The space occupied by adsorbed fluid is comparable to that of the bulk fluid and is no longer negligible. Although the processes of adsorption have been well studied in the past century, hydrocarbon adsorption in shales remains a challenge because of the complexity of the reservoir environment: high-pressure-high-temperature condition, strong heterogeneity of the porous rock (Loucks et al., 2012), and multi-component fluid content. It is a common belief that the fluid is in bulk state in fractures, inorganic pores and the center portion of the large organic pores, while the adsorbed fluid is mainly associated with the organic constituent of shale (Ambrose et al. 2012). Some progress has been made toward the understanding of adsorption in shale recently. Ambrose et al. (2012) performed molecular dynamic simulations to predict the density distribution of pure methane in nanometer slit graphite pores at 353 K and 21 MPa. Results showed multi-layer adsorption of methane occurred on the graphite walls with width ranging from 1.14 to 3.93 nm. Didar and Akkutlu (2013) performed Monte Carlo simulations to study the fluid behaviors of binary

hydrocarbon mixtures (C1/C2 and C1/C3). They found that the fluid molecules of the heavier component preferred to stay in the adsorbed phase. Mosher et al. (2013) used grand canonical Monte Carlo (GCMC) simulations to investigate methane adsorption in mircro- and mesoporous carbons. Results showed that methane adsorption loading was highly sensitive to pore size. The maximum methane excess adsorption at 298 K in 0.4-nm size pore was 12.5 times greater than that in the 9.0-nm size pore. These molecular simulation studies provide details of fluid behaviors in nanoscale pores; however, they are computationally intensive. It limits applications in simulating bigger scale processes (order of approximately 100 nm and bigger).

For pure fluid, capillary condensation describes the phenomenon that the vapor to liquid phase transition happens below the saturation vapor pressure of the fluid in confined pore space. Such process has been known and studied over a century (Thomson, 1872). Capillary condensation can be seen in adsorption isotherm experiments when the temperature is below the fluid critical temperature, where a sudden or rapid increase in fluid adsorbed amount occurs before the saturation pressure and a hysteresis loop may occur during the process of adsorption and desorption (Thommes et al., 2015). There are also many models available to predict the phase transitions of capillary condensation, such as Grand Canonical Monte Carlo (GCMC) simulation, Gibbs Ensemble Monte Carlo (GEMC) simulation, Quench Molecular Dynamics, Density Functional Theory (DFT) (Tarazona et al. 1987; Gelb et al. 1999; Monson 2005). Although capillary condensation is nothing new, the petroleum industry has just started to get more attentions on this subject due to the recent boom of unconventional shale resources and its potential existence in those very tight shale resource rocks (5-10 nm pore sizes). In one of earlier

papers (Chen et al. 2012), capillary condensation of n-hexane was observed in the shale core plugs. This was the first evidence of capillary condensation of hydrocarbon in shale resource rocks. In a latter paper (Chen et al. 2013), it was pointed out that the capillary condensation does not occur in shales if the hydrocarbon is nearly 100% methane because the reservoir temperature is much higher than the methane critical temperature (190.6 K). Instead, capillary condensation may occur when the petroleum fluid contains sufficient amounts of intermediate and/or heavy components, which is the case for many condensate gas shale plays such as the Eagle Ford, Barnett and Marcellus shales. However, many of the condensate fluids exhibit retrograde behaviors. That is, one may experience two dew point pressures of the fluid during one isothermal compression or expansion. In this case, capillary condensation can shift both the upper and lower dew point pressures from their bulk values. Such changes may have significant impact on fluid-in-place if the original reservoir pressure is close to the dew point pressure. Meanwhile, it can also help to predict the condensate dropout for different pore sizes under the influence of capillary condensation. Presence of capillary condensation in shale reservoirs can have significant impact in reserve estimation and "gas" production. If indeed, some or a majority of the hydrocarbon exists as liquid-like condensation in some shale reservoirs, the reserves would be much higher than current industry model predicted. In addition, the presence of capillary condensation in nanopore throats and/or small pores can block gas flow and, thus, alter matrix transport during production. Therefore, occurrence of capillary condensation needs to be carefully evaluated to predict production in shale reservoir engineering.

In this chapter, we use the SLD model building upon thermodynamic equilibrium relations to predict fluid density distributions and adsorption for both pure components and mixtures. The SLD model is one type of DFT and was first developed by Rangarajan et al. (1995) to study the physical adsorption over large pressure ranges including the supercritical ranges. The model considers both the fluid-fluid interactions from equations of state and fluid-pore wall interactions from Lennard-Jones potential energy functions. A modified PR-EOS (Chen et al., 1997) is used to account for the modified fluid-fluid interactions under confinement. Lee's partially integrated 10-4 Lennard-Jones potential (Lee, 1988) is adopted to predict the fluid-pore wall interactions between hydrocarbon molecules and surface wall. We then use Young-Laplace equation coupled with original PR-EOS to account for the capillarity effects and predict capillary condensation of a binary mixture in a heterogeneous pore system. In addition, the Young-Laplace equation is modified to consider the effects of the thickness of the adsorbed layer on pore radius. The reason to use original PR-EOS instead of a modified one is that we exclude the adsorbed fluid near the surface wall and treat the fluid in the center as bulk fluid.

6.2 Modified Young-Laplace Equation

In physics, the Young-Laplace equation is used to describe the pressure difference across the interface between the wetting phase and the non-wetting phase in a media. Such pressure difference is known as capillary pressure shown in Equation 6.1:

$$P_C = P_{\text{non-wetting}} - P_{\text{wetting}} \quad \text{.....(6.1)}$$

where P_C is the capillary pressure. In an oil/gas two phase system, gas is the non-wetting phase and oil is the wetting phase. When the oil and gas are inside a porous system, the pore networks were treated as tube shaped. The Young-Laplace equation in such a tube-shaped pore system can be written as

$$P_C = P_G - P_O = \frac{2\gamma\cos\theta}{r} \quad \text{.....(6.2)}$$

where γ is the interfacial tension, r is the pore radius and θ is the contact angle of the oil/gas interface to the pore wall. Since the pore wall is covered with the adsorbed fluid, the oil and gas phases in the center of the pore have no direct contact to the pore wall and they are completely wet to the adsorbed layers. Therefore, the contact angle θ is 0. Meanwhile, the thickness of the adsorbed fluid can also reduce the pore space occupied by bulk oil and gas fluid, causing the reduction of the pore radius. To correct this, the effective pore radius should be used in Equation 6.2 by subtracting the original pore radius by the adsorption thickness t, similar to the classical treatment by BJH (Barrett et al., 1951). Equation 6.3 then becomes:

$$P_C = P_G - P_O = \frac{2\gamma}{r-t} \quad \text{.....(6.3)}$$

Equation 6.3 is the modified version of the Young-Laplace equation in a capillary tube. In fact, people have been aware of the importance of the adsorption thickness in shales on gas-in-place, pore size reduction and other aspects in the past few years (Ambrose et al. 2012; Li et al. 2014; Tan and Piri 2015), but there is no clear and accurate path for calculation of the adsorption thickness. Although attempts have been made by using the Shapiro's adsorption film model (Shapiro and Stenby 1996) to estimate the adsorption film thickness as an approximation (Li et al. 2013; Li et al. 2014), the many assumptions

of the model and its limitation that it is applicable only close to the dew point pressure makes the model less attractive and impractical over larger pressure range. In the next section, we propose a new method to predict the adsorption thickness from fluid density distributions across the pore calculated from the SLD model. The determined value of the adsorption thickness is then adopted in Equation 6.3 for pore radius correction.

In Equation 6.3, the interfacial tension γ is determined by the parachor equation:

$$\gamma = \left\{ \sum_{i=1}^{n_c} Pch_i \left[x_i \rho_{\mathrm{b}}^{\mathrm{O}} - y_i \rho_{\mathrm{b}}^{\mathrm{G}} \right] \right\}^4 \quad \text{.....(6.4)}$$

where Pch_{i} is the Parachor of component i, x_i and y_i are the composition of component i in oil and gas phases respectively and $\rho_{\mathrm{b}}^{\mathrm{O}}$ and $\rho_{\mathrm{b}}^{\mathrm{G}}$ are the bulk molar density of the oil phase and gas phase, respectively. To calculate the fluid composition and density in both phases, an equation of state is needed and PR-EOS is used. While in the PR-EOS, instead of using the same pressure, the oil pressure and gas pressure are used separately in the corresponding phases. With known gas pressure, an iterative method is used to update the interfacial tension to calculate the oil pressure using Equation 6.3. Successive substitution is used here for convergence. We then apply such PR-EOS considering the capillary effects to the phase split calculations to estimate the adjusted saturation pressures (dew point pressures or bubble point pressures) by given fluid composition, temperature and pore radius. In the condensate/ retrograde gas region, this shift in dew pressures is the feature of capillary condensation of the hydrocarbon mixture.

6.3 Adsorption Thickness Determination with the Presence of Capillary Condensation

The fluid density distributions across the pore for both pure components and mixtures as well as the compositional distributions of mixtures were calculated from the SLD model, as we discussed in Chapter 3. In this paragraph, as an example, we show typical density and compositional distributions of a synthetic binary mixture that contains 50% methane and 50% ethane in an 8-nm pore at 350 K and 10 MPa (**Figure 6.1**). The figure shows that the fluid density increases rapidly approaching the wall but continuously without a clear boundary between the adsorbed region and the bulk region, indicating that there is no clear interface between the "so-called" adsorbed phase and the bulk phase in a pore that is just a few nanometers wide. In order words, the fluid does not experience a "phase-transition" in the near-wall region, although its density and the properties deviate significantly from those of the bulk fluid. This finding implies that the traditional theories, which treat the adsorption layer as a well-defined homogeneous liquid-like thin film (Evans et al. 1986; Shapiro and Stenby 1996), may not be suitable for hydrocarbon adsorption at subsurface conditions in shales, where many of the pores are in the order of nanometer.

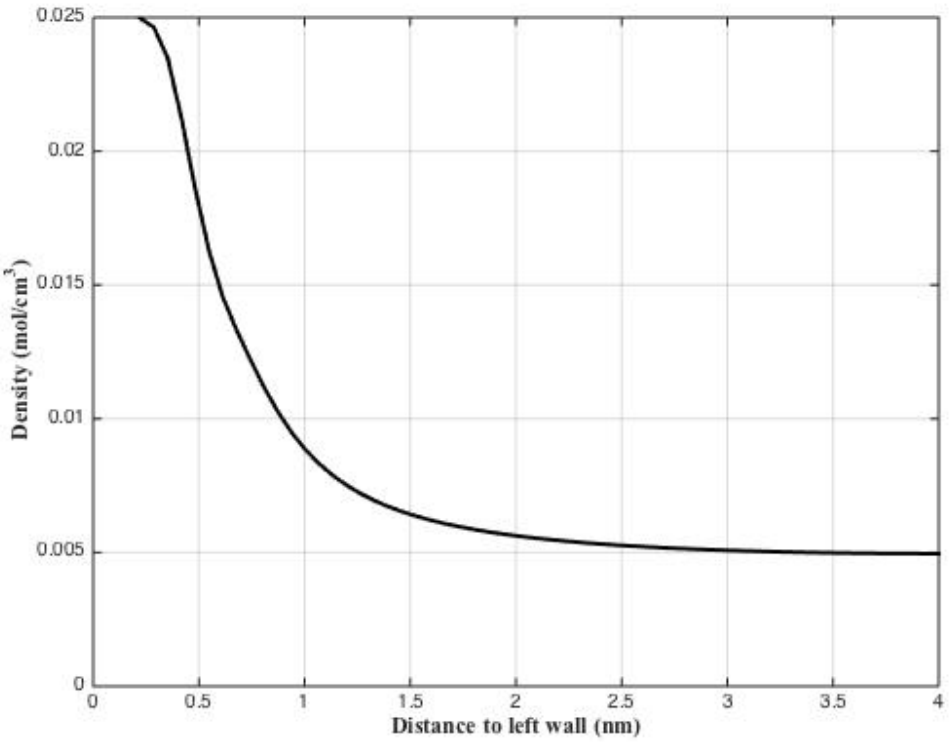

Figure 6.1—Density distribution of equal molar C1/C2 binary mixture an 8-nm pore at 350 K and 10 MPa. Only half of the symmetric pore is shown.

It is important to determine the adsorption thickness in order to calculate the effective pore radius. Although there is no clear transition between the adsorbed and the bulk region, an artificial cut-off is desired for this purpose. Walton and Quirke (1989) stated that the structure of the adsorbed layers was independent of the bulk region in the pore. It indicates the fluid in the adsorbed region is not sensitive to the phase transition, i.e. capillary condensation, in the bulk in the center of the pore. This supports the idea that an effective pore radius should be used to predict the capillary condensation because the bulk fluid cannot "feel" the real pore size with the presence of the adsorbed layers. Based on the criteria of adsorbed region definition from Walton and Quirke (1989), discrete density profiles of hydrocarbons in nanopores are used to evaluate the density change of

each molecular layer over a large pressure range including a phase change. Consider pure ethane confined in a 5.33 nm wide slit graphite pore at 300 K, **Figure 6.2** shows a series of ethane discrete density profiles in half of the pore with bulk pressure ranges from 0.5 to 50 MPa. A discrete density profile is generated by averaging the continuous fluid density within each molecular layer (with its width equals to the molecular diameter) across the pore. As we can see from the figure, six ethane-layers occupy the half space of the pore. The averaged ethane density at each layer is building up as pressure increases. Phase transition from vapor-like fluid to liquid-like fluid in the center region of the pore is seen between 4 and 4.5 MPa (the saturation pressure of ethane at 300 K is 4.36 MPa). **Figure 6.3** shows density change with respect to pressure for each of the six ethane-layers from 0.5 to 50 MPa. The red dashed line in the figure represents the bulk vapor saturation pressure (4.36 MPa), above which the vapor-liquid phase transition will happen in bulk. It is clear to see that layer 1, which is the layer closest to the left wall, has the highest density and becomes almost constant when the pressure is larger than 3.5 MPa. This means layer 1 becomes "saturated" with ethane molecules after pressure reaches about 3.5 MPa and becomes insensitive to further pressure increase or the phase changes inside the pore. For the second layer, the density is much lower and close to bulk density for pressure less than 0.5 MPa. After that, its density starts to build up rapidly in the pressure range of 0.5 to 3.5 MPa and becomes almost "saturated" thereafter. These two layers, since their densities stabilize at pressure much less than the vapor-liquid phase transition pressure, are considered as adsorbed layers. Therefore, the adsorption thickness in this case equals to two ethane molecular diameters. For the rest four layers, sharp changes in density are observed indicating the occurrence of phase transition. It is, however, surprised to see

that the phase transition happened at different pressures for different layers, but all lower than the bulk saturation pressure. The closer the layer is to the wall, the earlier the phase transition occurs. If we subtract the original pore radius by two adsorbed ethane layers, the effective pore radius is obtained to be 1.78 nm instead of 2.67 nm. We then use the modified Yong-Laplace equation to predict the confined vapor saturation pressure (blue dashed line in Figure 6.3). As we can see, it is able to predict the confined vapor saturation pressure of the two ethane layers in the center of the pore. The phase transition of the two layers closer to the wall happens even earlier than what is predicted, due to the relatively stronger fluid-pore wall interactions. We define these two layers as transition layers since they do not follow exactly neither adsorption process nor phase transition process but lies in between. It can be found from this case that capillary condensation can occur in the center of the pore and the transition pressure can be predicted by the modified Yong-Laplace equation. While in the region near the pore wall where adsorption is dominated, the fluid cannot feel the phase transition because the space has been already fulfilled due to strong fluid-wall interactions.

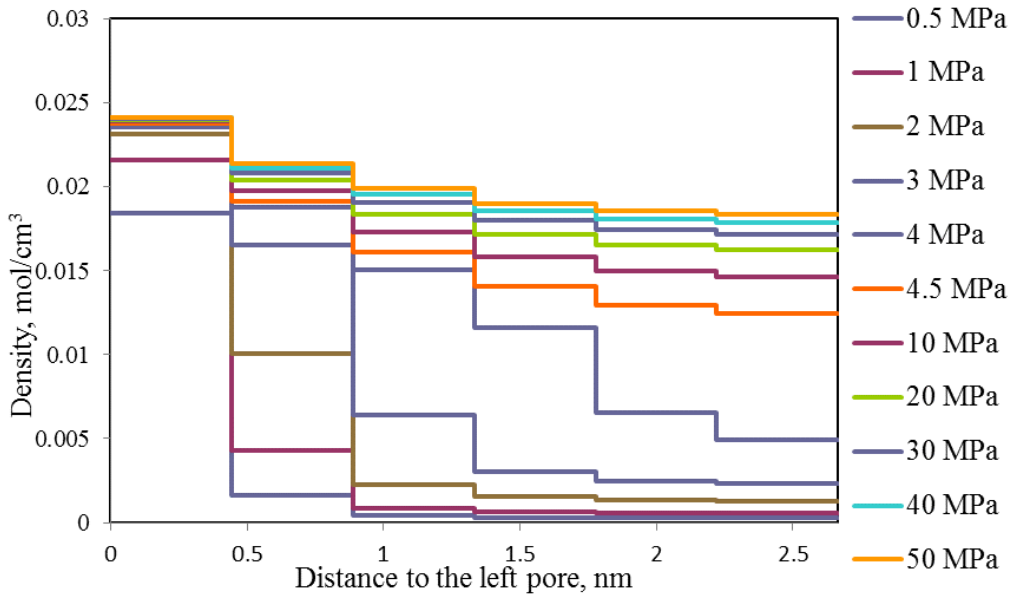

Figure 6.2—Ethane discrete density profiles in left half of the pore with bulk pressure ranges from 0.5 to 50 MPa.

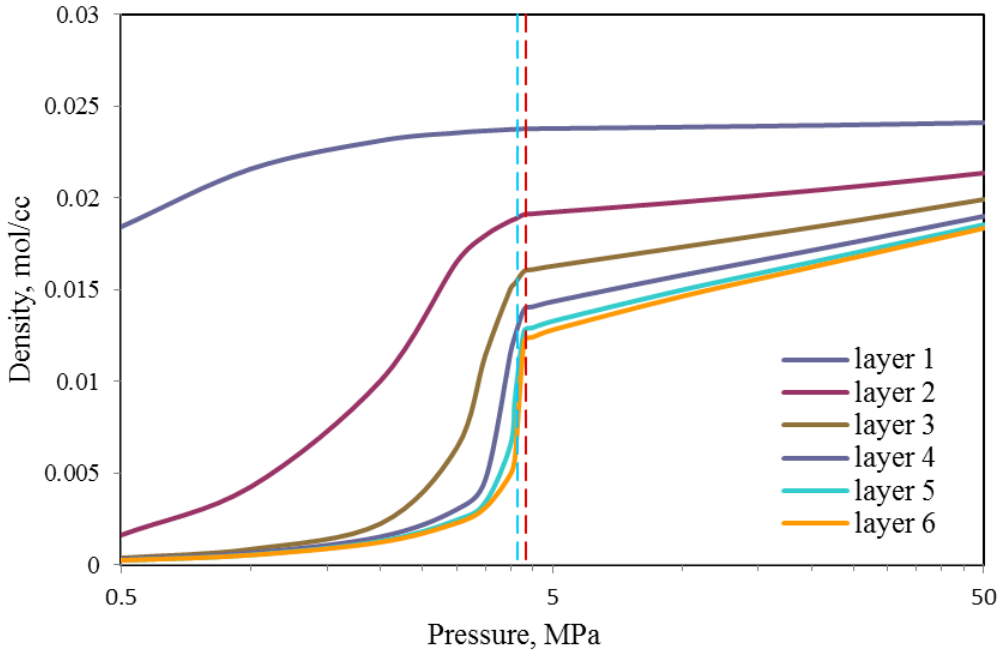

Figure 6.3—Ethane density change with respect to pressure for each of the six ethane-layers from 0.5 to 50 MPa at 300 K. The red dashed line is the bulk ethane saturation pressure and the blue dashed line is the confined saturation pressure calculated by the modified Young-Laplace Equation.

6.4 Adsorption Isotherms in Heterogeneous Nanopore Systems Above Cricondentherm Temperature

Adsorption isotherms describe the equilibrium state of fluid sorption in a porous material with incremental pressures at constant temperature. In physical chemistry and material science area, adsorption isotherms have been utilized to investigate the pore structures and pore size distribution (PSD) of the material as well as fluid separations over a long time. While in our study, with known pore structures and PSD from petrophysical analysis, we aim to use adsorption isotherms to predict the storage capacities of hydrocarbons in shales at reservoir conditions.

In Chapter 4.4, adsorption isotherms of pure hydrocarbon components and their mixtures in a single pore system were generated using the SLD model. The results were in good agreement with experimental studies and molecular simulations. In this part, we extend the method to a heterogeneous pore system to investigate the fluid behavior in different size pores at variety pressure conditions. Consider a pore system contains two parallel graphite pores with different pore sizes, 8 and 20 nm, respectively. The pores have slit shape and the same pore volume and are connected to a bulk system where the pressure, temperature and fluid composition are assumed to be constant. A binary mixture of 50% methane (C1) and 50% propane (C3) is used. The temperature is fixed and the pressure range is from 0.01 to 50 MPa. The system temperature is chosen to be higher than the temperature at cricondentherm point of the C1/C3 mixture so that the pressure path is on the right side of the two-phase envelop of the mixture on a Pressure-Temperature (PT) phase diagram (as shown in **Figure 6.4**). In this case, capillary condensation does not

occur along the isothermal pressure path (details of capillary condensation and its effects are discussed in the next section).

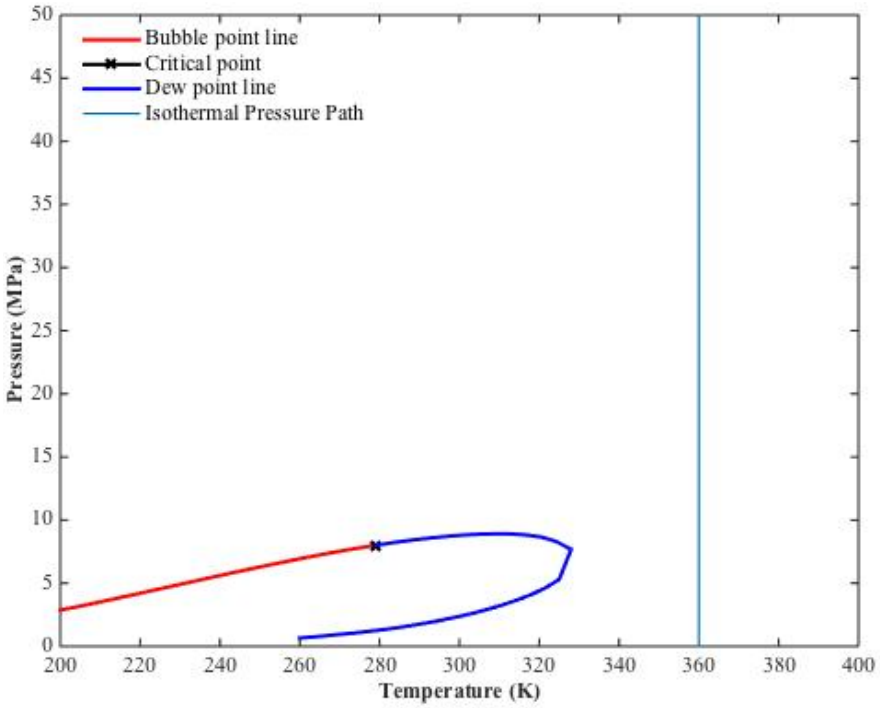

Figure 6.4—The bulk two phase envelope of equal molar C1/C3 mixture and the isothermal pressure path at 360 K from 0.01 to 50 MPa.

Figure 6.5 shows the total adsorption isotherm and the partial adsorption isotherms of each component in each pore over the pressure range. Without the information of the adsorbent, the fluid content is shown as molar density. Figure 6.5a gives the amount of total, bulk and adsorbed fluid from 0.01 to 50 MPa. When the pressure is lower than 5 MPa, the pores mainly contains adsorbed fluid. As pressure get higher, bulk fluid density becomes dominant and the amount of adsorbed fluid even starts to decrease as pressure reaches 8 MPa. This indicates that the confined fluid tends to behave similar to bulk fluid in terms of density at high pressure. Figure 6.5b shows the partial adsorption isotherms of each component in each pore. The adsorbed and bulk fluid is not distinguished. As we

can see from the plot, the amount of C3 stored is higher than C1 in each pore. This is the result of preferential adsorption of heavy component (C3) compare to light component (C1) in organic nanopores. Larger attraction forces between pore wall molecules and propane fluid molecules bring more propane than methane into the pore space, especially at low-pressure range and in smaller pores.

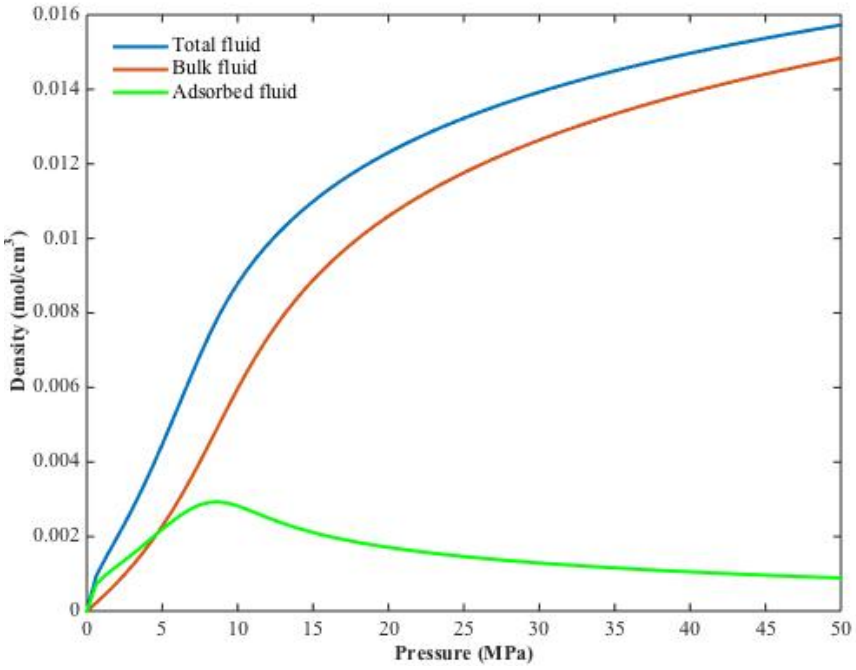

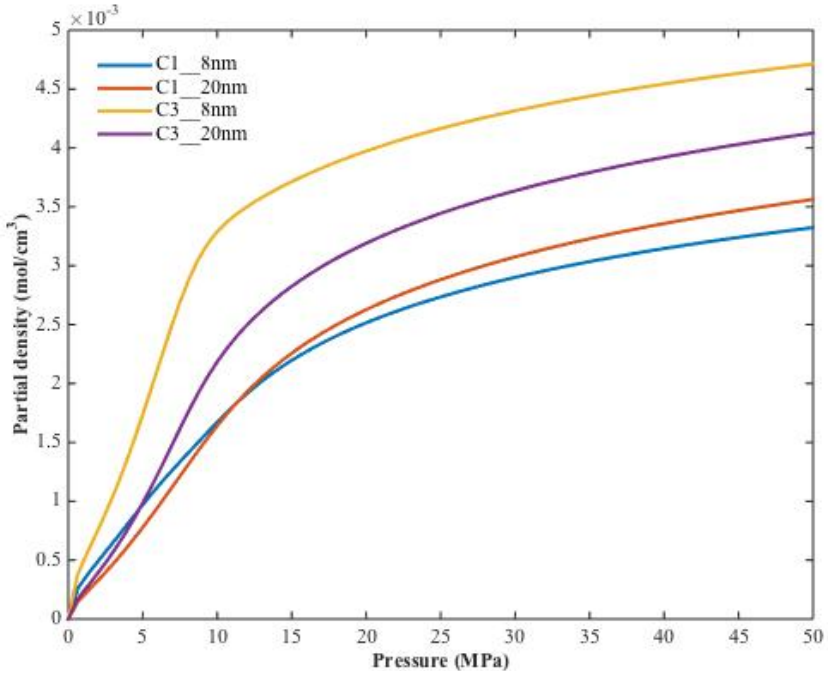

Figure 6.5—Adsorption isotherms of C1/C3 mixture in a two-pore system. (a) Total, bulk and adsorbed fluid content of C1/C3 mixture. (b) The C1 and C3 fluid content in 8 and 20 nm pores.

Figure 6.6 shows the plots of the ratio C3/C1 in the 8 nm and 20 nm pores over the pressure range, illustrating the selectivity of C3 over C1. The selectivity describes the ratio of the total amount of one component over the other in a binary mixture. In this case, the value of selectivity is the ratio of the amount of C3 to C1 at any particular pressure. When pressure is low, the pore space is mainly filled with C3 and therefore C3 composition keeps increasing as pressure goes higher. The effect of preferable adsorption of C3 is more significant in the 8-nm pore than that in the 20 nm pore, where the average fluid-pore wall interaction is relatively much weaker. When the pressure reaches about 8 MPa, maximum values of C3 selectivity are seen in both pores (2.04 and 1.34 for 8 and 20 nm pores, respectively), according to Figure 8. Further increase in pressure results in

declination in C3 selectivity, which decreases fast at first and then slows down as pressure gets higher and has the values of 1.42 and 1.16 for 8 and 20 nm pores at 50 MPa, respectively. This implies that at high pressure the density of bulk phase is high and close to the adsorbed phase. It is obvious, from Figure 7 and Figure 8, that 8 nm pore contains larger amount of C3 while 20 nm pores has larger amount of C1, indicating that heavier molecules are more likely to stay in smaller pores. The size of pores in kerogen can have very wide distribution from a few nm to a few hundred nm. Our calculation suggests that heavier component tends to accumulate into smaller pores while methane stays in larger pores.

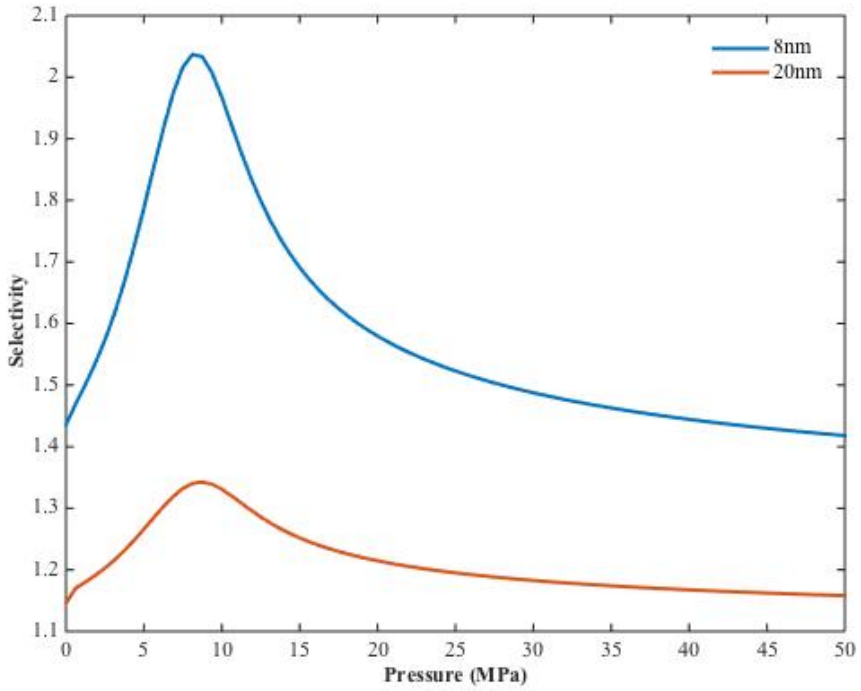

Figure 6.6—Selectivity of C3 over C1 in 8 and 20 nm pores over the pressure range of 0.01 to 50 MPa.

6.5 Capillary Condensation of Retrograde Mixtures

In this section, we investigate the effects of capillary condensation on retrograde hydrocarbon fluid with the presence of adsorption in heterogeneous pore system. Consider a binary mixture of methane (C1) and n-pentane (nC5) confined in a pore system that contains two parallel graphite pores with the same pore volume but different pore sizes, 14 and 24 nm in diameter, respectively. The pores are assumed to be connected to an open system with fixed temperature of 360 K and fluid composition of 80% C1 and 20% nC5. The adsorption region contains two layers of molecules with the thickness of 1.1 nm based on the adsorption thickness calculation. Therefore, the effective radiuses of the two pores become 5.9 and 9.9 nm, respectively. The isothermal pressure path from 0.1 to 20 MPa at 360 K travels through the two-phase region of the mixture, as shown in **Figure 6.7**. The pressure path intersects twice with the dew point line of the phase envelop, which indicates the retrograde behavior of the fluid. The two-phase envelop in the plot is for bulk fluid. However, it is known that the two-phase envelop will shift due to capillary effects (Li et al. 2014; Jin and Firoozabadi 2016). **Figure 6.8** gives the adsorption isotherms of each component in each pore and their total. From the plot, we can see that the total fluid content experiences two sudden declines. The two jumps are the sign of capillary condensation in the two different size pores respectively, while the two sudden decreases represent the capillary evaporation of the fluid confined in the two pores. Note that the fluid content change is much larger for capillary condensation than capillary evaporation due to the fact that the capillary evaporation happens at a much higher pressure where the density different between the liquid and the vapor is much smaller compare to that at capillary condensation. From quantitative point of view, the

capillary condensation in 14 and 24 nm pores occurs at 2.6 MPa and 2.8 MPa, respectively; the capillary evaporation in the two pores occurs at 15.6 and 15.7 MPa, respectively, while the bulk lower and upper dew point pressures of the mixture at 360 K are 3.1 and 15.5 MPa, respectively. As we can figure out, the capillary condensation happens before the pressure reaches the lower dew point pressure and the capillary evaporation occurs after the pressure exceeds the upper dew point pressure. This is how the two-phase envelop shifts under the effects of capillarity. We can see that the smaller the pore size, the larger the shift of the dew point pressures one can have. It is also observed that the shift of lower dew point pressure is more significant than that of the upper dew point pressure under the same confining environment. On the other hand, the partial adsorption isotherms of each component in each pore in Figure 6.8 give more detailed information on the fluid behavior during the process of the phase transition. During the process of capillary condensation, there is a huge jump in nC5 content and a slight decrease in C1 content indicating the phase change from vapor-like fluid to liquid. As pressure increases in the two-phase region, nC5 content decreases while the amount of C1 increases based on the flash calculation results. Note that although the liquid fraction changes with pressure, we assume the pores are fully filled with condensed liquid once capillary condensation happens due to the assumption that the pores are connected to an infinite large open system. At capillary evaporation, slight but steep changes of C1 and nC5 contents imply the phase change from liquid to vapor. When the pressure is higher than the capillary evaporation point, there is no more capillary condensation. However, at these pressures the density of the fluid in the pores is not far from the liquid.

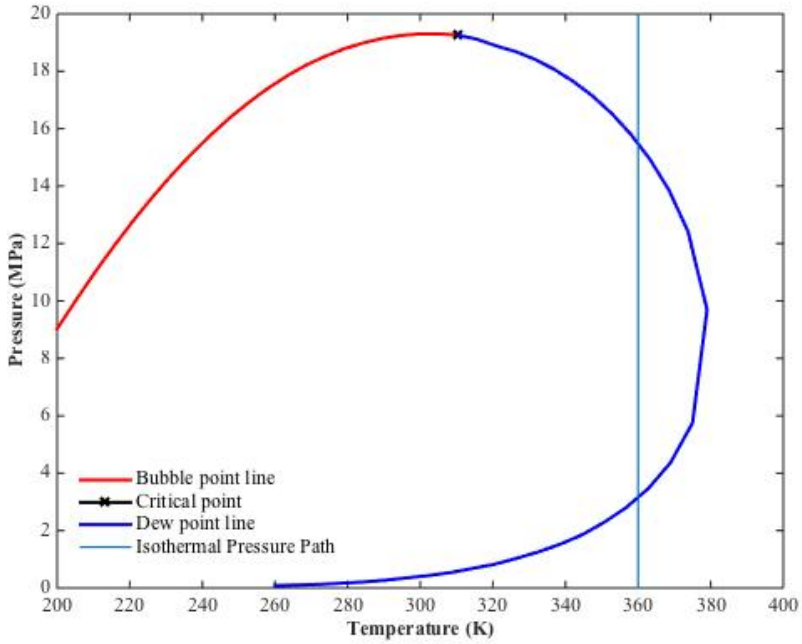

Figure 6.7—The bulk two phase envelop of a binary mixture with composition of 80% C1 and 20% nC5 and the isothermal pressure path at 360 K from 0.01 to 20 MPa.

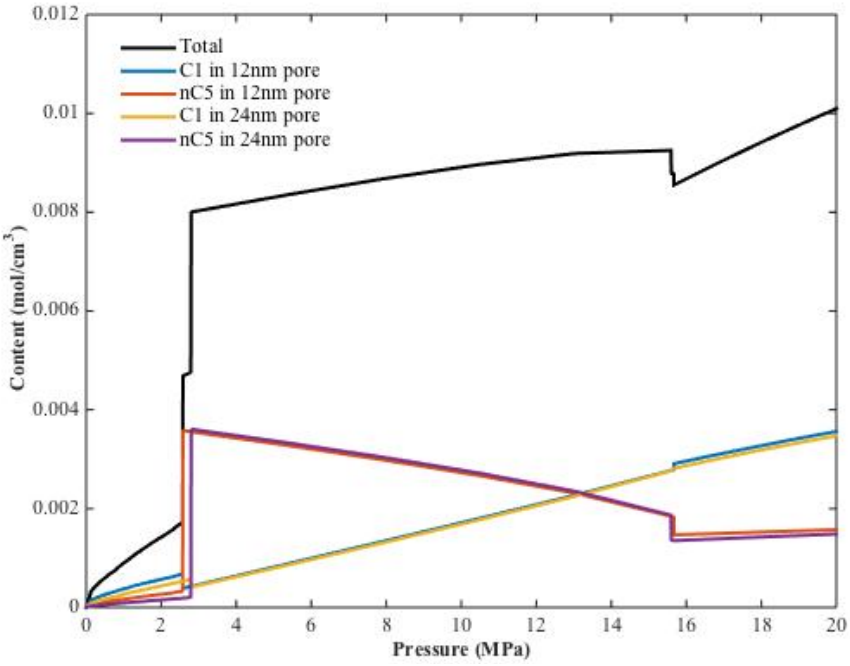

Figure 6.8—Adsorption isotherms of each component in each pore and their total of a binary mixture with composition of 80% C1 and 20% nC5 at 360 K from 0.01 to 20 MPa.

Chapter 7: Molecular Dynamics Simulations of Hydrocarbons in Nanopores

7.1 Background and Previous Work

In Chemical Engineering, molecular simulation techniques have been applied to study confined phase behavior for many years (Evans, 1990; Gelb et al., 1999; Koga et al., 2001; Frenkel and Smit, 2001; Alcoutlabi and McKenna, 2005). Their main purposes are to investigate the fluid properties in nanoporous materials, such as carbon nanotubes, polymers and porous glasses. Until recently, because of the booming of shale comes to public, when people realize that fluid behavior in shale media is substantially different from that in conventional reservoirs, they have started to utilize molecular simulation techniques to help understand the fluid behaviors in shales. Ambrose et al. (2012) performed a molecular dynamics simulation study to investigate the adsorption of methane in a graphite slit. Density profiles of methane across the pore were obtained from molecular dynamic studies. From the methane density profiles, they found that the density values of the adsorbed layers were usually 2 to 2.5 times higher than the methane bulk density. Didar and Akkutlu (2013) performed Monte Carlo simulations to study the fluid behaviors of binary hydrocarbon mixtures (C1/C2 and C1/C3). They found that the fluid molecules of the heavier component preferred to stay in the adsorbed phase. Mosher et al. (2013) used grand canonical Monte Carlo (GCMC) simulations to investigate methane adsorption in mircro- and mesoporous carbons. Results showed that methane adsorption loading was highly sensitive to pore size. The maximum methane excess adsorption at 298 K in 0.4-nm size pore was 12.5 times greater than that in the 9.0-nm size pore. Welch and Piri (2015) performed molecular dynamics simulations to investigate retrograde

condensation of ethane and heptane in oil-wet nanopores to represent the confined hydrocarbon fluid behavior in organic nanopores in shales. From the results, they concluded that molecular dynamics simulations with appropriate force field are able to capture the phenomenon of retrograde phase behavior for the particular hydrocarbon binary fluid. They found that high oil-wet nanoscale pore is more likely to induce condensation at lower pressures than the bulk at 310 K. But the same is not seen at 365 K due to the sealing effect of the condensation to the narrow pores which may slow down the processes. Sedghi et al. (2016) utilized large-scale molecular dynamics simulations to perform the oil-water/brine displacements in a calcite nanopore which represents shale inorganic matrix. The threshold capillary pressures between oil and water/brine in calcite that account for fluid-wall interactions are obtained under variety of oil composition, water salinity and temperature and pressure conditions. They found that because of the adsorption of water layers on calcite pore walls and the strong ordering of water molecules in those adsorbed layers, the threshold capillary pressure obtained from molecular dynamics simulations is greater than expected from conventional techniques such as Mayer-Stowe-Princen (MSP) method. (some of these reviews may be appeared in the previous chapters scatteredly, they are assembled here to serve for the integrity of previous work reviews for this chapter).

In this work, LAMMPS was adopted as the Molecular Dynamics Simulator for the investigation of the confined phase behavior studies. LAMMPS, also known as Large-scale Atomic/Molecular Massively Parallel Simulator, is a classical molecular dynamics open-source code that models an ensemble of particles in a liquid, solid, or gaseous state. It can model atomic, polymeric, biological, metallic, granular, and coarse-grained

systems using a variety of force fields and boundary conditions. The force field mentioned here refers to a set of parameters and equations for use in molecular mechanics simulations. It is designed to model the potential energy of a system of atoms. The force field we adopted in this study is the one in the Transferable Potentials for Phase Equilibria (TraPPE) force field family that is particularly for n-alkanes (Martin and Siepmann, 1998).

All MD simulations were performed in parallel using the TraPPE-United Atom (UA) force field in LAMMPS the stable version. From best practice and preliminary investigations, the cutoff radius was set to be 1.5 nm and the time step of the simulation was 2.0 fmsec. All the simulations were performed using constant NPT or NVT time integration via Nose/Hoover thermostat and barostat. The solid wall configurations (if any) were all fixed in the simulation, built from Virtual NanoLab 2016.4. The initial configurations of the fluid distributions in the simulation boxes were built from Packmol, which is an open source software that is designed for initial configurations of MD simulations by packing optimization.

7.2 Investigate Bulk Phase Transition of Binary Hydrocarbon Mixture Using Molecular Dynamics Simulations

In order to evaluate the performance of MD simulations of hydrocarbon mixture phase behavior quantitatively, a phase separation simulation of bulk C1/n-C4 binary fluid was performed. By using Packmol, a total number of 25,000 methane molecules and 1,000 n-butane molecules were generated in a 30 nm long cubic space, as shown in **Figure 7.1**. The methane molecules are in blue color and n-butane molecules are shown in red. Only

the carbon atoms are shown because in the simulation carbon and hydrogen atoms are defined as a group (pseudo-atom). For example, a methane molecule contains a group of CH_4; a n-butane molecule contains two groups of CH_3 and two CH_2. The force field parameters for C1/n-C4 mixture are obtained from TraPPE-UA and are shown in **Table 7.1**.

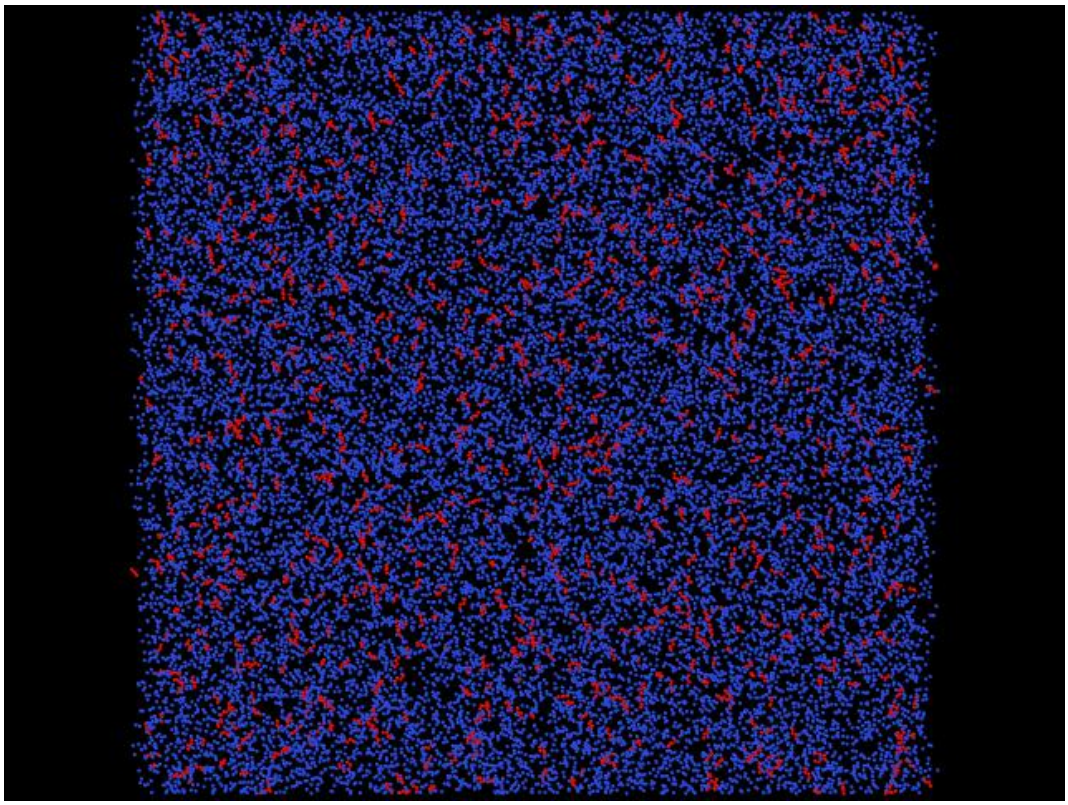

Figure 7.1—The initial configuration of C1/n-C4 binary fluid that contains 25,000 methane molecules and 1,000 n-butane molecules, built from Packmol

Table 7.1: C1/n-C4 mixture force field parameters from TraPPE-UA		
Group	ε/k_B [K]	σ [Å]
CH_4	148.0	3.730
CH_3	98.0	3.750
CH_2	46.0	3.950

NPT ensemble was used in this constant pressure simulation system. The temperature and pressure of the simulation are fixed at 200 K and 3.49 MPa, respectively. **Figure 7.2** shows the snapshots of the simulation where t = 0 ns, 0.16 ns, 0.5 ns, 4 ns, 15 ns and 20 ns. As we can see, beginning the second graph, condensation dropouts start to show and are finally accumulated into one large dropout. The figure shows clearly the phase separation processes within 20 ns of time, starts from vapor phase and ends to vapor-liquid equilibrium. As we can see, the liquid phase is more concentrated with red molecules, which are n-butane molecules, and the vapor phase is more concentrated with blue molecules, which are methane molecules.

Since all the 3D coordinates of each molecules in the simulation box have been recorded by the system, it is possible to compare the results of MD simulation and PR-EOS quantitatively regarding phase properties. In **Table 7.2**, the fluid compositions and fluid densities of each component in each phase obtained from both MD simulation and PR-EOS at 200 K and 3.49 MPa are shown.

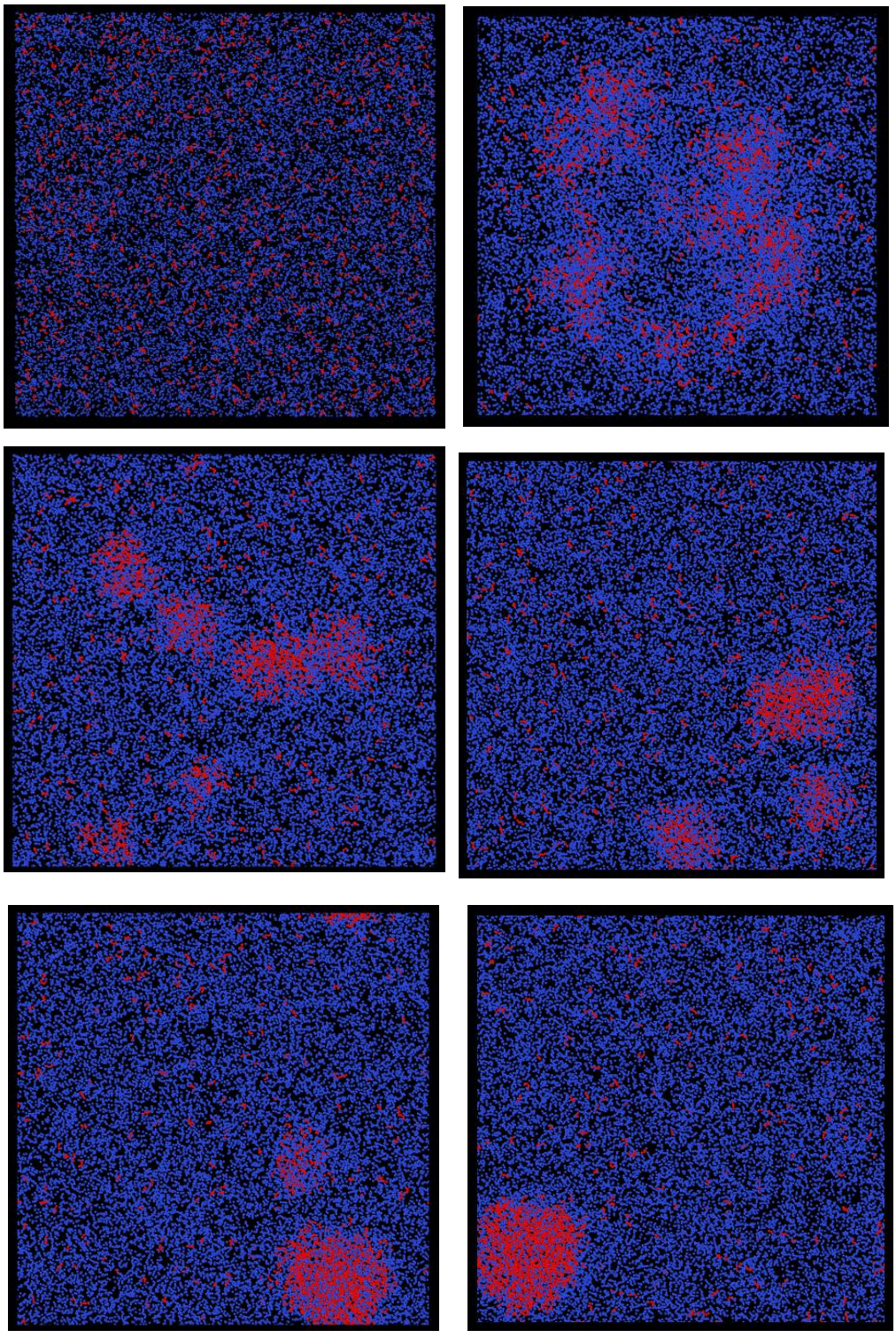

Figure 7.2—The snapshots of the MD simulation where t = 0 ns, 0.16 ns, 0.5 ns, 4 ns, 15 ns and 20 ns

Table 7.2: Phase property results from both MD simulation and PR-EOS at 200 K and 3.49 MPa		
	MD simulation	PR-EOS
C1-nC4 composition in liquid	59.4%-40.6%	59.0%-41.0%
Liquid density (mol/cm^3)	0.0167	0.0170
C1-nC4 composition in vapor	99.7%-0.3%	99.8%-0.2%
Vapor density (mol/cm^3)	0.0035	0.0032

As we can see from Table 7.2, the results from MD simulation and PR-EOS consist with each other for both liquid and vapor fluid property predictions. The results give confidence that the MD simulations are able to capture the phase behavior of hydrocarbon mixtures precisely.

7.3 Investigate Confined Hydrocarbon Mixture Fluid Behavior in Organic Nanopores Using Molecular Dynamics Simulations

In the previous section, MD simulation was performed to predict the liquid-vapor phase separation processes of C1/n-C4 binary mixture in bulk. The results were compared with PR-EOS and gave good match. In this section, MD simulations were extended to investigate the fluid behavior in confined space rather than in bulk. Attractive graphite walls were implemented into the system to represent confinement.

In the first simulation, two graphite sheets spacing 5 nm were generated to represent an organic pore with uniform width of 5 nm. Inside the pore, a total of 2,800 hydrocarbon

molecules including 2,500 methane molecules (color in blue) and 300 n-butane (color in red) molecules were placed randomly inside the pore, as shown in **Figure 7.3**.

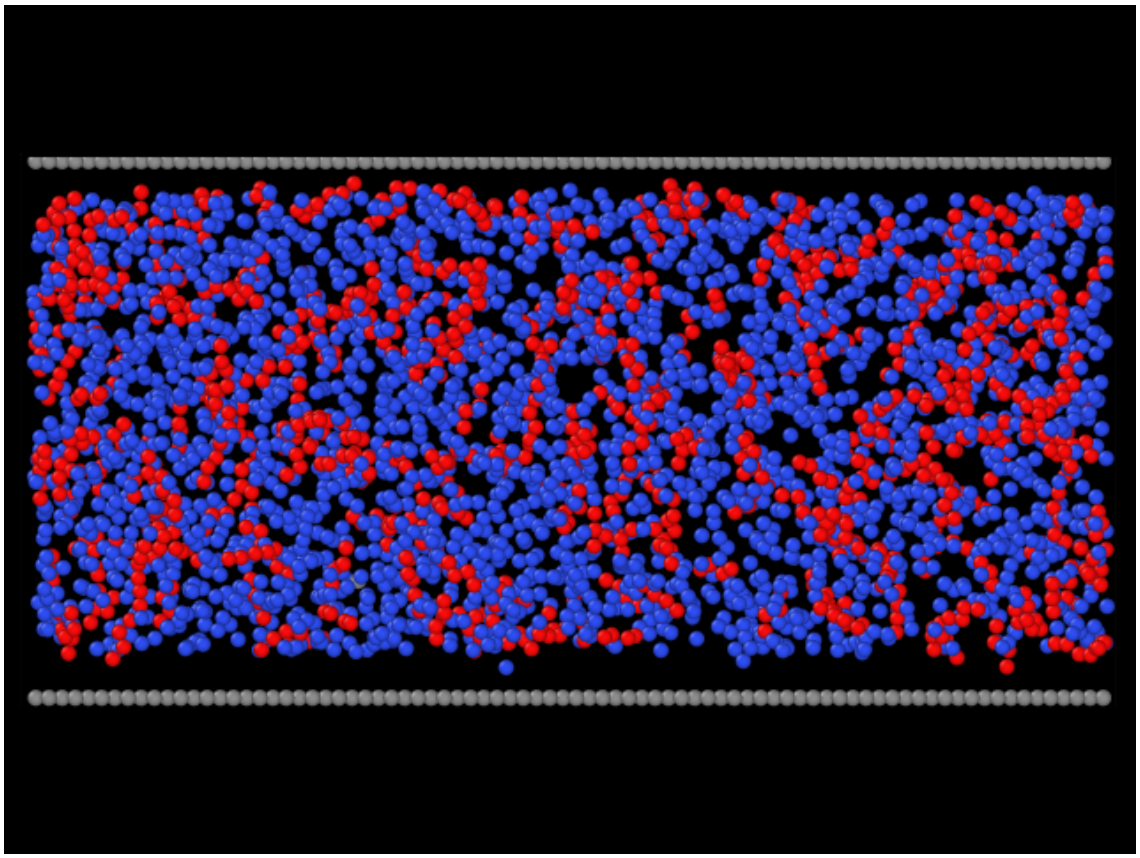

Figure 7.3—The initial configuration of the first simulation. Two graphite sheets represent an organic pore with uniform width of 5 nm. A total 2,500 methane molecules (color in blue) and 300 n-butane (color in red) molecules were placed randomly inside the pore

The pore structure is designed to be fixed in the simulation, therefore, the pore volume does not change. NVT ensemble was adopted to handle situation like this where the system has a constant volume. The temperature was fixed to be 253.15 K. Below in

Figure 7.4 are the snapshots of the simulation where t = 0 ns, 0.02 ns, 0.074 ns and 0.53 ns:

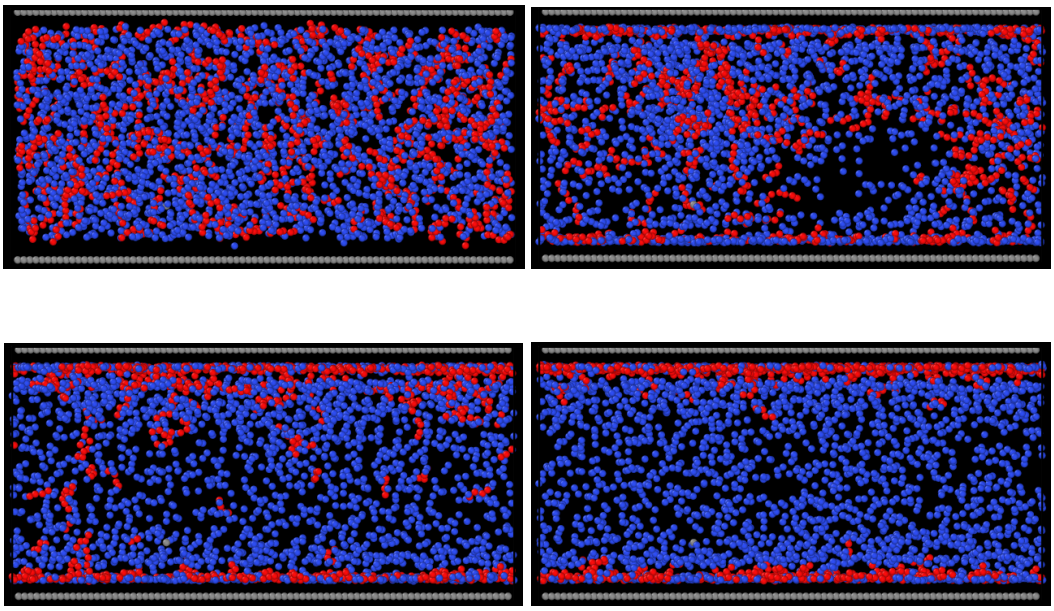

Figure 7.4— The snapshots of the simulation where t = 0 ns, 0.02 ns (upper right), 0.074 ns (bottom left) and 0.53 ns

As we can see from Figure 7.4, when the simulation time gets longer and longer, the n-butane molecules tend to accumulate to the spaces near the pore walls, forming the adsorbed phase. In the last graph of the figure where simulation time equals 0.53 ns, we can barely see any n-butane molecules in the center of the pore. Almost all the n-butane molecules settle in the adsorbed region with only a few of them to the outside but still not too far from the pore wall. For methane molecules, although it is not as obvious as n-butane, it is able to see the density gradient in the direction perpendicular to the pore wall where it is more concentrated in the regions near the pore wall. **Figure 7.5** gives the

averaged layer partial density distributions for the methane and n-butane inside the pore (only half of the pore was shown due to symmetry) and the overall density.

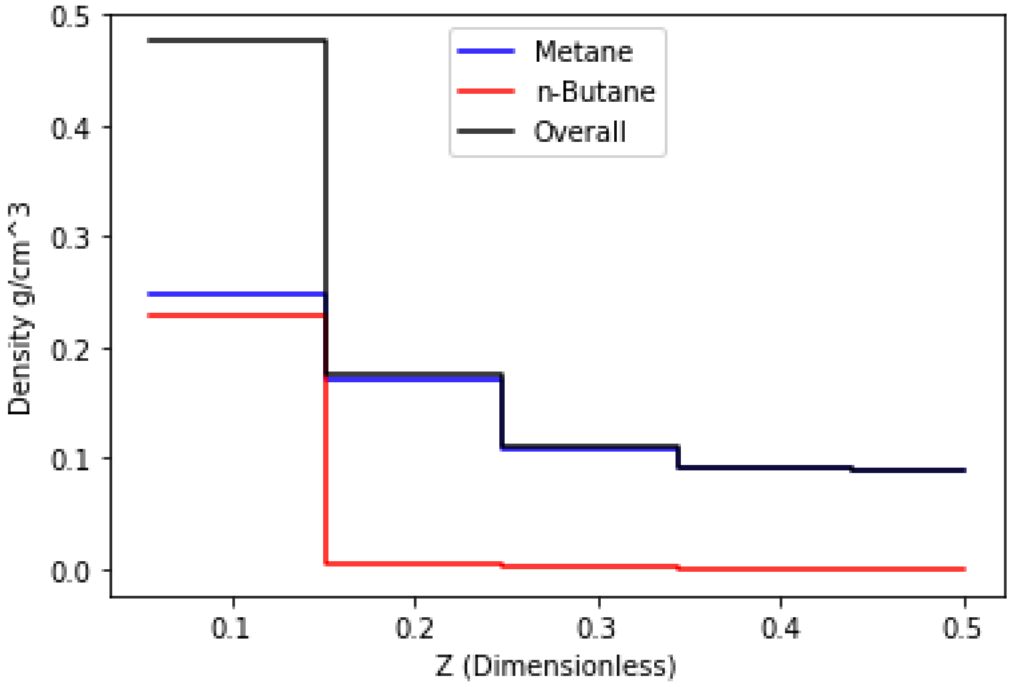

Figure 7.5— The averaged layer density distributions for methane (blue), n-butane(red) and the mixture total (black). The x-axes Z is the dimensionless pore width

The density distributions were calculated from the average values from every 2,000 simulation time steps between t = 1 ns and t = 1.5 ns. The length of the layer equals the diameter of the larger molecule, n-butane in this case. A total of five layers are defined in half of the pore. As we can see from Figure 7.5, the density of methane increases gradually from the center of the pore (0.088 g/cm^3) to the pore wall (0.248 g/cm^3). While the density of n-butane is almost zero for the four layers in the center and then increase dramatically to 0.228 g/cm^3 in the layer closest to the pore wall, known as the adsorbed

layer. The results are consistent with what we see from the last snapshot in Figure 7.4, where the system reaches equilibrium from its initial configuration.

For the second MD simulation, a two-pore system is introduced to investigate the effects of pore size on fluid behaviors. **Figure 7.6** shows the initial configuration of the second MD simulation. Two pores with different sizes built from graphite sheets are directly connected to each other. The larger pore has a width of 4.1 nm and the smaller pore is 2.0 nm in width. The four shorter graphite sheets perpendicular to the wall are placed only to keep fluid molecules inside the pores and have no interactions (LJ energy potential=0). A total of 900 methane molecules (color in blue) and 300 n-butane (color in red) molecules were generated randomly in the center of the pores. The system ran under NVT ensemble with a fixed temperature of 353.15 K. **Figure 7.7** shows the snapshots of the simulation where t = 0 ns, 0.05 ns, 0.15 ns and 1.25 ns.

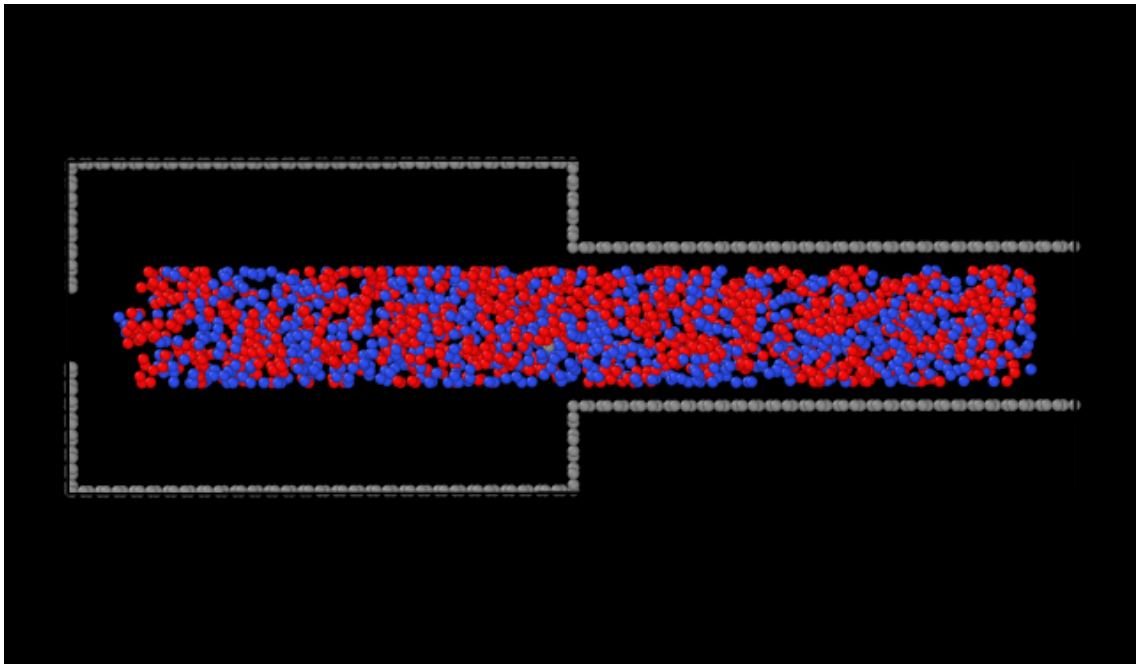

Figure 7.6— The initial configuration of C1/n-C4 mixtures in a two-pore system

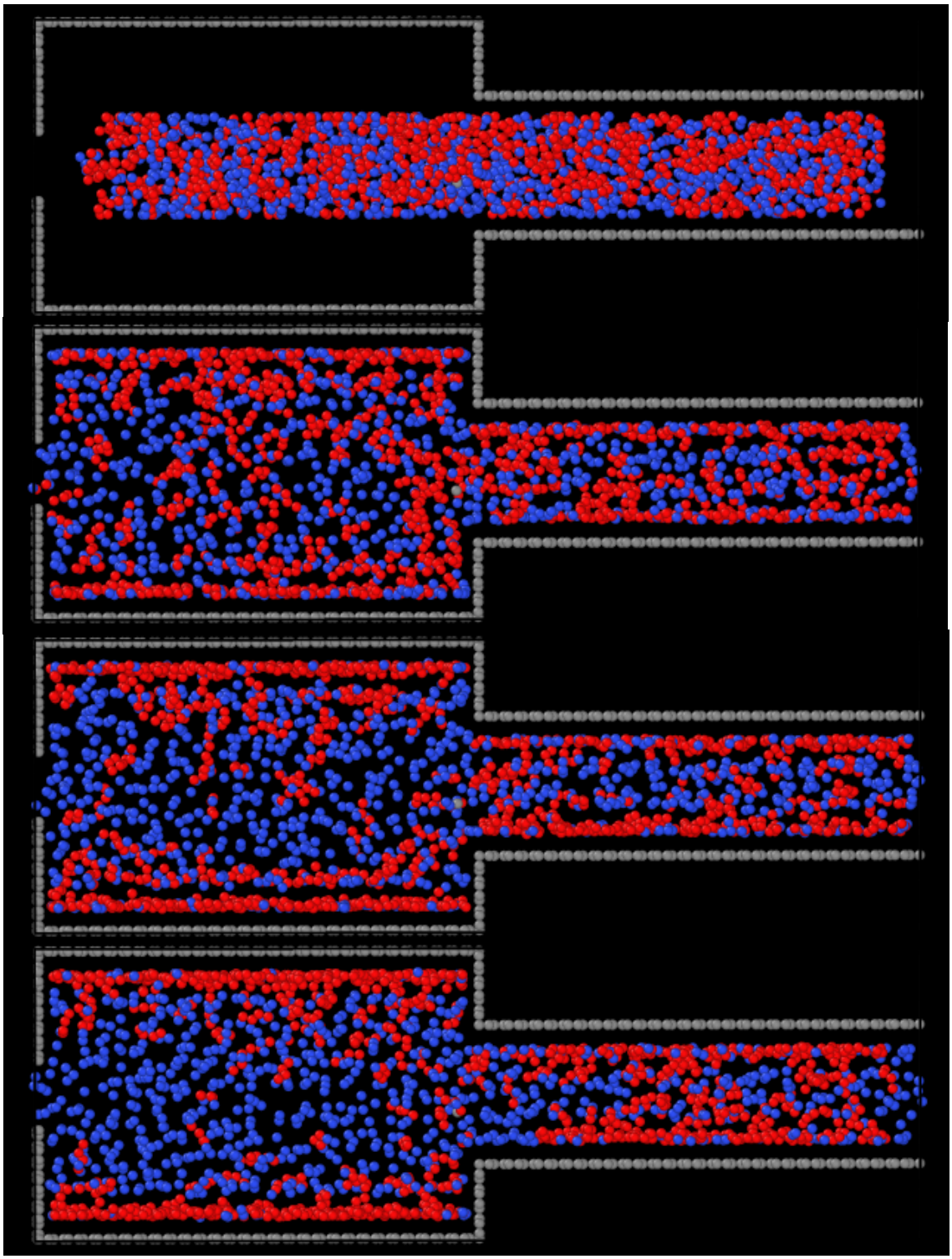

Figure 7.7—Snapshots of the simulation where t = 0 ns, 0.05 ns, 0.15 ns and 1.25 ns

As we can see from the figure, n-butane molecules tend to stay close to the pore walls for both larger and smaller pores. **Table 7.3** shows the average number of methane and n-butane molecules and their compositions in each pore at equilibrium. From the results, it is clear that the composition of n-butane in smaller pore is larger than that in the larger pore. This means that competitively, the smaller pore attracts n-butane more than methane. The molecule number ratio of lager/smaller pore gives a hint of how fluid distributes differently in the two pores. If the fluid distributes uniformly over the entire space, this number should be 2.00 (number of molecules should be proportional the volume of the pore, the volume of the larger pore is 2 times of the smaller pore). In Table 7.3, this number is 2.20 for methane and 1.80 pore n-butane. This means that nearly 10% of the methane molecules in larger pores have been placed by n-butane molecules due to the confinement effects.

Table 7.3: Molecule count of methane and n-butane in each pore at equilibrium

	Methane	n-Butane
Number of molecules in larger pore	619	193
Composition in larger pore	76.2%	23.8%
Number of molecules in smaller pore	281	107
Composition in smaller pore	72.4%	27.6%
Molecule number ratio of lager/smaller pore	2.20	1.80

Chapter 8: Conclusions and Recommendations

8.1 Conclusions

The following conclusions can be drawn from the dissertation:

1. The van der Waals and Peng-Robinson EOS were modified to consider the effect of fluid-wall interactions on phase behavior. Correlations of critical property shift from three different hydrocarbons (C1, nC4 and nC8) were developed based on molecular simulation data from Singh et al. (2009) to calculate and include the effect of fluid-wall interactions into EOS.

2. The SLD-PR model for both single component (C1, nC4 and nC8) and fluid mixtures (C1 and nC4) were described. Such model is capable of predicting the fluid density distributions across the nanoscale pores accurately under much shorter computational time compare to molecular simulations. The model was tested with molecular simulation data.

3. The confinement effects in nanoscale pores can affect fluid critical properties, fluid vapor-liquid ratio and K-value for each component. When the pore size gets smaller, the critical temperatures and pressures of the fluids will decrease and the fluid vapor-liquid ratio will increase. The K-values of the heavy components in the mixture (such as nC4 and C10) will increase with decreasing pore size, while the K-values of the light components (such as C1) remain either constant or decrease slightly when the pore size decreases.

4. The two-phase region of hydrocarbon mixtures (53.01% C1/ 10.55% nC4/ 36.44% C10) shrinked under the influence of the wall from 100 nm to 2 nm. The

upper dew point pressure can decrease up to around 100% from 2500 psi to 1300 psi when the fluids are confined in the 2-nm pore. This can either delay the pressure when condensate dropout occurs by up to 1200 psi or even no occurrence of condensation during production, of a gas-condensate shale reservoir.

5. For a binary mixture contains C1 and nC4, the wall favors heavier component (nC4) compare to the lighter component (C1). The composition of the heavier component (nC4) becomes dominant near the wall regardless of the bulk composition.

6. Pore size can decrease the percentage of space occupied by bulk fluid to the whole pore volume. When the pore size is small enough, the bulk region can disappear and the whole pore is occupied by adsorbed fluid. For heavier component (such as nC4), the pore size at which the bulk region just disappears is larger than that for lighter component (such as C1), under the same conditions.

7. Higher pressure can shift the whole fluid density profile to higher values. However, increase in pressure can have larger impact on the fluid in the bulk compare to that in the adsorbed region. For example, when pressure increased from 3000 psi to 4000 psi at 200 °F in a 10-nm pore, the bulk methane density was increased by 0.035 g/cm^3 while the adsorbed methane density was only increased by 0.020 g/cm^3. On the other hand, increase in temperature can decrease the fluid density for both bulk fluid and adsorbed fluid. The decrease amount of densities for both bulk fluid and adsorbed fluid are similar. When the temperature increased from 150 °F to 200 °F, at 4000 psi in a 10 nm pore, bulk methane density

decreased by 0.018 g/cm^3 and methane adsorbed density decreased by 0.020 g/cm^3.

8. The adsorption of mixture hydrocarbons at high-pressure-high-temperature is multi-layer adsorption. The Langmuir adsorption theory, which assumes single layer adsorption mechanism, may not applicable. For the real case gas-in-place model application, sensitivity analysis on the Eagle Ford fluid showed the storage capacities of adsorbed gas and free gas in organic content are sensitive to temperature, pressure, fluid composition and pore size distributions. However, the total gas-in-place does not change significantly when changing temperature, fluid composition and pore size distributions. The only dominant effect on total gas-in-place is pressure.

9. The effects of adsorption on fluid density and fluid distributions are more obvious at low-pressure ranges. When the pressure gets higher, the confined fluid tends to behavior similar to bulk fluid. For example, for an equal molar C1/C3 mixture at 350 K in 8 and 20 nm pores, the C3 selectivity over C1 first increases with pressure. It then reaches the maximum values of 2.04 and 1.34 for 8 and 20 nm pores, respectively when the pressure is about 8 MPa. After that the C3 selectivity starts to decrease as further increase in pressure. The values of C3 selectivity for 8 and 20 nm pores approach to 1.42 and 1.16 when the pressure is at 50 MPa, respectively.

10. The phase transition of pure fluid in confined space is analyzed using the discrete density profiles. The results showed that the molecular layers of the fluid close to

wall are not sensitive to phase transition (vapor to liquid) when the pore pressure exceeds the bulk saturation pressure. These layers are fulfilled with fluid molecules and achieve maximum density at the pressure much lower than the saturation pressure. For the layers in the center of the pore, sharp density changes are seen near the bulk saturation pressure indicating the occurrence of phase transition. However, the phase transitions of these layers occur at pressures lower than the bulk saturation pressure. The phase transition pressure of these layers can be roughly estimated by the modified Young-Laplace equation.

11. The modified Young-Laplace equation is used to predict capillary condensation. For a retrograde mixture, the effects of capillary condensation can lower the lower dew point pressure and increase the upper dew point pressure. The shift is larger for the lower dew point pressure. For example, for a binary mixture contains 80% C1 and 20% nC5 at 360 K that is confined in a 14-nm pore, the lower dew point pressure shifts from 3.1 to 2.6 MPa by 0.5 MPa, while the shift for the upper dew point pressure is only 0.2 MPa, which is from 15.5 to 15.7 MPa.

12. Molecular dynamics simulations were performed to study the confined fluid phase behavior for hydrocarbon mixtures. The results were consistent with what we predict using PR-EOS and SLD model. Heavier components favor to stay as close to the pore wall as possible, forming the adsorbed phase. For a two-pore system. Heavier components tend to stay in the smaller pore and squeeze the lighter component out from the smaller pore to the larger pore.

8.2 Future Work Recommendations

Although SLD model provides good results and is simple to use, we can extend SLD model to curvature surfaces such as cylinders and spheres. We can then extend the methodology to pore networks and upscale to reservoir scale.

In Chapter 8, we see that molecular simulation is a powerful tool to study the confined phase behavior. Besides adsorption, we can study how and at what situation will capillary condensation will occur inside the nanopores using molecular dynamics. We can also run non-equilibrium molecular dynamics simulations to see how adsorption and capillary condensation can affect fluid flow at different pore size, temperature, pressure and fluid types. The results from molecular simulation studies can be used to tune the modified equation of states and/or adsorption isotherms.

References

1. Abdul-Rehman, H. B., Hasanain, M. A., and Loughlin, K. F. 1990. Quaternary, Ternary, Binary, and Pure Component Sorption on Zeolites. 1. Light Alkanes on Linde S-115 Silicalite at Moderate to High Pressures. *Industrial & Engineering Chemistry Research* **29** (7): 1525-1535.

2. Adachi, Y. and Sugie, H. 1986. A New Mixing Rule— Modified Conventional Mixing Rule. *Fluid Phase Equilibria* **28** (2): 103-118.

3. Alcoutlabi, M. and McKenna, G.B. 2005. Effects of Confinement on Material Behaviour at the Nanometre Size Scale. *Journal of Physics: Condensed Matter* **17** (15): R461.

4. Ambrose, R. 2011. Micro-Structure of Gas Shales and its Effects on Gas Storage and Production Performance. Ph.D. Dissertation, The University of Oklahoma, Norman, OK.

5. Ambrose, R., Hartman, R., Diaz-Campos, M., Akkutlu, I. Y., and Sondergeld, C. 2012. Shale Gas-in-Place Calculations Part I: New Pore-Scale Considerations. *SPE Journal* **17** (1): 219-229.

6. Bae, Y. S., Mulfort, K. L., Frost, H., Ryan, P., Punnathanam, S., Broadbelt, L. J., and Snurr, R. Q. 2008. Separation of CO_2 from CH_4 Using Mixed-Ligand

Metal−Organic Frameworks. *Langmuir* **24** (16): 8592-8598.

7. Barrett, E. P., Joyner, L. G., and Halenda, P. P. 1951. The Determination of Pore Volume and Area Distributions in Porous Substances. I. Computations from Nitrogen Isotherms: *Journal of the American Chemical Society* 73(1): 373-380.

8. Beaton, A.P., Pawlowicz, J.G., Anderson, S.D.A., Berhane, H., and Rokosh, C.D. 2010. Total Organic Carbon and Adsorption Isotherms of the Duvernay and Muskwa Formations in Alberta: Shale Gas Data Release. Energy Resources Conservation Board, ERCB/ AGS, Edmonton, Alberta. p. 33.

9. Chen, J.H., Wong, D.S.H., Tan, C.S., Subramanian, R., Lira, C.T., and Orth, M. 1997. Adsorption and Desorption of Carbon Dioxide onto and From Activated Carbon at High Pressures. *Industrial & engineering chemistry research* **36** (7): 2808-2815.

10. Chen, J.H., Zhang, J., Jin, G., Quinn, T., Frost, E., and Chen, J. 2012. Capillary Condensation and NMR Relaxation Time in Unconventional Shale Hydrocarbon Resources. Presented at SPWLA 53rd Annual Logging Symposium, Long Beach, 18-22 July.

11. Chen, J.H., Mehmani, A., Li, B., Georgi, D., and Jin, G. 2013. Estimation of Total Hydrocarbon in the Presence of Capillary Condensation for Unconventional Shale

Reservoirs. Presented at SPE Middle East Oil and Gas Show and Conference, Manama, Bahrain, 10-13 March. SPE-164468-MS.

12. Coasne, B., Alba-Simionesco, C., Audonnet, F., Dosseh, G., and Gubbins, K. E. 2009. Adsorption and Structure of Benzene on Silica Surfaces and in Nanopores. *Langmuir* **25** (18): 10648-10659.

13. Curtis, M.E., Ambrose, R.J., Sondergeld, C.H., and Rai, C.S. 2010. Structural Characterization of Gas Shales on the Micro- and Nano-Scales. Paper SPE 137693 presented at the Canadian Unconventional Resources and International Petroleum Conferenece, Calgary, Canada, 19-21 October.

14. Curtis, M.E., Ambrose, R.J., Sondergeld, C.H. and Rai, C.S. 2011. Investigation of the Relationship between Organic Porosity and Thermal Maturity in the Marcellus Shale. Paper SPE 144370 presented at the North American Unconventional Gas Conference and Exhibition, The Woodlands, Texas, 14-16 June.

15. Chareonsuppanimit, P., Mohammad, S.A., Robinson Jr, R.L., and Gasem, K.A.M. 2012. High-Pressure Adsorption of Gases on Shales: Measurements and Modeling. *International Journal of Coal Geology* **95**: 34-46.

16. Danesh, A. 1998. PVT and Phase Behavior of Petroleum Reservoir Fluids. Volume 47, Elsevier Science.

17. de Keizer, A., Michalski, T., and Findenegg, G.H. 1991. Fluids in Pores: Experimental and Computer Simulation Studies of Multilayer Adsorption, Pore Condensation and Critical-Point Shifts. *Pure and applied chemistry* **63** (10): 1495-1502.

18. Demontis, P., Stara, G., and Suffritti, G.B. 2003. Behavior of Water in the Hydrophobic Zeolite Silicate at Different Temperatures: A Molecular Dynamics Study. *Journal of Physical Chemistry B* **107** (18): 4426-4436.

19. Deo, M. and Anderson, T. 2012. Liquids from Shales Reservoir Description and Dynamics. Phase 2, Research Progress Report.

20. Derouane, E.G. 2007. On the Physical State of Molecules in Microporous Solids. *Microporous and mesoporous materials* **104** (1): 46-51.

21. Diaz-Campos, M. 2010. Uncertainties in Shale Gas-in-Place Calculations: Molecular Simulation Approach. Master's Thesis, The University of Oklahoma, Norman, OK.

22. Didar, B.R. and Akkutlu, I.Y. 2013. Pore-Size Dependence of Fluid Phase Behavior and Properties in Organic-Rich Shale Reservoirs. Paper SPE 164099 presented at the SPE International Symposium on Oilfield Chemistry, The Woodlands, Texas, 8-10 April.

23. Dreibach, F., Staudt, R., and Keller, J.U. 1999. High Pressure Adsorption Data of Methane, Nitrogen, Carbon Dioxide and Their Binary and Ternary Mixtures on Activated Carbon. *Adsorption* **5** (3): 215–227.

24. Du, Z., Manos, G., Vlugt, T. J., and Smit, B. 1998. Molecular Simulation of Adsorption of Short Linear Alkanes and Their Mixtures in Silicalite. *AIChE journal* **44** (8): 1756-1764.

25. Dubinin, M.M. 1960. The Potential Theory of Adsorption of Gases and Vapors for Adsorbents with Energetically Nonuniform Surfaces. *Chemical Review* **60** (2): 235–241.

26. Dukovski, I., Machta, J., Saravana, C., and Auerbach, S.M. 2003. Cluster Monte Carlo Simulations of Phase Transitions and Critical Phenomenon in Zeolites. *Journal of Chemical Physics* **113** (9): 3697-3703.

27. EIA. 2017. http://www.eia.gov

28. Estévez L.A., Müller E.A., and Olivera-Fuentes C. 1988. Predictive Correlation for Binary Interaction Parameters in Cubic Equations of State. AIChE's 1988 Spring National Meeting, New Orleans, USA.

29. Evans, R., Marconi, U.M.B., and Tarazona, P. 1986. Capillary Condensation and Adsorption in Cylindrical and Slit-like Pores. *Molecular and Chemical Phys*ics **82** (10): 1763-1787.

30. Evans, R., 1990. Fluids adsorbed in narrow pores: phase equilibria and structure. *Journal of Physics: Condensed Matter* **2** (46): 8989.

31. Findenegg, G.H., Gross, S., and Michalski, T. 1994. Pore Condensation in Controlled-Pore Glass. An Experimental Test of the Saam-Cole Theory. *Studies in Surface Science and Catalysis* **87**: 71-80.

32. Frenkel, D. and Smit, B. 2001. Understanding Molecular Simulation: from Algorithms to Applications. Vol. 1, Academic Press.

33. Gasem, K.A.M., Robinson, R.L., Jr., Fitzgerald, J.E., and Pan, Z.; Sudibandriyo, M. Sequestering Carbon Dioxide in Coalbeds; DE-FC26- 98FT40426, prepared for the U.S. Department of Energy, 2003.

34. Giovambattista, N., Rossky, P.J., and Debenedetti, P.G. 2009. Effect of Temperature on the Structure and Phase Behavior of Water Confined by Hydrophobic, Hydrophilic, and Heterogeneous Surfaces. *Journal of Physical Chemistry B* **113** (42): 13723-13734.

35. Gelb, L.D., Gubbins, K.E., Radhakrishnan, R., and Sliwinska-Bartkowiak, M. 1999. Phase Separation in Confined Systems. *Rep. Prog. Phys* **62**: 1573–1659.

36. Groß, S. and Findenegg G.H. 1997. Pore Condensation in Novel Highly Ordered Mesoporous Silica. *Berichte der Bunsengesellschaft für physikalische Chemie* **101** (11): 1726-1730.

37. Hamada, Y., Koga, K., and Tanaka, H. 2007. Phase Equilibria and Interfacial Tension of Fluids Confined in Narrow Pores. *J. Chem Phys* **127** (8): 1-9.

38. Harlick, P.J.E. and Tezel, F. H. 2003. Adsorption of Carbon Dioxide, Methane and Nitrogen: Pure and Binary Mixture Adsorption for ZSM-5 with SiO_2/Al_2O_3 Ratio of 280. *Separation and Purification Technology* **33** (2): 199-210.

39. Hartman, R.C., Ambrose, R. J., Akkutlu, I. Y., and Clarkson, C. R. 2011. Shale Gas-In-Place Calculations Part II-Multicomponent Gas Adsorption Effects. SPE 141416 presented at North American Unconventional Gas Conference and Exhibition, Oklahoma City, Oklahoma, USA, 27-29 March.

40. Heuchel, M., Davies, G.M., Buss, E., and Seaton, N.A. 1999. Adsorption of Carbon Dioxide and Methane and Their Mixtures on an Activated Carbon: Simulation and Experiment. *Langmuir* **15** (25): 8695-8705.

41. IHS. 2014. http://www.fekete.com

42. Jamili, A. 2010. Modeling Effects of Diffusion and Gravity Drainage on Oil Recovery in Naturally Fractured Reservoirs Under Gas Injection. Ph.D. Dissertation, University of Kansas, Lawrence, KS.

43. JD van der Waals. 1873. Over de Continuiteit van den Gas-en Vloeistoftoestand.

44. Jiang, J. and Sandler, S.I. 2006. Capillary Phase Transitions of Linear and Branched Alkanes in Carbon Nanotubes from Molecular Simulation. *Langmuir* **22** (17): 7391-7399.

45. Jin, Z. and Firoozabadi, A. 2016. Thermodynamic Modeling of Phase Behavior in Shale Media. *SPE Journal* **21** (01): 190-207.

46. Koga, K., Gao, G.T., Tanaka, H., and Zeng, X.C. 2001. Formation of Ordered Ice Nanotubes inside Carbon Nanotubes. *Nature* **412** (6849): 802-805.

47. Kotdawala, R.R., Kazantzis, N., and Thompson, R. W. 2005. Analysis of Binary Adsorption of Polar and Nonpolar Molecules in Narrow Slit-Pores by Mean-Field Perturbation Theory. *Journal of Chemical Physics* **123** (24): 244709.

48. Langmuir, I. 1918. The Adsorption of Gases on Plane Surface of Glass, Mica and Platinum: The Research Laboratory of The General Electric Company, p. 1361-1402.

49. Lee, L.L. 1988. Molecular Thermodynamics of Nonideal Fluids. Butterworth-Heinemann.

50. Łencka, M., and Anderko, A. 1991. On the Composition-Dependent Interaction Parameters in Equations of State. *Chemical Engineering Communications* **107** (1), 173-188.

51. Li, B., Mehmani, A., Chen, J., Georgi, D.T., and Jin, G., 2013. 2013. The Condition of Capillary Condensation and Its Effects on Adsorption Isotherms of Unconventional Gas Condensate Reservoirs. Presented at SPE Annual Technical Conference and Exhibition, New Orleans, Louisiana, 30 September-2 October. SPE-166162-MS.

52. Li, B., Mezzatesta, A., Thern, H., Zhang, B., Wu, J., and Zhang, H. 2014. The Condition of Capillary Condensation and Its Effects on Gas-in-Place of Unconventional Gas Condensate Reservoirs. SPE 170837 presented at SPE Annual Technical Conference and Exhibition, Amsterdam, The Netherlands, 27-29 October.

53. Li, M., Gu, A., Lu, X., and Wang, R. 2003. Determination of the Adsorbate Density from Supercritical Gas Adsorption Equilibrium Data. *Carbon* **41** (3): 585–588.

54. Li, Y.K. and Nghiem, L.X. 1982. The Development of a General Phase Envelope Construction Algorithm for Reservoir Fluid Studies. Paper SPE 11198 presented at the SPE Annual Technical Conference and Exhibition, New Orleans, 26–29 September.

55. Loucks, R. G., Reed, R. M., Ruppel, S. C., and Hammes, U. 2012. Spectrum of Pore Types and Networks in Mudrocks and a Descriptive Classification for Matrix-Related Mudrock Pores. *AAPG Bulletin* **96** (6): 1071-1098.

56. Lucia, A. and Brian M.B. 2012. Molecular Geometry Effects and the Gibbs–Helmholtz Constrained Equation of State. *Computers & Chemical Engineering* **37**: 1-14.

57. Luffel, D.L. and Guidry, F.K. 1992. New Core Analysis Methods for Measuring Rock Properties of Devonian Shale. *J. Pet. Tech*. **44** (11): 1184–1190.

58. Ma, Y., Jin, L., Jand amili, A. 2013. Modifying van der Waals Equation of State to Consider Influence of Confinement on Phase Behavior. Paper SPE 166476 presented at the SPE Annual Technical Conference and Exhibition, New Orleans, LA, 31 September-2 October.

59. Ma, Y. and Jamili, A. 2014. Modeling the Effects of Porous Media in Dry Gas and Liquid Rich Shale on Phase Behavior. SPE 169128 presented at Improved Oil Recovery Symposium, Tulsa, Oklahoma, USA, 12-16 April.

60. Ma, Y. and Jamili, A. 2016. Modeling the Density Profiles and Adsorption of Pure and Mixture Hydrocarbons in Shales. *J. Unconventional Oil Gas Resource* **14**: 128-138.

61. Maddox, M. W., Sowers, S. L., and Gubbins, K. E. 1996. Molecular Simulation of Binary Mixture Adsorption in Buckytubes and MCM-41. *Adsorption* **2** (1): 23-32.

62. Mao, Z., and Susan B.S. 2001. Separation of Organic Molecular Mixtures in Carbon Nanotubes and Bundles: Molecular Dynamics Simulations. *Journal of Physical Chemistry B* **105** (29): 6916-6924.

63. Martin, M.G. and Siepmann, J.I. 1998. Transferable Potentials for Phase Equilibria. 1. United-Atom Description of n-alkanes. *Journal of Physical Chemistry B* 102 (14): 2569-2577.

64. Masel, R. I., 1996. Principles of Adsorption and Reaction on Solid Surfaces. Vol. 3, John Wiley & Sons.

65. Mavor, M.J. and Nelson, C.R. 1997. Coalbed Reservoir Gas-In-Place Analysis. Report GRI-97/0263, Gas Research Institute, Chicago, Illinois.

66. McCain, W.D., John P.S., and Lenn, C.P. 2011. Petroleum Reservoir Fluid Property Correlations. PennWell Books.

67. Menon, P.G. 1968. Adsorption at High Pressures. *Chemical Reviews* **68** (3): 277–294.

68. Mohammad, S.A., Chen, J.S., Robinson Jr, R.L., and Gasem, K.A. 2009. Generalized Simplified Local-Density/Peng−Robinson Model for Adsorption of Pure and Mixed Gases on Coals. *Energy & Fuels* **23** (12): 6259-6271.

69. Monson, P.A. 2005. Recent Progress in Molecular Modeling of Adsorption and Hysteresis in Mesoporous Materials. *Adsorption* **11**: 29–35.

70. Mosher, K., He, J., Liu, Y., Rupp, E., and Wilcox, J. 2013. Molecular Simulation of Methane Adsorption in Micro-and Mesoporous Carbons with Applications to Coal and Gas Shale Systems. *International Journal of Coal Geol*ogy **109**: 36-44.

71. Neimark A.V., Ravikovitch P.I., and Vishnyakov A. 2003. Bridging Scales from Molecular Simulations to Classical Thermodynamics: Density Functional Theory of Capillary Condensation in Nanopores. *Journal of Physics: Condensed Matter* **15** (3): 347-365.

72. Nghiem, L.X. 1983. A New Approach to Quasi-Newton Method with Application to Compositional Modeling. Paper SPE 12242 presented at the 1983 SPE Symposium on Reservoir Simulation, San Francisco, 16–18 November.

73. Nicholson, D. and Parsonage, N.G. 1982. Computer Simulation and the Statistical Mechanics of Adsorption. Academic press, New York.

74. Nishiumi H., Arai T., and Takeuchi K. 1988. Generalization of the Binary Interaction Parameter of the Peng-Robinson Equation of State by Component Family. *Fluid Phase Equilibria* **42**: 43-62.

75. Nuttall, B.C., Eble, C.F., Drahovzal, J.A., Bustin, M. 2005. Analysis of Devonian Black Shales in Kentucky for Potential Carbon Dioxide Sequestration and Enhanced Natural Gas Production. Kentucky Geological Survey, University of Kentucky, Lexington, Kentucky.

76. Panagiotopoulos, A.Z., and Reid, R.C. 1986. New Mixing Rule for Cubic Equations of State for Highly Polar, Asymmetric Systems. *ACS Symposium Series* **300** (28): 571-582.

77. Peng, D.Y. and Robinson, D.B. 1976. A New Two-Constant Equation of State. *Industrial & Engineering Chemistry Fundamentals* **15** (1): 59-64.

78. Petersen C.S. 1989. A Systematic and Consistent Approach to Determine Binary Interaction Coefficients for the Peng-Robinson Equation of State. *SPE Reservoir Engineering* **4** (04): 488-494.

79. Poling B.E., Prausnitz J.M., and O'Connell J.P. 2001. The Properties of Gases and Liquids. New York: McGraw-Hill.

80. Rangarajan, B., Lira, C.T., and Subramanian, R. 1995. Simplified Local Density Model for Adsorption Over Large Pressure Ranges. *AIChE Journal* **41** (4): 838-845.

81. Redlich, O. and Kwong J.N.S. 1949. On the Thermodynamics of Solutions. V. an Equation of State. Fugacities of Gaseous Solutions. *Chemical Reviews* **44** (1): 233-244.

82. Rine, J. M., Dorsey, W., Floyd, M., and Lasswell, P. 2011. Comparative SEM Study of Pore Types and Porosity Distribution in High to Low Porosity Samples from Selected Gas-Shale Formations.

83. Sage, B.H. and Lacey, W.N. 1950. Thermodynamic Properties of the Lighter Paraffin Hydrocarbons and Nitrogen. Monograph on API Research Project 37, API, New York.

84. Sapmanee, K. 2011. Effects of Pore Proximity on Behavior and Production Prediction of Gas/Condensate. MS Thesis, The University of Oklahoma, Norman, Oklahoma.

85. Schmidt G. and Wenzel H. 1980. A Modified van der Waals Type Equation of State. *Chemical Engineering Science* **35** (7): 1503-1512.

86. Schoen, M. and Diestler, D.J. 1998. Analytical Treatment of a Simple Fluid Adsorbed in a Slit-Pore. *Journal of Chemical Physics* **109** (13): 5596-5606.

87. Schulze, W. 1993. A Simple Generalization of the Binary Temperature-Dependent Interaction Parameters in the Soave-Redlich-Kwong and Peng-Robinson Equations of State for Helium-Mixtures. *Fluid phase equilibria* **87** (2): 199-211.

88. Sedghi, M., Piri, M., and Goual, L. 2016. Atomistic Molecular Dynamics Simulations of Crude Oil/Brine Displacement in Calcite Mesopores. *Langmuir* **32** (14): 3375-3384.

89. Severson, B.L. and Snurr, R.Q. 2007. Monte Carlo Simulation of n-alkane Adsorption Isotherms in Carbon Slit Pores. *Journal of Chemical Physics* **126** (13): 134708-1-134708-7.

90. Shapiro, A.A. and Stenby, E.H. 1996. Effects of Capillary Forces and Adsorption on Reserves Distribution, SPE 36922 presented at the 1996 SPE European Petroleum Conference held in Milan, Itaty, 22 – 24 October.

91. Sigmund, P.M., Dranckhuk, P.M., Morrow, N.R., and Purvis, R.A. 1973. Retrograde Condensation in Porous Media. *SPE Journal* **12** (02): 93-104.

92. Singh, S.K., Sinha, A., Deo, G., and Singh, J.K. 2009. Vapor-Liquid Phase Coexistence, Critical Properties, and Surface Tension of Confined Alkanes. *Journal of Physical Chemistry C* **113** (17): 7170–7180.

93. Soave, G. 1972. Equilibrium Constants from a Modified Redlich-Kwong Equation of State. *Chemical Engineering Sci*ence **27** (6): 1197-1203.

94. Stryjek, R. and Vera, J.H. 1986. PRSV: An Improved Peng-Robinson Equation of State for Pure Compounds and Mixtures. *Canadian Journal of Chemical Engineering* **64** (2): 323-333.

95. Tan, S.P. and Piri, M. 2015. Equation-of-State Modeling of Confined-Fluid Phase Equilibria in Nanopores. *Fluid Phase Equilibria* **393**: 48-63.

96. Tarazona, P., Marini Bettolo Marconi, U., and Evans, R. 1987. Phase Equilibria of Fluid Interfaces and Confined Fluids Non-Local Versus Local Density Functional. *Molecular Physics* **60** (3): 573-595.

97. Thommes, M. and Findenegg G.H. 1994. Pore Condensation and Critical-Point Shift of a Fluid in Controlled-Pore Glass. *Langmuir* **10** (11): 4270-4277.

98. Thommes, M., Kaneko, K., Neimark, A.V., Olivier, J.P., Rodriguez-Reinoso, F., Rouquerol, J., and Sing, K.S. 2015. Physisorption Of Gases, with Special Reference to the Evaluation of Surface Area and Pore Size Distribution. *Pure and Applied Chemistr*y **87** (9-10): 1051-1069.

99. Thomson, W. 1872. 4. On the Equilibrium of Vapor at a Curved Surface of Liquid. *Philosophical Magazine Series 4* **42** (282): 448-452.

100. Tindy, R. and Raynal, M. 1966. Are Test-Cell Saturation Pressure Accurate Enough? *Oil and Gas Journal* **64** (49): 126-139.

101. Travalloni, L., Castier, M., Tavares, F.W., and Sandler, S. 2010a. Thermodynamic modeling of confined fluids using an extension of the generalized van der Waals theory. *Chemical Engineering Science* **65** (10): 3088-3099.

102. Travalloni, L., Castier, M., Tavares, F. W., and Sandler, S. 2010b. Critical Behavior of Pure Fluids from an Extension of the van der Waals Equation of State. *Journal of Supercritical Fluids* **55** (2): 455-461.

103. Trebin, F.A. and Zadora, G.I. 1968. Experimental study of the effect of porous media on phase change in gas condensate systems. *Neft' i Gaz* 81: 37.

104. Trens, P., Tanchoux, N., Galarneau, A., Brunel, D., Fubini, B., Garrone, E., and Renzo, F.D. 2005. A Macrothermodynamic Approach to the Limit of Reversible Capillary Condensation. *Langmuir* **21** (18): 8560-8564.

105. Voronov, V.P., Belyakov, M.Y., Gorodetskii, E.E., Kulikov, V.D., Muratov, A.R., and Nagaev, V.B. 2003. Phase Behavior of Methane-Pentane Mixture in Bulk and in Porous Media. *Transport in porous media* **52** (2): 123-140.

106. Walls, J. D., Diaz, E., Derzhi, N. Grader, A., Dvorkin, J., Arredondo, S., Carpio, G., and Sinclair, S. W., 2011. Eagle Ford Shale Reservoir Properties from Digital Rock Physics, presented at HGS Applied Geoscience Mudrocks Conference, Feb 7 – 8, Woodlands, TX.

107. Walton, J.P.R.B. and Quirke, N.P.R.B. 1989. Capillary Condensation: A Molecular Simulation Study. *Molecular Simulation* **2** (4-6): 361-391.

108. Weniger, P., Kalkreuth, W., Busch, A., and Krooss, B. M. 2010. High-Pressure Methane and Carbon Dioxide Sorption on Coal and Shale Samples from The Paraná Basin, Brazil. *International Journal of Coal Geology* **84** (3): 190-205.

109. Whitson C.H. and Brulé M.R. 2000. Phase behavior. Richardson, Tex.: Henry L. Doherty Memorial Fund of AIME, Society of Petroleum Engineers.

110. Wu, J. 2006. Density Function Theory for Chemical Engineering: from Capillarity to Soft Materials. *AIChE. Journal* **52** (3): 1169-1193.

111. Wu, Q., Zhou, L., Wu, J., and Zhou, Y. 2005. Adsorption Equilibrium of The Mixture CH_4^+ N_2^+ H_2 on Activated Carbon. *Journal of Chemical & Engineering Data* **50** (2): 635-642.

112. Yang, Q. and Zhong, C. 2006. Molecular Simulation of Carbon Dioxide/Methane/Hydrogen Mixture Adsorption in Metal-Organic Frameworks. *The Journal of Physical Chemistry B* **110** (36): 17776-17783.

113. Yun, J. H., Düren, T., Keil, F. J., and Seaton, N. A. 2002. Adsorption of Methane, Ethane, and Their Binary Mixtures on MCM-41: Experimental Evaluation of Methods for The Prediction of Adsorption Equilibrium. *Langmuir* **18** (7): 2693-2701.

114. Yuan, W., Pan, Z., Li, X., Yang, Y., Zhao, C., Connell, L. D., and He, J. 2014. Experimental Study and Modeling of Methane Adsorption and Diffusion in Shale. *Fuel* **117** (A): 509-519.

115. Zarragoicoechea, G.J. and Kuz, V.A. 2002. van der Waals Equation of State for a Fluid in a Nanopore. *Physical Review E* **65** (2): 1-4.

116. Zarragoicoechea, G.J. and Kuz, V.A. 2004. Critical Shift of a Confined Fluid in a Nanopore. *Fluid Phase Equilibria* **220** (1): 7-9.

117. Zeigermann, P., Dvoyashkin, M., Valiullin, R., and Kärger, J. 2009. Assessing the Pore Critical Point of The Confined Fluid by Diffusion Measurement. *Diffusion-fundamentals* **11** (41): 1-2.

118. Zhang, T., Ellis, G. S., Ruppel, S. C., Milliken, K., and Yang, R. 2012. Effect of Organic-Matter Type and Thermal Maturity on Methane Adsorption in Shale-Gas Systems. *Organic Geochemistry* **47**: 120-131.

119. Zhu, H.Y., Ni, L.A., and Lu, G.Q. 1999. A Pore-Size-Dependent Equation of State for Multilayer Adsorption in Cylindrical Mesopores. *Langmuir* **15** (10): 3632-3641.

120. Zudkevitch, D. and Joffe, J. 1970. Correlation and Prediction of Vapor-Liquid Equilibria with The Redlich-Kwong Equation of State. *AIChE Journal* **16** (1): 112-119.

Appendix A: Expressions of position dependent equation of state parameter

According to Chen et al. (1997), the equation of state parameter, a, which is known as the internal pressure correction term, is dependent on the position of the fluid molecule with respect to the pore walls, as well as the pore diameter and fluid molecular diameter.

When $L/\sigma_{ff} \geq 3$, a(z) has the following expressions:

$$\frac{a_{ff}(z)}{a} = \frac{3}{8}\left[\frac{z}{\sigma_{ff}} + \frac{5}{6} - \frac{1}{3}\left(\frac{L-z}{\sigma_{ff}} - \frac{1}{2}\right)^{-3}\right] \quad \text{for} \quad 0.5 \leq \frac{z}{\sigma_{ff}} \leq 1.5 \quad \text{.....(A.1)}$$

$$\frac{a_{ff}(z)}{a} = \frac{3}{8}\left[\frac{8}{3} - \frac{1}{3}\left(\frac{z}{\sigma_{ff}} - \frac{1}{2}\right)^{-3} - \frac{1}{3}\left(\frac{L-z}{\sigma_{ff}} - \frac{1}{2}\right)^{-3}\right] \quad \text{for} \quad 1.5 \leq \frac{z}{\sigma_{ff}} \leq \frac{L}{\sigma_{ff}} - 1.5 \quad \text{.....(A.2)}$$

$$\frac{a_{ff}(z)}{a} = \frac{3}{8}\left[\frac{L-z}{\sigma_{ff}} + \frac{5}{6} - \frac{1}{3}\left(\frac{z}{\sigma_{ff}} - \frac{1}{2}\right)^{-3}\right] \quad \text{for} \quad \frac{L}{\sigma_{ff}} - 1.5 \leq \frac{z}{\sigma_{ff}} \leq \frac{L}{\sigma_{ff}} - 0.5 \quad \text{.....(A.3)}$$

When $2 \leq L/\sigma_{ff} \leq 3$, a(z) is given by:

$$\frac{a_{ff}(z)}{a} = \frac{3}{8}\left[\frac{z}{\sigma_{ff}} + \frac{5}{6} - \frac{1}{3}\left(\frac{L-z}{\sigma_{ff}} - \frac{1}{2}\right)^{-3}\right] \quad \text{for} \quad 0.5 \leq \frac{z}{\sigma_{ff}} \leq 1.5 \quad \text{.....(A.4)}$$

$$\frac{a_{ff}(z)}{a} = \frac{3}{8}\left[\frac{L}{\sigma_{ff}} - 1\right] \quad \text{for} \quad 1.5 \leq \frac{z}{\sigma_{ff}} \leq \frac{L}{\sigma_{ff}} - 1.5 \quad \text{.....(A.5)}$$

$$\frac{a_{ff}(z)}{a} = \frac{3}{8}\left[\frac{L-z}{\sigma_{ff}} + \frac{5}{6} - \frac{1}{3}\left(\frac{z}{\sigma_{ff}} - \frac{1}{2}\right)^{-3}\right] \quad \text{for} \quad \frac{L}{\sigma_{ff}} - 1.5 \leq \frac{z}{\sigma_{ff}} \leq \frac{L}{\sigma_{ff}} - 0.5 \quad \text{.....(A.6)}$$

If $1.5 \leq L/\sigma_{ff} \leq 2$, then a(z) is:

$$\frac{a_{ff}(z)}{a} = \frac{3}{8}\left(\frac{L}{\sigma_{ff} - 1}\right) \quad \text{.....(A.7)}$$

Appendix B: Volumetric Method for Shale Gas Content Calculations

By definition, the amount of free gas in inorganic matrix is the total volume of the gas at surface condition per unit mass of rock:

$$G_{f,inorg} = \frac{V_{f,inorg,surf}}{M_b} \quad \text{(B.1)}$$

Where $V_{f,inorg,surf}$ is the volume of the free gas at surface condition, M_b is the mass of the rock. By applying the mass conservation at surface condition and reservoir condition, we can have:

$$G_{f,inorg} = \frac{V_{f,inorg,res}\rho_{f,res}}{\rho_{f,surf}\rho_b V_b} \quad \text{(B.2)}$$

Where $V_{f,inorg,res}$ is the volume of the free gas at reservoir condition, $\rho_{f,res}$ and $\rho_{f,surf}$ are the free gas density at reservoir and surface conditions, respectively. The total mass of the rock in Equation B.2 is expressed as the product of rock bulk density ρ_b and rock bulk volume V_b. Then, the volume of the free gas at reservoir condition, $V_{f,inorg,res}$, can be expressed in terms of porosity, bulk volume and water saturation.

$$G_{f,inorg} = \frac{V_{tot}[\phi_t(1-S_w)-\phi_k]\rho_{f,res}}{\frac{P_{surf}\overline{M}_f}{Z_f RT_{surf}}\rho_b V_b} \quad \text{(B.3)}$$

Where ϕ_t and ϕ_k are the total porosity and kerogen porosity, respectively. S_w is water saturation. In Equation B.3, the free gas density at surface condition in expressed in terms is apparent free gas molar mass $\overline{M}_f$, compressibility at surface condition Z_f, surface

temperature and pressure and gas constant, based on gas law. If the surface condition is 298.15 K and 0.1 MPa, Equation (A.3) becomes:

$$G_{f,inorg} = 8.7355 \times 10^5 \frac{[\phi_t (1 - S_w) - \phi_k]\rho_{f,res} Z_f}{\sum_i^{n_c} (x_i MW_i)\rho_b} \quad \text{..... (B.4)}$$

In Equation B.4, the apparent free gas molar mass $\bar{M}_f$ is expressed as the summation of the product of composition and molecular weight for each component. The coefficient 8.7355e5 has the unit of scf*g/(ton*mol). The unit of both the gas density and rock density is ton/m^3.

Similarly, the free gas in organic content $G_{f,org}$ at surface condition.

$$G_{f,org} = 8.7355 \times 10^5 \frac{(V_b \phi_k - V_{ads})\rho_{f,res} Z_f}{\sum_i^{n_c} (x_i MW_i)\rho_b V_b} \quad \text{..... (B.5)}$$

Different than Equation B.4, the void volume of occupied by free gas in kerogen at reservoir condition is calculated by subtracting the total kerogen void volume by the volume taken by adsorbed gas.

Therefore, the adsorbed gas in organic content G_{ads} is:

$$G_{ads} = 8.7355 \times 10^5 \frac{V_{ads}\rho_{ads,res} Z_{ads}}{\sum_i^{n_c} (y_i MW_i)\rho_b V_b} \quad \text{..... (B.5)}$$

Note that in Equation B.6 all the gas properties are the properties for the adsorbed gas, which is expected to be different compare to that of the free gas. y_i is the average fluid composition for the adsorbed gas.